Designing the Hole Transport Layer for the Development of Perovskite and Quantum Dot Solar Cells

by

Ashish Sharma
10CC15A26017

A thesis submitted to the
Academy of Scientific & Innovative Research
for the award of the degree of
DOCTOR OF PHILOSOPHY
in

SCIENCE

Under the supervision of
Dr. Arup Kumar Rath

National Chemical Laboratory, Pune

Academy of Scientific and Innovative Research
AcSIR Headquarters, CSIR-HRDC campus
Sector 19, Kamla Nehru Nagar,
Ghaziabad, U.P. – 201 002, India

May - 2021

Certificate

This is to certify that the work incorporated in this Ph.D. thesis entitled, "*Designing the Hole Transport Layer for the Development of Perovskite and Quantum Dot Solar Cells*", submitted by *Ashish Sharma* to the Academy of Scientific and Innovative Research (AcSIR), in partial fulfillment of the requirements for the award of the Degree of *Doctor of Philosophy in Science*, embodies original research work carried-out by the student. We, further certify that this work has not been submitted to any other University or Institution in part or full for the award of any degree or diploma. Research material(s) obtained from other source(s) and used in this research work has/have been duly acknowledged in the thesis. Image(s), illustration(s), figure(s), table(s) etc., used in the thesis from other source(s), have also been duly cited and acknowledged.

(Signature of Student)

Ashish Sharma
Date: 11.05.2021

(Signature of Supervisor)

Dr Arup Kumar Rath
Date: 11.05.2021

STATEMENTS OF ACADEMIC INTEGRITY

I Ashish Sharma, a Ph.D. student of the Academy of Scientific and Innovative Research (AcSIR) with Registration No. 10CC15A26017 hereby undertake that, the thesis entitled "Designing the Hole Transport Layer for the Development of Perovskite and Quantum Dot Solar Cells" has been prepared by me and that the document reports original work carried out by me and is free of any plagiarism in compliance with the UGC Regulations on "*Promotion of Academic Integrity and Prevention of Plagiarism in Higher Educational Institutions (2018)*" and the CSIR Guidelines for "*Ethics in Research and in Governance (2020)*".

Signature of the Student
Date: 11.05.2021
Place: Pune

It is hereby certified that the work done by the student, under my/our supervision, is plagiarism-free in accordance with the UGC Regulations on "*Promotion of Academic Integrity and Prevention of Plagiarism in Higher Educational Institutions (2018)*" and the CSIR Guidelines for "*Ethics in Research and in Governance (2020)*".

Signature of the Supervisor
Name: Dr Arup Kumar Rath
Date: 11.05.2021
Place: Pune

This dissertation is dedicated to my family, who always had faith in me and taught me to persevere with a smile.

Acknowledgment

Throughout the long odyssey of my research scholar life, I have come across people who either accompanied me in this journey or helped and supported me in various forms. To those kindred souls, I am pleased to have an opportunity to express my gratitude here.

First and foremost, it is my greatest privilege to express my utmost gratitude to my research supervisor, ***Dr Arup Kumar Rath*** *for the excellent guidance, perpetual encouragement, steadfast attitude, and constructive criticism during my time as a doctoral student. I had been extremely fortunate to have an advisor who has been both, a guide throughout this winding journey and a teacher who taught me not only the subject but also discipline, work ethics, and ways to achieve my goals. I sincerely acknowledge the freedom rendered by him in the laboratory for independent thinking, planning, and execution of the research as well as maintaining an excellent work culture through his inputs. I believe the best way of thanking him would be through my future contribution to the scientific community.*

I owe to thank my Doctoral Advisory Committee members, ***Dr. T.G. Ajithkumar****,* ***Dr. Sayan Bagchi,*** *and* ***Dr. K Krishnamoorthy*** *for their continued support, guidance, and suggestions which helped my research work immensely.*

I am grateful to ***Prof. Dr. Ashwini K. Nangia*** *(Director, NCL), both* ***Dr. B. L. V. Prasad****, Head, Division of Physical & Materials Chemistry, and* ***Dr P. A. Joy*** *(former head of Division) for giving me this opportunity and providing all necessary infrastructure and facilities.*

My sincere thanks to ***Dr. J. Nithyandan****,* ***Dr Sakya Sen, Dr. Janardan Kundu****,* ***Mrs. Kohle****,* ***Mr. Iyer****,* ***Mr. Purushothaman,*** *Library staff, Student academic office staff, and all other scientists of NCL for their motivation, constant encouragement, and support.*

Furthermore, I want to express my thanks to ***Dr. K. Selvaraj****,* ***Mr. R. S. Gholap*** *and his team for help in HR-TEM, FE-SEM measurements,* ***Mr. Srinivas Deo*** *for his help in XPS measurements, and* ***Dr. Satyajit Sahu (IIT JODHPUR)*** *and his doctoral student* ***Jayanta Bera*** *for their AFM measurements,*

It is my pleasure to thank all my past and present labmates ***Dr Srikanth, Prasenjit, Debranjan, Rangarajan, Anupam, Apoorva, Haris, Saptam, Chandan, Neha,*** *and* ***Asif****,* *for devoting their precious time and valuable suggestions, which indeed helped me during this research work. I would also like to thank all the summer trainees, and project trainees of our labs who assisted me during their time in NCL.*

No words are enough to acknowledge my prized friends in and out of NCL who have helped me at various stages of my work in NCL. I wish to thank, ***Dr Samik, Dr Pranab, Dr Sachin**, **Dr Swamy, Dr Sandeep, Dr Milan, Dr Arun, Dr Sudhakar, Dr Subodh, Mahendra, Urmila, Ruchi, Monika, Shubhra, Sanjukta, Gargi, Rohit.*** *Also,* ***Sujit*** *and* ***Chotu*** *for the homely food without which survival would have been a tad difficult. I have immensely enjoyed these interactions and hopefully learned a few things. I will cherish these memories forever.*

I am thankful to my professor from University of Hyderabad, ***Dr. Periasamy*** *for his valuable chemistry lectures in my Master's degree and for igniting my interest in material chemistry. I am also thankful to* ***Dr. Balamurugan*** *for providing me my first exposure to research and my schoolteacher* ***Mrs. Preeti Ma'm*** *whose strict demeanor and commitment in Science classes still instill me with fear and awe.*

Without the funding I received, this Ph.D. would not have been possible, and I would like to express my sincere appreciation to ***CSIR-JRF-New Delhi*** *for awarding JRF and SRF.*

*My family has always been a source of inspiration and great moral support for me throughout my education and all other aspects of life. I am blessed to have such an understanding family and thoroughly indebted to my parents (**Sub Maj Hari Chand** and **Smt Yashoda**). I would be remiss if I fail to mention my brother* ***MAJ Neeraj*** *and my sister* ***Gitika*** *for being my bedrock always. I also thank my* ***MAJ Akash*** *and* ***MAJ Rujula*** *for their continued support and encouragement. And I hope one day my nephew* ***Akshaj*** *will read (and understand) this thesis.*

I wish to thank the great scientific community whose achievements are a constant source of inspiration for me.

Above all, I thank the Almighty for his enormous blessings.

Ashish Sharma

Table of Contents

Abbreviations

Ag	Silver
Al	Aluminium
AFM	Atomic Force Microscopy
AM	Air Mass
Au	Gold
BHJ	Bulk Heterojunction
B.P.	Boiling Point
CB	Conduction Band
CdS	Cadmium Sulfide
CdSe	Cadmium Selenide
CO_2	Carbon Dioxide
CQD	Colloidal Quantum Dot
CIGS	Copper Indium Gallium Selenide
C-V	Capacitance –Voltage
CZTS	Copper Zinc Tin Sulfide
DSSCs	Dye-Sensitized Solar Cells
E	Energy
EDT	1,2-Ethaneidthiol
E_F	Fermi Level
E_g	Band Gap
EQE	External Quantum Efficiency
ETL	Electron Transport Layer
FF	Fill Factor
FTO	Fluorine-Doped Tin Oxide
FWHM	Full Width at Half Maximum
GaAs	Gallium Arsenide
HOMO	Highest Occupied Molecular Orbital
FWHM	Half Width at Half Maximum
HTL	Hole Transport Layer
Hz	Hertz
I-V	Current –Voltage

ITO	Indium-Doped Tin Oxide
J_{SC}	Short Circuit Current Density
J-V	Current Density-Voltage
LED	Light-Emitting Diode
LUMO	Lowest Unoccupied Molecular Orbital
MEG	Multiple Exciton Generation
mg	Milligram
min	Minute
mL	Millilitre
MHz	Megahertz
mm	Millimetre
mmol	Millimole
M.P.	Melting Point
MPA	Mercaptopropionic Acid
MPE	3-methyl mercaptopropionate
MoO_3	Molybdenum Trioxide
NIR	Near-Infrared
NREL	National Renewable Energy Laboratory
OA/OLA	Oleic Acid
ODE	1-Octadecene
PbS	Lead Sulfide
PbSe	Lead Selenide
PCBM	Phenyl-C61-Butyric Acid Methyl Ester
PCE	Power Conversion Efficiency
PEDOT:PSS	Poly(3,4-ethylene dioxythiophene) poly(styrene sulfonate)
PL	Photoluminescence
QDs	Quantum Dots
R_s	Series Resistance
R_{sh}	Shunt Resistance
SEM	Scanning Electron Microscope
TCO	Transparent Conductive Oxide
TEM	Transmission Electron Microscopy
TiO_2	Titanium Dioxide
VB	Valence Band

V_{bi}	Built-in Potential
V_{OC}	Open Circuit Voltage
XPS	X-ray Photoelectron Spectrometry
XRD	X-ray Diffraction
ZnO	Zinc Oxide

List of Symbols

Φ	Work Function
h	Plank Constant
°C	Degree Centigrade
υ	Frequency
%	Percentage

List of Figures

List of Tables

Chapter I

Introduction

1.1 Photovoltaics – a necessity

The technological advances through the turn of the 20th century have been putting an ever-increasing load on the supply of energy through conventional sources like coal and petroleum. The limited reserves of these fossil fuels and being non-renewable has shifted the onus onto the renewable sources of energy such as solar, wind, and hydro to meet the demand as the population explodes and technology becomes more accessible. As of now, 80% of the world energy requirement is met by the non-renewable energy sources (fossil fuels, natural gas, and nuclear energy), and even glancing over its exhaustibility, these have a slew of problems ranging from CO_2 emissions in coal to proper storage of spent nuclear fuel. Figure 1.1(a) shows the ratio of all energy resources as of 2018.[1] From a report released by the U.S. Department of Energy's Energy Information Administration (EIA), global energy consumption is slated to increase by 28% between 2015 and 2040, where fossil fuels are estimated to provide 77% of the increase. The report also forecasts a 2.8% annual increase in renewable energy, predicting that power generation by these resources will surpass generation by coal on a worldwide basis by 2040.[2] Even though energy consumption is still predominantly fossil fuel-based, renewables are the most rapidly growing energy source for electricity generation. In the Statistical Review of World Energy report published by BP (British Petroleum Company) in 2019, it was reported that the largest increment to power generation was provided by renewable sources, increasing from 9.3% to 10.4%, surpassing nuclear power generation for the first time.[3] For the first time since these data were tabulated, coal's share of generation reported their lowest - 36.4%. The tariff for the solar panel has come down to 1.99 ₹/kWh and a mix of these panels and solar thermal power can provide electricity at a cheaper rate compared to thermal power plants running on coal.

These improvements in renewables and changing landscape of energy consumption coupled with the need to decrease the greenhouse emissions makes it imperative to have low cost photovoltaic (PV) technologies to harness the abundant solar energy and store it (India's solar energy insolation is about 600 TW, global horizontal irradiation shown in Figure 1.1(b)).[4] As the prevalent Silicon solar cells still struggle with costly manufacturing, in this thesis, we focus on developing the emerging perovskite and quantum dot based solar cells. We elucidate the critical role of the hole transport layer on the performance, reproducibility and stability of the solution processed perovskite and quantum dot based solar cells and developed novel hole transport layers to address these challenges.

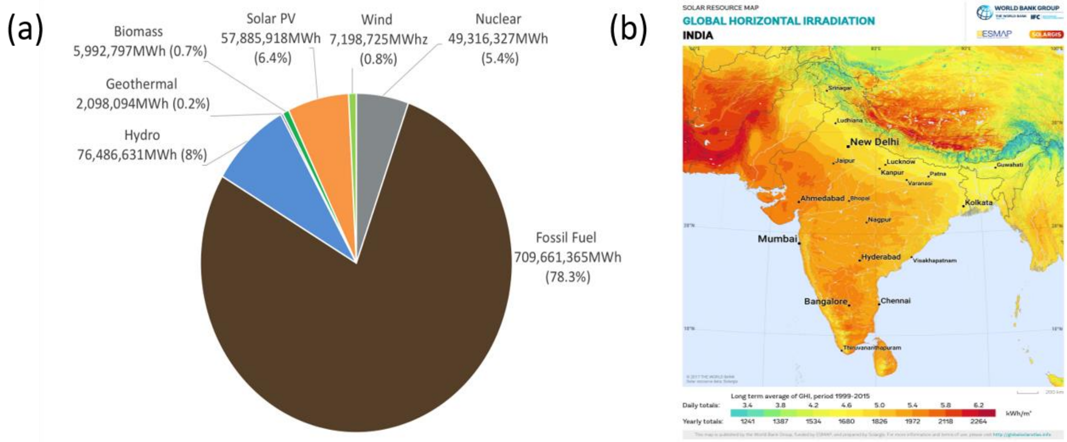

Figure 1.1: (a) Contribution from various energy sources to the total global energy consumption as per ISEP Energy Chart-2018. The relative contributions from different renewable energy sources are marked. (b) Global Horizontal Irradiation in India.

1.2 Development of solar cells

The first step in the solar cell journey was the discovery of the photovoltaic effect by French scientist Edmond Becquerel in 1839 when he noticed electric current generation in an electrolytic cell consisting of two metal electrodes suspended inside a conducting solution when exposed to sunlight.[5] In 1876, Adams and Day discovered that selenium produces electricity when exposed to sunlight and showed that solids could convert light to electricity without heat or mechanical energy generation[6]. This was later utilized by Charles Fritts (1883) to construct a solar cell with selenium on top of a thin layer of gold but achieved a very low efficiency of ~1% owing to Selenium being a bad semiconductor[7]. In 1887, Heinrich Hertz discovered the photoelectric effect (later explained by Albert Einstein) when he noticed that a charged object lost its charge readily when illuminated by ultraviolet light.[8] All these discoveries culminated into the start of Generation-I of solar cells, as Bell Labs announced on April 25, 1954, the first practical silicon solar cell with an efficiency of 6%, the first major step in harnessing the Sun. [9]

The ensuing decade saw the employment of solar cells majorly in the extraterrestrial power supply. In 1958, Hoffman Electronics introduced a solar cell with 9 % efficiency while T. Madelkorn from US Signals Corporation made the first radiation-proof n on p silicon solar cell which is more suited for space purposes and used in Vanguard I. In 1960, Hoffman Electronics boosted the solar cell efficiency to 14 %. Mono-crystalline silicon has been the choice of sensitizer. Westinghouse utilized float zone silicon of thickness 375 µm as the base material and TiO_2 and SiO_2 (Figure 1.2(a)) as front and back contacts to achieve an efficiency of 18.3%.[10] The best performance with the low resistivity float zone silicon was 20.9% PCE with 38.3 mA/cm^2 short circuit current (J_{SC}) obtained by University of South Wales researchers. A further boost was provided by Swanson et al. from Stanford with PCE reaching 22.3% with a modified solar cell structure (Figure 1.2(b)) in AM1.5 conditions in 1984.[11] In 33 years since then the maximum efficiency for Silicon with a heterojunction back-contact crystalline silicon solar cell stands at 26.7%.[12] The thickness of the active layer was 165 µm in this case.

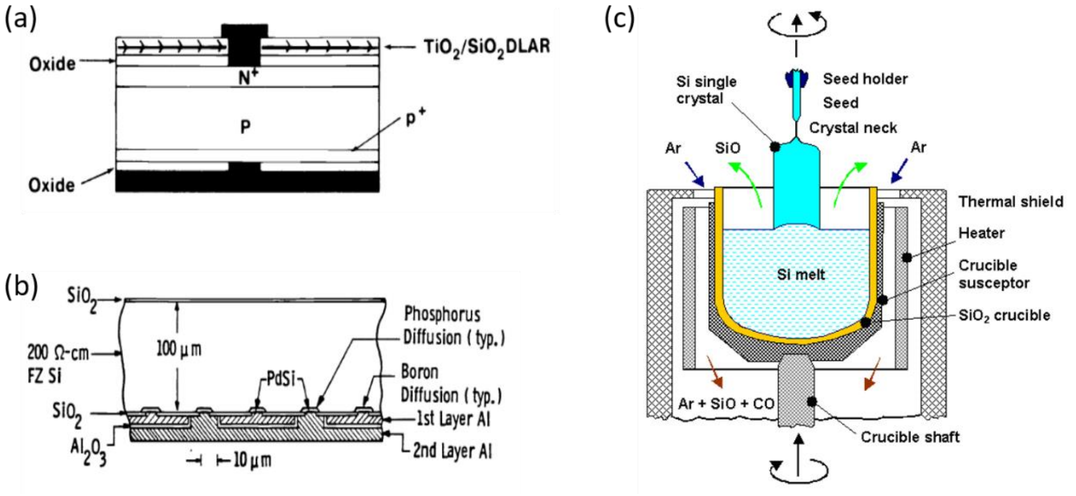

Figure 1.2: (a) Schematic diagram of Westinghouse FZ silicon cell design (b) Point contact cell design consisting of alternating small diffused n- and p-type regions developed by Swanson. (c) Schematic drawing of a crystal growth apparatus employing the Czochralski method.

Though the efficiencies for the Silicon solar cells have very close to its theoretical conversion efficiency (29.1%) given by the Shockley-Quessier limit, there is overall an economical loss sustained in this sector. This stems from Silicon being an indirect semiconductor and as such requires a greater thickness to be able to absorb enough light to be beneficial in photovoltaics. This dictates the thick wafer requirement of monocrystalline Silicon and there is a high cost associated with the preferred method of processing (Czochralski method, 1.2(c)) to achieve the incredibly low impurity concentration of the 10^{-10} %. On top of that, almost half of the wafer material is lost in form of saw dust when shaping wafers. Additionally, Light with higher wavelengths (λ>1200 nm), is not utilized by the solar cell as it fails to generate electron-hole pair here. If we move away from the high-cost manufacturing of monocrystalline-Si towards the polycrystalline-Si, which are incidentally thicker, we generate a lot of grain boundaries which leads to recombination losses both at the top and bottom of the layer thus reducing the total efficiency of the solar cell.[13] Going down to amorphous Si leads to further decrease in efficiency due to band tail formation, low mobility, and lifetime values, and absolute decrease in quantum efficiency. With these drawbacks in mind, direct bandgap materials were investigated to be used as active layer in solar cells.

The second generation of solar cells brought about the thin film fabrication technology for energy production as it shifted to direct bandgap materials consisting of Cadmium telluride (CdTe), Gallium Arsenide (GaAs), Copper Indium Gallium Selenide (CIGS), and even amorphous Si. CIGS and CdTe solar cells have achieved high PCE of 22.9% and 22.1% respectively which are comparable to c-Si solar cells.[14] A schematic of the CIGS solar cell is shown in Figure 1.3(a). Though CIGS is bandgap tunable (1.0 to 2.4 eV by changing the ratio of In:Ga and Se), the underlying issue for expansion of CIGS is the rarity of Indium as well as the complex stoichiometry which makes it challenging to optimize the solar cells. CdTe suffers from a similar set of issues, one being the rarity of Tellurium and the other being the toxicity associated with Cd, thus affecting the large-scale production of these solar cells. For years though, GaAs has been known as the wonder material as it has the near-optimum bandgap of 1.42 eV and has so far achieved the highest efficiency for a single p-n junction solar cell – 28.8%.[15] Being a direct bandgap material, GaAs is used as thin-film but its synthesis utilizes a deposition step onto GaAs wafer and then separating it. This leads to an increase in production cost, similar to that seen in c-Si, and as such, this technology is reserved for high-cost high-efficiency applications (typically related to space). GaAs has been utilized in space applications since 1965 and recently with triple-junction solar cell based upon GaAs with germanium and indium gallium phosphide layers to achieve a record efficiency of over 32%. This triple-junction solar cell was used for power generation in satellite MidSTAR-1 (as shown in Figure 1.3(b)) launched in 2007. Amorphous Si utilizes a randomly organized structure and has a high band gap of 1.7 eV, when compared to c-Si 1.1 eV, allowing stronger absorption in the visible range and subsequently decreasing the thickness. It was predicted to take over the market due to its low cost but it suffered from low efficiencies and decreased photostability.

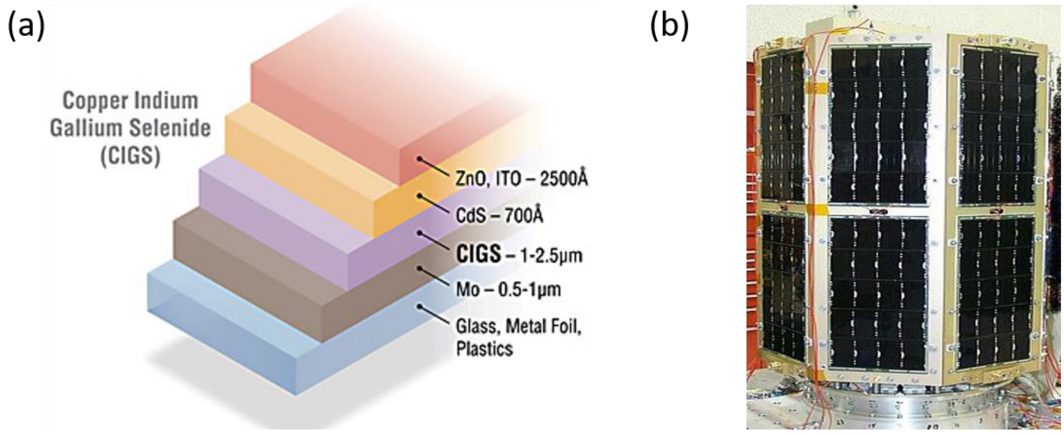

Figure 1.3: (a) Schematic diagram of a typical CIGS solar cell. Many approaches replace the toxic CdS layer used here with a non-toxic buffer layer. (b) Triple-junction GaAs cells covering MidSTAR-1 satellite.

The introduction of Dye Sensitized Solar Cell (DSSC) by Michael Grätzel and Brian O'Regan kickstarted the third generation of solar cells of which all the modern technologies are a part of. The third generation of solar cells is different from the first two as it focuses on optimization following the 'golden triangle'- (i) high conversion efficiency, (ii) long term photostability while (iii) keeping the cost of devices low. The first report for DSSC was published by Grätzel in 1991 with an efficiency of 7.9%.[16] Though the efficiency was lower compared to other competing strategies, it was considered more viable with its advantages like low-cost materials, easy manufacturability, transparency (employment in window panes augmented by color choices, Figure 1.4(a)), and mechanical flexibility. The potential was high with theoretical efficiency estimated to be around 32% but the achieved PCE has been only just above 14% in the 30 years of research since.[17] The major disadvantages with the DSSC has been the sintering of Titanium oxide (TiO_2) limiting the substrate choice, the best dyes (Ruthenium based) and counter electrode (Platinum) being expensive, and use of the liquid electrolyte redox couple (I^-/I_3^-) which can cause leakage, cause corrosion of counter electrode and even lead to detachment of the adsorbed dye from the TiO_2. Figure 1.4(b) shows the classic constituents of the DSSCs. Though by using solid-state electrolyte solves most of the stability issues, other factors still limit the large-scale production of DSSCs.

Copper Zinc Tin Sulphide (CZTS) is a quaternary semiconducting material developed in line with CIGS having similar favourable optical and electronic properties as CIGS and CdTe but having abundant and non-toxic constituents. Sulfur can be replaced with Selenium to form CZTSe or an alloy of sulfur and selenium to form CZTSSe solar cells. The power output for CZTS and CZTSSe has remained relatively low when compared to other previous technologies with 11.0% and 12.6% efficiency respectively.[18] This stems from the complexity of the design as the formation of phase pure material is difficult and the stability is low thermodynamically (Sn compounds are volatile). The other problem arises from the similar ionic radii of Cu and Zn which leads to antisite defect where Cu cations can occupy Zn sites and vice versa. These defects then lead to an increase in band tail states. Research has been, thus, mostly stagnant for this quaternary material.

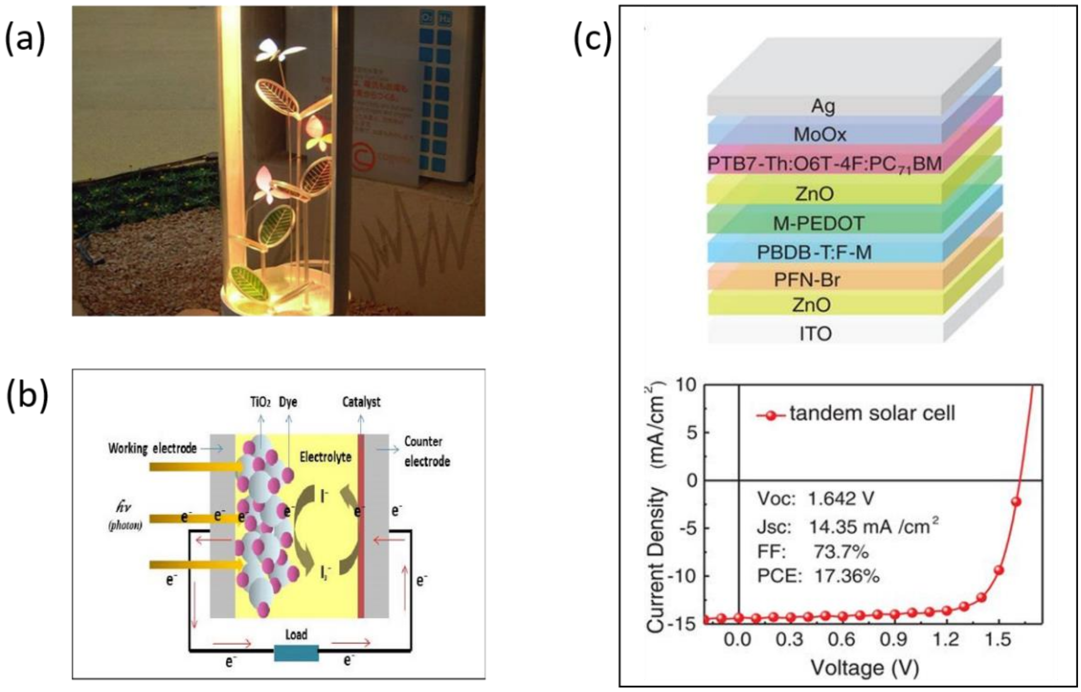

Figure 1.4: (a) A 'plant' with leaves made of DSSC. It shows the benefit of these cells under diffused light. Similar applications lie in windows, sheds, etc. (b) Working principle of a DSSC.[16] (c) Device structure of the tandem solar cell used. Bottom J-V curve shows the improvement in photovoltaic parameters.[21]

Organic solar cells (OSC) have been around for quite a while and the first single layer report was published in 1958 with magnesium phthalocyanine (MgPc) as the absorbing layer sandwiched as Al/MgPc/Ag. The efficiency was a meagre 0.01% with 200 mV photovoltage.[19] Since then the device structure has developed further to bilayer structures with one electron donor and one electron acceptor material, three layered structures (two acceptors and one donor), bulk heterojunction (BHJ) structure, and the more promising of all tandem solar cell. OSC has many advantages, the foremost of them being cheap and printable on flexible surfaces. Additionally, by molecular engineering whereby ligand sizes are changed, different bandgaps could be achieved and the extinction coefficient of these organic molecules is high.[20] For decades the commercial viability of OSCs have been under the scanner due to their low external quantum efficiency (EQE), insufficient absorption, low hole mobility, lower exciton diffusion length, low dielectric constant, high exciton binding energy, and stability woes. The lifetime for these solar cells is abysmally low. Still, there have been ongoing investigations in this field and more recently by delving into a tandem structure with two organic photovoltaics (OPV), Meng et al. managed to achieve a high PCE of 17.3% with 1.64 V photovoltage and a high 0.74 fill factor (Figure 1.4(c)).[21]

In this thesis, work has been done on two new promising technologies that aim to fulfil the necessities of the golden triangle - the colloidal quantum dots (CQD) solar cells and the perovskite solar cells (PSC). Both of these are a product of the 21st century with perovskite being fairly new with the first report dating back to 2009 by Kojima et al. with an introductory efficiency of 3.9%.[22] Through tremendous research effort in this area, within a decade a very high PCE of >24% for a single p-n junction solar cell was achieved.[23] These direct bandgap materials possess properties like ambipolar transport, low exciton binding, high carrier mobility (in the range ~ 10–30 $cm^2V^{-1}s^{-1}$), and long recombination lifetime.[24] The CQD solar cells have also increased in performance starting from 1% in 1998 to 13.8% as of now.[25] Lead sulfide (PbS) quantum dots have been at the forefront among other CQDs such as PbSe, CuSe, CdSe, etc owing to its easily tunable bandgap, longer hot carrier lifetimes, multiple exciton generation (MEG) ability, and solution processability with solar cell fabrication cheaper than most technologies out there. Figure 1.5 shows the evolution of PCE for PbS QD solar cells and PSC as compiled by National Renewable Energy Laboratory, USA. As this thesis includes work done in the improvement of both organic-inorganic perovskite ($CH_3NH_3PbI_3$) as well as PbS CQD solar cells, there is a short introduction for both in the next two segments.

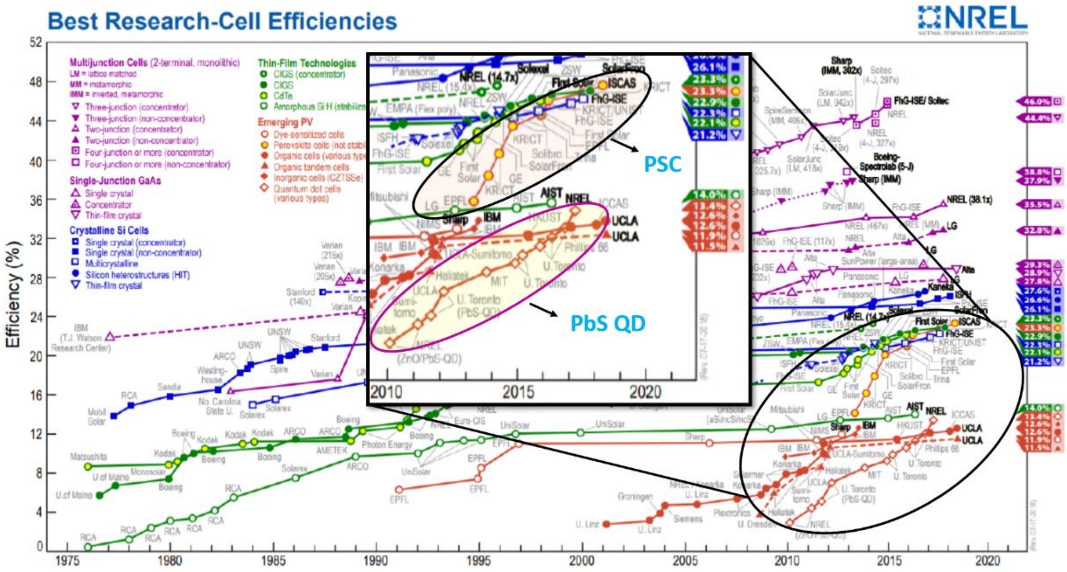

Figure 1.5: NREL chart indicating the progress of single p-n junction perovskite and PbS QD solar cells.

1.3 Perovskite Solar Cells

1.3.1 Fundamentals of perovskite solar cells

Perovskite is the name of materials with structure ABX_3 where A is a cation, B is a metal atom and X is the anion (shown in Figure 1.6(a)). This structure was first found in calcium titanate, $CaTiO_3$ and later, Caesium lead halides, with the chemical formula $CsPbX_3$ (X = Cl, Br or I), were determined by Danish scientist Christian Møller with crystallography. He was also the first to observe their semiconducting nature. In 1978, Dieter Weber replaced caesium with methylammonium cations ($CH_3NH_3^+$) to generate the first three-dimensional organic–inorganic hybrid perovskites but could not contemplate it having photovoltaic properties.[26] The first report for that came after 3 decades in 2006 when Miyasaka and co-workers used $CH_3NH_3PbBr_3$ and achieving an efficiency of 2.2% in a DSSC architecture and further replaced the bromine with iodine to get 3.8% efficiency.[22] Since then perovskite materials have found their use in multitude of applications ranging from lasers, photodetectors, photocatalysts, X-ray imaging, LEDs, X-ray imaging, etc.

Many strategies have been developed for preparing the three-dimensional perovskite material. Majority of the earlier work focused on the organic-inorganic lead trihalide or mixed-halide (I^-, Br^- and/or Cl^-) perovskites. In these ABX_3 crystals, the ionic radii of the ions determine if the perovskite can form, and the precise crystal unit cell size and type. A parameter, which indicates if an efficient and stable perovskite crystal structure will be formed, is Goldschmidt's tolerance factor, which is given by $(t = (r_A + r_X)/\sqrt{2}\,(r_B + r_X))$. The value for t needs to fall between 0.9 and 1.013 to form simple cubic perovskite.[27] Table 1.1 lists the ionic radii of various ions used in ABX_3 which helps in screening the potential candidates. The electronic contributions to the band structure originate from the metal and halide orbitals and metal needs to match the valency of halides. This in turn creates a window within which the size of metal ion should lie to have an effective perovskite material thereby limiting the choice of the metals. To date, Lead has been the only successful metal in terms of coordination and size. Efforts were made to replace the toxic Pb with Sn but tin struggles with its slightly smaller size and its tendency to quickly undergo oxidation to give Sn^{4+} thus being detrimental to the perovskite crystal structure.

Table 1.1. Ionic radii of various ions in ABX_3 perovskite structure

A cations	radius (pm)	B cations	radius (pm)	X cations	radius (pm)
Ammonium $[NH_4^+]$	146	Pb^{2+}	119	Cl^-	181
Methylammonium $[CH_3NH_3]^+$	217	Sn^{2+}	69	Br^-	196
Azetidinium $[(CH_2)_3NH_2]^+$	250	Mg^{2+} (additive)	72	I^-	220
Formamidinium $[NH_2(CH)NH_2]^+$	253	Ca^{2+} (additive)	100	SCN^-	213
Dimethylammonium $[(CH_3)_2NH_2]^+$	272	Sr^{2+} (additive)	118		
Ethylammonium $[(C_2H_5)NH_3]^+$	274	Ag^+ (additive)	115		
Guanidinium $[C(NH_2)_3]^+$	278	Bi^{3+} (additive)	103		
Tetramethylammonium $[(CH_3)_4N]^+$	292				
Cs^+	167				
Rb^+	152				
K^+	137				

1.3.2 Progress in PSCs

The 3.8% PSC made by Kojima suffered from rapid degradation due to involvement of I^-/I_3^- liquid electrolyte and though efficiency was boosted to 6.5% in 2011, the instability remained.[28] This was eventually resolved in 2012 when a solid-state material, spiro-OMeTAD (2,2′7,7′-tetrakis-(N,N-di-p-methoxyphenyl-amine)-9,9′-spirobifluorene) was used as hole conductor.[29] The most studied 3D perovskites are $MAPbI_3$ ($MA = CH_3NH_3^+$) and $FAPbI_3$ ($FA = CH(NH_2)_2^+$). From an efficiency of 9.7% for pure $MAPbI_3$ in 2012, we have come to a high PCE of 25.6% using a pseudo halide formate ion (HCOO-) to suppress halide vacancies in FAPbI3 perovskite in 2021.[29,30] In 2013, first high efficiency of 14.1% was achieved for a two-step deposition method.[31] A high PCE of 24.2% was certified in 2019, with V_{OC} of 1.2 V, J_{SC} of 24.16 mA/cm^2, and fill factor 0.84. Various lead precursors had been utilized along with PbI_2 such as $PbCl_2$, $PbAc_2.3H_2O$, $PbBr_2$, $Pb(SCN)_2$, etc.[32] These changes improved film morphology and resulted in higher efficiencies.

Efforts were made to replace Pb with Sn to make perovskite more environment friendly. The $MASnI_3$ perovskite has a bandgap of ~1.2–1.3 eV, allowing broader light harvesting. $ASnI_3$ perovskites (with A= Cs, MA, and FA) have suitable optical bandgaps in the range of 1.2–1.4 eV. $CsPbBr_3$ has a band gap as high as 2.3V. Although $CsSnI_3$ (with $SnCl_2$) showed low efficiency of around 3.4%, $MASnI_3$ reached an efficiency of 6.4%. These pure tin perovskites are still inferior to pure lead ones and efforts were also made to incorporate both Pb and Sn-based perovskites in the crystal structure as $(FASnI_3)_{0.6}(MAPbI_3)_{0.4}$, producing a record efficiency of 17.5% (Figure 1.6).[33]

Depending upon the presence of different cations, perovskite could also be converted from a 3-D structure to the 2-D perovskite with the cations acting as an interlayer between two sheets of inorganic BX_4 octahedra, which help combating moisture-related degradation. Initially, Smith et al. made 2D layered $(PEA)_2(MA)_2[Pb_3I_{10}]$ showing V_{OC} of 1.18 V and PCE 4.73%.[34] Docampo et al. prepared layered 2D perovskite by utilizing a bottom MAPI layer and an LPK top layer, which serves as a selective charge extraction layer and moisture barrier, obtaining a high PCE of 16.8%.[35] Mohite group in 2016 obtained 12.52% efficiency for pure 2D perovskite by making near-single-crystalline films using a hot-cast method which have out-of-plane alignment.[36] These moisture stable perovskites are required for the longer shelf life of solar panels.

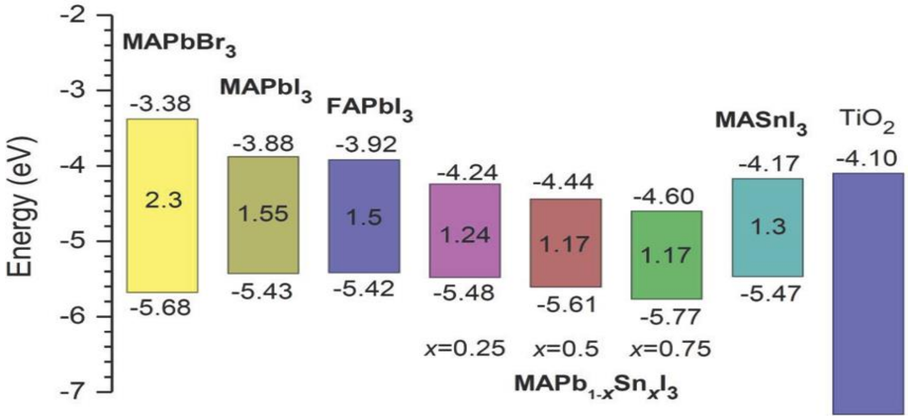

Figure 1.6: Bandgap comparison for different three-dimensional organic inorganic perovskite with ABX_3 structure.[33]

1.3.3 Transport layers Engineering

In the standard n-i-p solar cell, sunlight hits the sensitizer (perovskite) through the transparent conducting surface, FTO. Excitons are generated inside the material and the weakly bound hole and electrons move towards HTL and ETL respectively. Electrons hop to the ETL and subsequently to the FTO from perovskite through the lower conduction band and holes jump to HTM and gold through the valence band. They recombine outside to generate electricity.

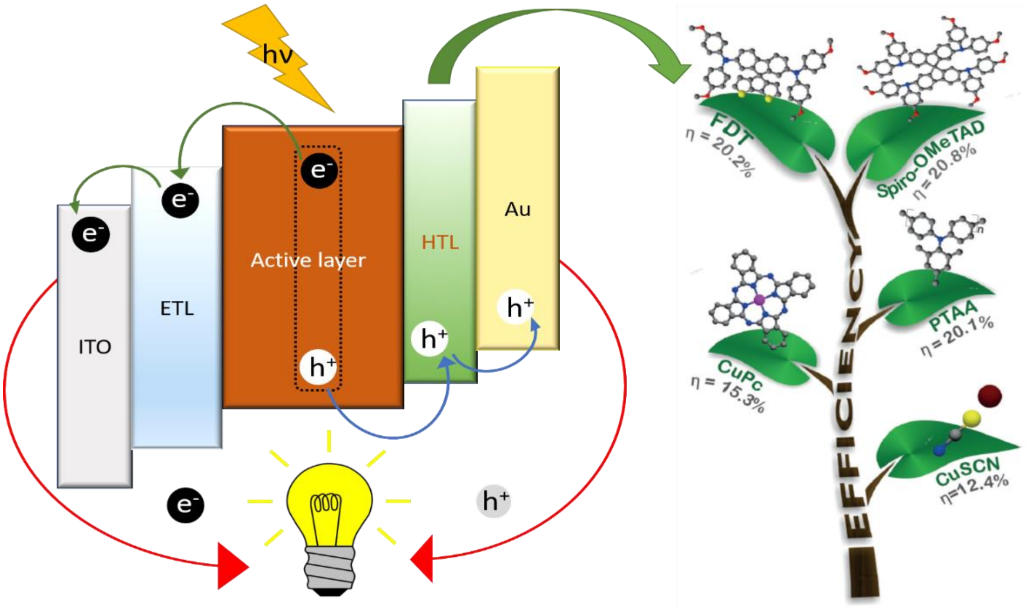

Figure 1.7: Illustration of the charge flow after exciton generation from active layer. The ‘tree’ on the right shows some commonly used HTL in PSCs.

We get four types of solar cell architectures depending upon the position and morphology of HTL and ETL used in device building as shown in Figure 1.7. Taking ETLs first, in the n-i-p, the de facto material has been titanium oxide because of its high band gap and good electron transport properties. TiO_2 could be coated either as a thin layer (80-100 nm) for planar or a mesoporous TiO_2 layer could be deposited from the ethanolic solution of readily available titania nanoparticle paste such as 18 NR-T, WER2-O, 90-TT, etc. An annealing step of 500 °C is required after coating. Low-temperature processed planar PSCs are also prepared by doping the TiO_2 with Niobium or with chlorine.[37] Other materials include SnO_2, ZnO, etc. For p-i-n, it is tricky as the ETL preparation should not compromise the perovskite layer below. So, materials like C_{60} (thermally evaporated), PCBM (Phenyl-C61-butyric acid methyl ester), ZnO nanoparticles have been utilized.[38]

For HTL, along with Spiro-OMeTAD, PTAA (poly (triaryl amine)), P3HT (Poly (3-hexylthiophene-2,5-diyl)[39] have been widely used. Cost-effective copper thiocyanate (CuSCN) suffers from non-dissolution in most solvents. Small molecular HTM such as FDT (fluorene-dithiophene core as a donor and methoxy triphenylamine side groups) have been used with additives to give 20.2% PCE for $(FAPbI_3)_{0.85}(MAPbBr_3)_{0.15}$.[40] For p-i-n architecture, CuSCN again has been used but potentiostatically electrodeposited for thicker film deposition this time around.[41] PEDOT:PSS (poly (3,4-ethylenedioxy thiophene) polystyrene sulfonate), Nickel oxide (NiO_x) are also used as HTL in p-i-n type solar cells development.[42]

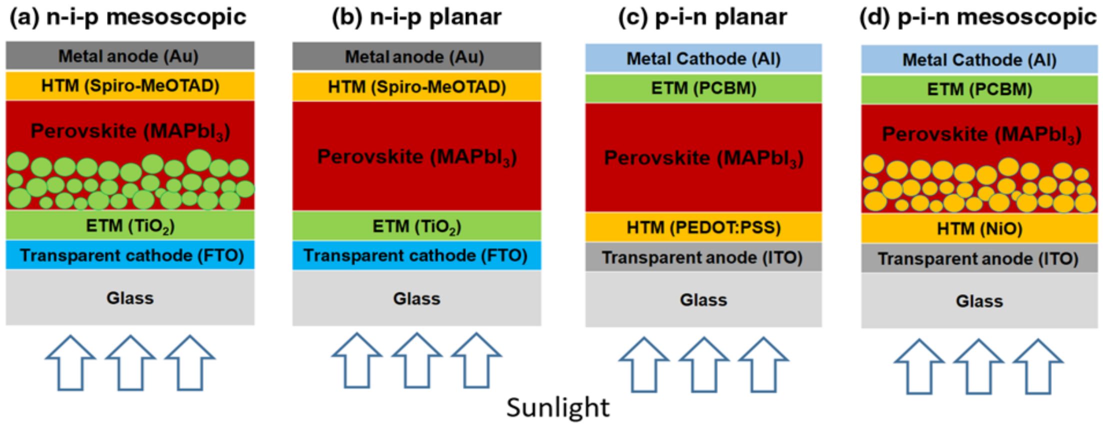

Figure 1.8: PSCs with mesoscopic and planar architecture with normal (n-i-p) and inverted (p-i-n) structures implying flexibility in combinations of electron transport and hole transport materials.

1.3.4 Electrical and Optical Properties of Perovskite

The electronic and optical properties of the perovskite make it a very enviable material. The exciton binding energy of the $MAPbI_3$ perovskite was measured to be around 1-10 meV, effectively rendering the photo generated carriers as free carriers. This coupled with high carrier mobility and long diffusion length (L_D) well into micrometer range leads to decreased recombination losses in solar cells. Beneficial optical properties include high absorption coefficient, direct bandgap transition, and long lifetime. From, L_D ($L_D = \sqrt{D\tau}$), we can estimate diffusion coefficient 'D' for electrons and holes and know which architecture is more suitable. For example, a mesoscopic structure with mesoporous TiO_2 is recommended for $MAPbI_3$. It has been observed that electronic properties discussed above are slightly better in the case of $FAPbI_3$ thus giving an edge to the mixed cation approach over standard $MAPbI_3$.[43] Surface potential plots of polycrystalline $MAPbI_3$ perovskite films show an intergrain potential barrier of ~45 meV in the dark, indicating that charge trapping at grain boundaries is much less of a problem than in CdTe or CIGS who boast a barrier around 100meV-800meV. Similarly, Urbach energy for perovskite is around 15meV much less compared to CIGS (25meV) and marginally higher than GaAs (7meV) which is remarkable for a solution-processed semiconductor.[44]

The recombination of charge carriers can be expressed as $dn/dt = -k_1n-k_2n^2-k_3n^3$ where k_1 is Shockley-Read-Hall (SRH) trapping which is non-radiative recombination rate constant, k_2 is band to band radiative recombination rate constant and k_3 is third-order Auger recombination rate constant and n is electron charge carrier density. The schematics for the processes involved are given in Figure 1.9(a). At low light intensity, we have predominant trap-assisted monomolecular recombination. As the intensity increases, we move towards radiative recombination as all traps are filled now and even higher light intensities lead to Auger type recombination. SRH is trap assisted and leads to a decrease in J_{SC} and V_{OC} of the devices effectively harming the efficiencies. A PCE of 30.5% is expected from a single p-n junction device with V_{OC} and FF approaching the Shockley-Queisser limit of 1.33 V and 0.91 when no non-radiative recombination is present (Figure 1.9(c)). These recombination processes are dependent upon the interfacial interactions (like lattice strain) present in the ETL/Perovskite or Perovskite/HTL boundaries and need to be accounted for in interface engineering.[45]

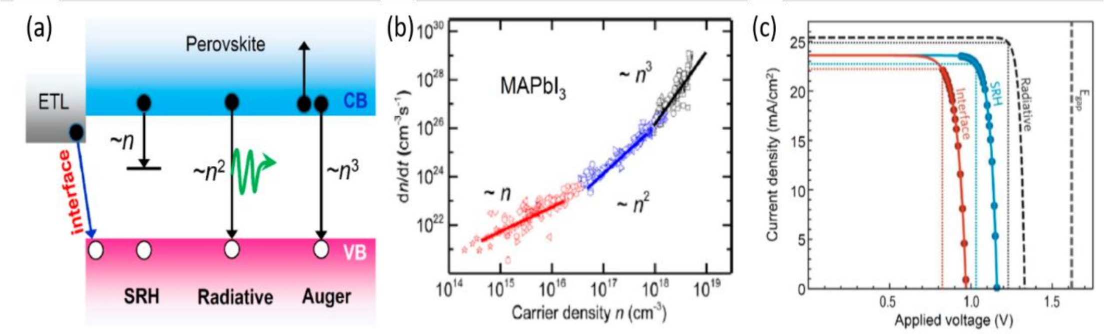

Figure 1.9: (a) Illustration of the different recombination process in PSCs - first-order SRH, second-order radiative, and third-order Auger recombinations (b) From the plot of, dn/dt (recombination rate) as a function of charge density, n, we see various slopes showing the recombination processes for $MAPbI_3$. (c) J-V curve showing the effect of the aforementioned recombination processes.[45]

1.3.5 Film fabrication processes

The performance of the PSCs is majorly dependent on the quality of perovskite in terms of crystallinity and morphology of the films grown. The best performing devices contain perovskite grains with large crystallites devoid of cracks and pinholes. The onus, thus, here lies upon the film fabrication step which utilizes mostly a solution-processed method. The low enthalpy of formation for metal halide perovskites coupled with the high ionic nature of their bonding makes this cost-effective process feasible at low temperatures. As seen in Figure 1.10(a), we see three distinct stages of crystallization of perovskites following the La Mer mechanism. Stage I shows the ions and molecules of perovskite precursors in the solution. As the solvent evaporates during the spin coating, the solution reaches a supersaturated concentration, C_s, forming some nuclei of the perovskites. This nucleation step continues with an increase in crystallite size with solute diffusion in Stage II. As the solution concentration goes below C_s, in Stage III, no more new nuclei are formed and existing crystals increase in size until all precursors are utilized.[46]

In the early years of perovskite research, one-step solution processing was the most used method to grow the active layer. Fairly simple, it required deposition from a homogeneous solution containing all the components in the desired concentration. The films were then heated at around 100-150 °C depending upon the perovskite formed (Figure 1.10(c)). Polar solvents with high dielectric solvents like DMF, DMSO, GBL are preferred in this route. These solvents are not ideal as due to their high boiling points they retard evaporation thus giving non-uniform crystallite sizes or rod and needle structures with poor surface coverage in some cases. This necessitated the removal of solvent rapidly from the film giving rise to techniques like antisolvent treatment, substrate heating, gas blowing, and vacuum treatment (Figure 1.10(e)). Antisolvent method requires flushing of the still spinning perovskite film with a solvent that does not affect the perovskite crystal and has been researched and modified immensely.[47] For example, the addition of methylamine to acetonitrile to decrease defects leading to an efficiency of 18%. Similar efficiency has been achieved by Nie et al., using hot casting method whereby they dropped a 70 °C mixture of PbI_2 and MACl on heated substrates kept at 180 °C.[48]

Figure 1.10(b) shows two step solution processing method in action. The initial step involves the deposition of Pb^{2+} salts onto the substrates and heating at 70 °C followed by exposure to solution or gas form of organic salt and through diffusion (driven by heat) to complete perovskite formation. This provides more control over the crystal growth compared to one step solution-processed method. The first report for this was published by Liang et al., and then Burschka et al. improved it utilizing nanoporous TiO_2 and dipping the prewetted PbI_2 films in a solution of MAI in 2-propanol to achieve 15.0% efficiency with high reproducibility.[31] Other methods also include co-evaporation of precursors in a vacuum chamber for efficient controlled perovskite formation (Figure 1.10 (d)).[49]

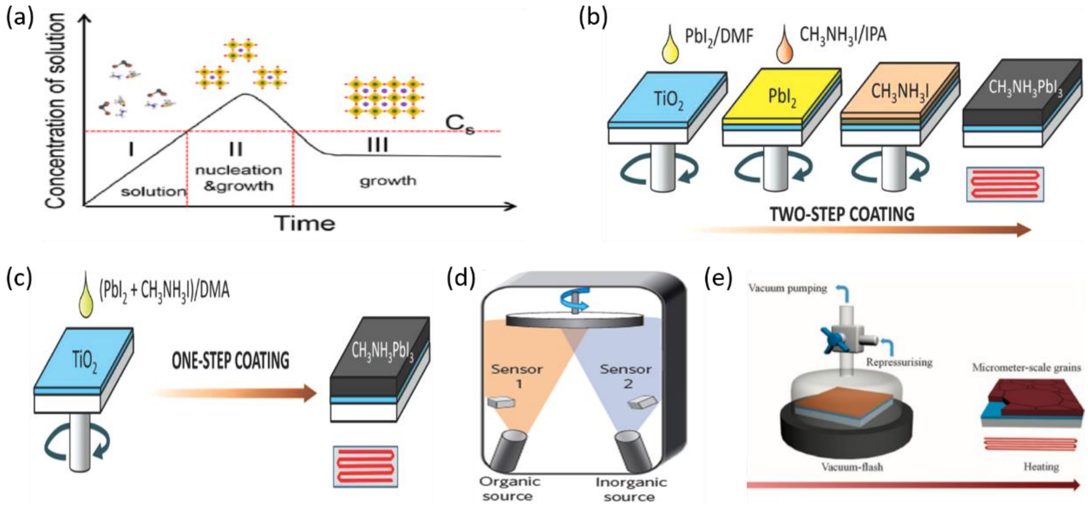

Figure 1.10: (a) Schematic shows the growth of perovskite crystals from solution processing. Different deposition technique for perovskite growth – (b) Two step coating, (c) single step coating, (d) vacuum co-evaporation deposition, and (e) Pressure induced large crystallite growth.

Still there remain many challenges with PSCs chiefly the moisture instability. In presence of water, the perovskite reverts to its precursors irreversibly thus damaging the device and losing performance. Better encapsulation and capping with a hydrophobic layer are some of the options. Lead sources being mostly carcinogenic is another roadblock in perovskite's way to commercialization. Performance of solar cells depends upon the changing weather and thus devices need to be stable in the window of -40 °C to 85 °C. Perovskites still face the issue of degradation at elevated temperature as the metal contact deposited above has the tendency to tunnel through pinholes of an HTM like Spiro-OMeTAD at high temperature (60 °C - 70 °C) and create another pathway for charge movement in the device.[50]

1.4 PbS Colloidal Quantum dot solar cells

1.4.1 Basics of PbS CQDs

Quantum dots have been around since the 1960s though the first report on it was published by Ekimove in 1981 depicting semiconductor crystallites in a glass matrix.[51] In 1996, the first film fabrication of QDs was reported by Smith and co-workers by depositing Ag islands onto a GaAs surface and by the late 1990s commercial production of colloidal quantum dots became feasible.[52] Following this, quantum dots have been researched for potential applications in photovoltaics, LEDs, photoconductors and photodetectors, bioimaging, etc. We have already seen the commercialization of Quantum dot LED TVs (QLEDs) by Samsung. The property which makes these quantum dots so sought-after is the quantum confinement effect which results in bandgap tunability of the semiconductor. Typically, the confinement takes place when the size of the nanoparticle is in the same order as the exciton Bohr radius of the semiconductor. QDs are in the strongest confinement as they are confined in all three spatial coordinates (quasi 0-D) leading to discrete energy level formation which governs the optical and electronic properties of the material.

In a bulk material, electrons and holes are free to move around with no restriction, leading to continuous energy values which are close enough that an energy band is formed. Highest occupied band is called the valence band, the lowest unoccupied band is conduction band and the energy difference between them gives E_g, the bandgap. Bulk semiconductors have density of states, DOS $\propto (E-E_{c/v})^{1/2}$. As seen in Figure 1.11, if the electrons are confined even in a single coordinate, the motion is hindered and the band is lost in favour of step-like density of states forming a quantum well. DOS for electrons in quantum wells having two degrees of freedom is independent of energy. Quantum wire, bound in two dimensions, has a DOS $\propto$ $(E-E_{c/v})^{-1/2}$. As we move from quantum well to quantum wire and finally to a quantum dot, we see the emergence of discrete, quantized energy levels. Here quantum dot possesses atomic-like DOS that is given by a delta function $\delta(E-E_{c/v})$. For this reason, some people refer to QDs as artificial atoms.[53]

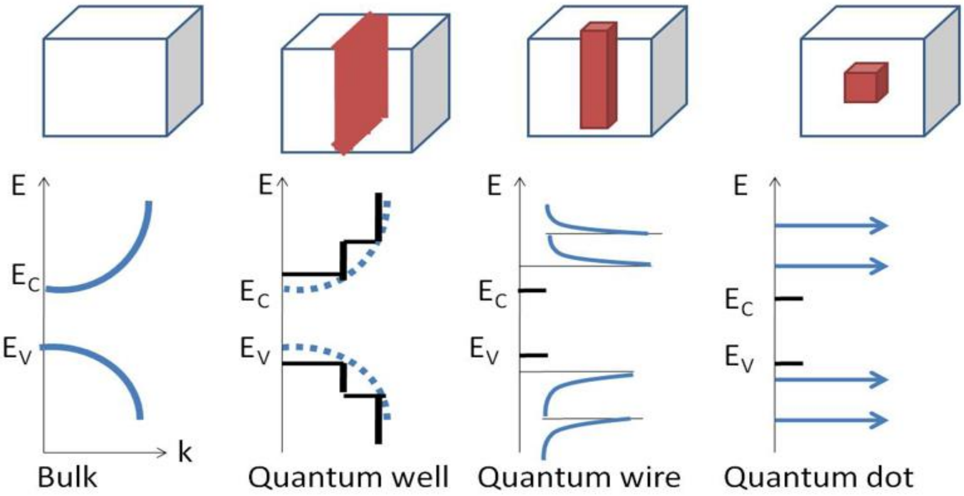

Figure 1.11: Graphic representation of density of states going from bulk material to quantum dot. The conduction and valence bands split into subbands as the system dimensionality is lowered eventually forming discrete energy levels for 0-D QDs.

This leads to size tunability and subsequent handle over the bandgap of the semiconductor. For example, bulk phase PbS has a low E_g value of 0.41 eV, which though absorbing enough sunlight and generating hefty J_{SC}, suffers from an abysmally low V_{OC} and FF. By synthesizing PbS QDs with a size of ~3nm, a bandgap of 1.4 eV is obtained which is more in line with Shockley Quessier limit and thus gives better performance.[54] We will discuss synthetic routes, properties, and advancement in QD technology in the following sections.

1.4.2 Synthesis of PbS CQDs

Quantum dots synthesis can be done through the 'hot injection method' which is facile and low cost (Figure 1.12(a)). This method was first demonstrated by Bawendi and Murray where they synthesized different cadmium QDs with formula CdX (X=S, Se, Te).[55] This method typically involves the rapid injection of the chalcogen precursor into the metal precursor mixed with a non-coordinating solvent (ex. Octadecene, oleylamine) and a long chain surfactant kept at a high temperature and subsequent cooldown (kept in inert atmosphere). By changing either the precursors' concentration or the temperature of the system, different sizes of monodisperse quantum dots can be synthesized here. The growth of the quantum dots follows the LaMer approach here. Fast addition of the chalcogen precursor (at elevated temperature) to the solution causes an increase in concentration of the metal precursors which leads to crossing of nucleation threshold for nanocrystal formation and metal-chalcogen monomers are formed to partially relieve the supersaturation. The surfactant employed here prevents QD agglomeration. After the initial homogeneous diffusion-controlled growth phase (smaller QDs form much faster than larger QDs), Ostwald ripening takes over and size defocusing occurs in remainder of growth phase. In this process, small nuclei dissolve in the solution owing to their high surface energy and the precursors redeposit on larger nanocrystals. Thus, bigger nanocrystals grow further and smaller nuclei fizzle out, providing a high monodispersity of 5-10%. Figure 1.12(b) and 1.12(c) signifies the importance of synthesizing appropriate size QDs as its carryover to the bandgap and change in optical properties caused by the size variation respectively.[56]

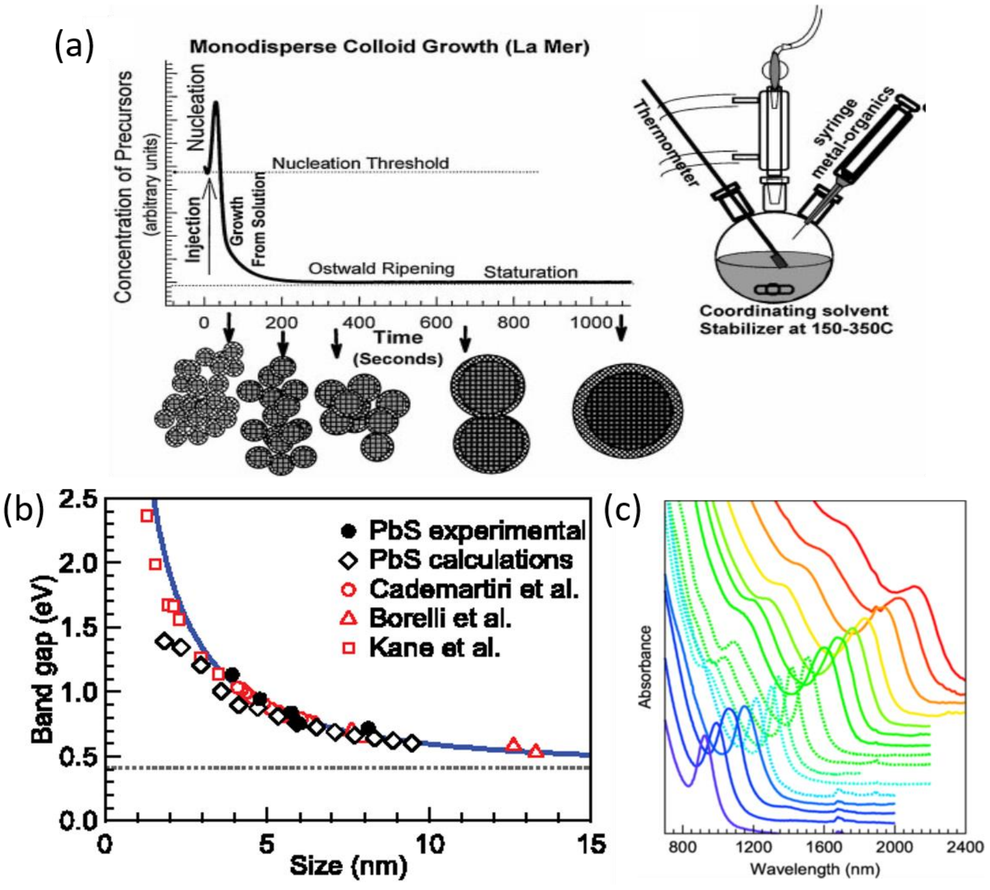

Figure 1.12: (a) Illustration depicting stages of nucleation and growth in the synthesis of monodisperse QDs. (b) Bandgap vs QD size graph. Experimental observations correlate with the calculated values.[57] Bulk bandgap shown with dotted line and (c) Absorbance spectra showing 1st excitonic peak of PbS QDs ranging from 3 to 10 nm.[54]

1.4.3 Evolution of PbS CQDs

The efficiency enhancement in the PbS QDs is directly related to the device architecture evolution and film fabrication changes over the years. The first and the simplest architecture employed was the Schottky architecture (brown label in Figure 1.13(a)) in which a thin layer of QDs is sandwiched between the top metal and bottom transparent conducting oxide (TCO) layer. The first report in QDSC used solid-state ligand exchange (SSE) with EDT ligands to give 1.8% PCE which has recently been boosted to 5.2% using 1,4-benzenedithiol in place of EDT.[58,59] The lower performance caused by the ineffective collection of charge carriers from the back end of the cell and low V_{OC} brought about depleted heterojunction (DHJ) solar cells (blue labels). This concept involving a p-n junction was first used for PbSe QDs coated upon a wide bandgap n-type material (ZnO) to give 1.6% efficiency.[60] Similar approach for PbS QDs resulted in higher J_{SC} and V_{OC} while increasing FF to 55% overcoming the Schottky limitation of charge carrier collection. As the excitons generated at the back end relied upon diffusion to get across, efforts were made to passivate the trap states, enhance diffusion lengths and increase the depletion width of the absorber layer. For example, two step treatment of the QDs where $CdCl_2$ surface treatment is done in solution phase by amines followed by regular SSE method with MPA. This led to an increase in diffusion lengths (>200nm) and an absorber layer of thickness 600 nm gave a high PCE of 9.2% with 29.5 mA/cm^2 J_{SC}.[61] Another stratagem developed to combat the charge extraction issue was the depleted bulk heterojunction architecture which involved the penetration of ZnO nanowires or nanoparticles into the p-type QD layer thus providing a pathway for efficient charge extraction (Figure 1.13(b)). It helped grow a thicker layer of PbS QDs and an efficiency upwards of 10%.[62] The current state-of-the-art PbS QDSCs have an n-i-p structure (red label) where a thin layer of p-type layer (with shallower CBM) is added on top of PbS QDs to prevent the backflow of electrons to metal contact and ferry holes across. So, using a thin layer of p-type EDT-PbS on top of n-type TBAI-PbS resulted in better output as well as improved stability. Crisp et al. replaced the organic TBAI with PbI_2 via SSE post-treatment to make organic-free devices.[63] Later on, halide ions (particularly iodide) were used in the mixed solution exchange process and SSE to achieve 10.2% and recently an efficiency of 12.5% was realized by using only solution state ligand exchange (SLE) with lead halide and hybrid perovskites.[64,65] Colloidal inks thus obtained can be deposited in a single spin coating bypassing the tiresome layer by layer approach. Mixing perovskite with QDs to form n-i-p perovskite QDs solar cell show even higher PCEs of 16% but they are out of the scope of this thesis.[66]

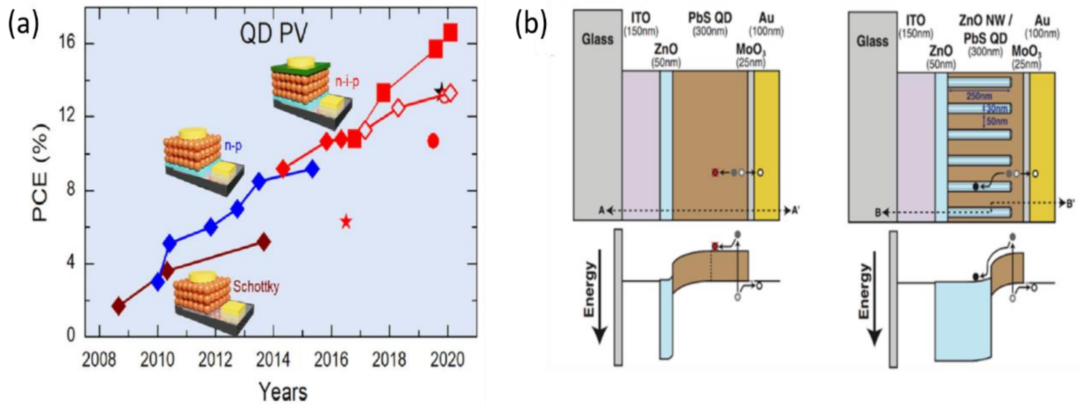

Figure 1.13: (a) PCEs for PbS QD solar cells over the years. The evolution of PCE largely depends upon the architectures over time, Schottky (brown), depleted heterojunction (blue), and n-i-p (red) (b) Illustration of DHJ and depleted bulk heterojunction solar cells.

1.4.4 Passivation of PbS CQDs

The surface ligands used for QD during synthesis perform three main functions - control the growth, prevent agglomeration and electronically passivate the surface. These ligands, like oleic acid which is long-chain fatty acid, are typically insulating and lousy for charge transport and need to be replaced with suitable smaller ligands. The synthesized QDs have then two facets which can be favoured by these shorter ligands – polar (111) surface consisting of only Pb atoms and charge-neutral (200) surface consisting of alternating Pb and S atoms. This then dictates the type of ligand required to passivate a particular facet. X-type ionic ligands (ex. $RCOO^-$, RS^-) passivate PbS-(111) surface whereas, neutral L-type electron donor (ex. RCOOH, RSH) and Z-type electron acceptor (ex. $CdCl_2$) passivate PbS-(100) surface. Passivation by these ligands can be accomplished in two ways, as discussed in the previous section, either by SSE or SLE.

SSE involves flushing the solid film of oleic acid (OA) capped QD with the solution containing the smaller ligand and was first demonstrated by Guyot-Sionnest and later used by Sargent's group for PbS QDs in 2005. TOPO (trioctyl phosphine oxide) ligands capping CdSe QDs were exchanged by diamines and dithiols.[67] As the outgoing ligands are bulky, the volume contraction after the exchange is about 50% which leads to cracks and pinholes in the film even after optimized concentration of small ligands are used. Luther provided a breakthrough by growing a thick film of PbS-EDT through layer by layer approach (LbL) by applying SSE for individual 10-12 thin layers.[68] This succeeded in giving smooth film with reduced interdot distance and efficient charge transport. This method is still widely used for transforming OA/oleylamine capped CsPbX$_3$ QDs to conductive solids for various photovoltaic applications.

Although functional, SSE is tiresome, leads to a lot of chemical wastage, and lacks used in industrial scalability. Recently discovered SLE method though ticks all the right boxes and provides more control over surface passivation. The first report for PbS QDs deposited via this method in single step spin coating was by Ning et al. (PCE = 6%). MAI was taken in DMF and mixed vigorously with OA capped PbS QDs in octane.[69] This led to phase separation and the MAI capped QDs were precipitated and solubilized in low boiling pointy solvent butylamine. This was later modified by using a mixture of MAI and PbI$_2$ as shown in Figure 1.14(a) to obtain a perovskite shelling on QDs boosting performance to 9%.[70] In 2017, first-time PbS QDSCs fabricated via SLE crossed the highest efficiency of SSE devices using PbX$_2$ (X=I and Br) and ammonium acetate (NH$_4$Ac) as precursors in DMF. These devices having PbS QDs capped with PbX$_3^-$/PbX$^+$ gave a PCE of 11.3% (Figure 1.14(b)).[71]

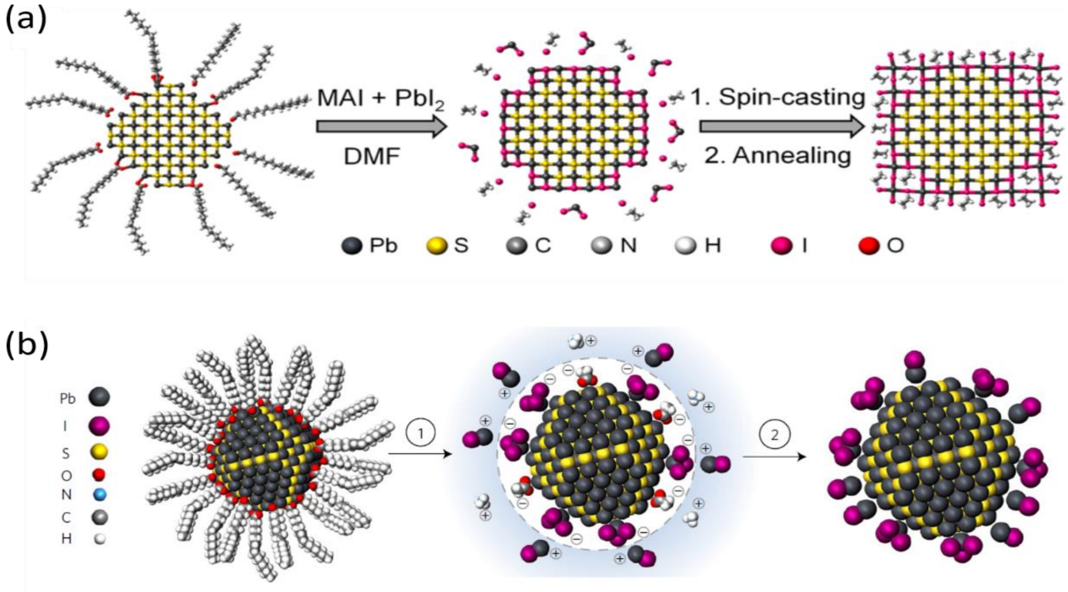

Figure 1.14: (a) Solution ligand exchange and Perovskite-shelling of QDs and (b) PbX$_3^-$ ions being stabilized by NH$_4$Ac after oleic acid is removed (stage 1) and subsequent precipitation removes NH$_4$Ac giving PbX$_3^-$/PbX$^+$ capped CQDs.

Apart from metal halide exchange, atomic-ligand/hybrid passivation[72], another factor that determines the transport properties in CQDs is ‘doping’. Ligands in themselves can act as dopants by altering the carrier concentrations of QDs. As seen from Figure 1.15(a), the nature of doping can be easily assessed by determining the number of excess electrons or holes present in QD. Remote doping can occur as in the case of remote charge transfer leading to excess holes in the system, thus p-doping the QD (scenario iii). In a substitutional doping though (scenario iv), a sulfur atom is exchanged with an iodide atom and the QD has an extra electron, thus n-doping the solid.[73] Iodide ligands passivated PbS QDs have recently shown high carrier mobilities for n-type QDs. Remote passivation with the n-type ZnO was shown by Rath et al., where they demonstrated in a bulk nanoheterojunction system, ZnO nanocrystals can donate electrons to the midgap states of PbS QDs leading to suppression of trap assisted recombination and promoting band-to-band recombination.[74] As the ligand library for QD passivation increases, we get a wide window over which the doping and carrier concentration of QDs can be tuned (Figure 1.15(b)).

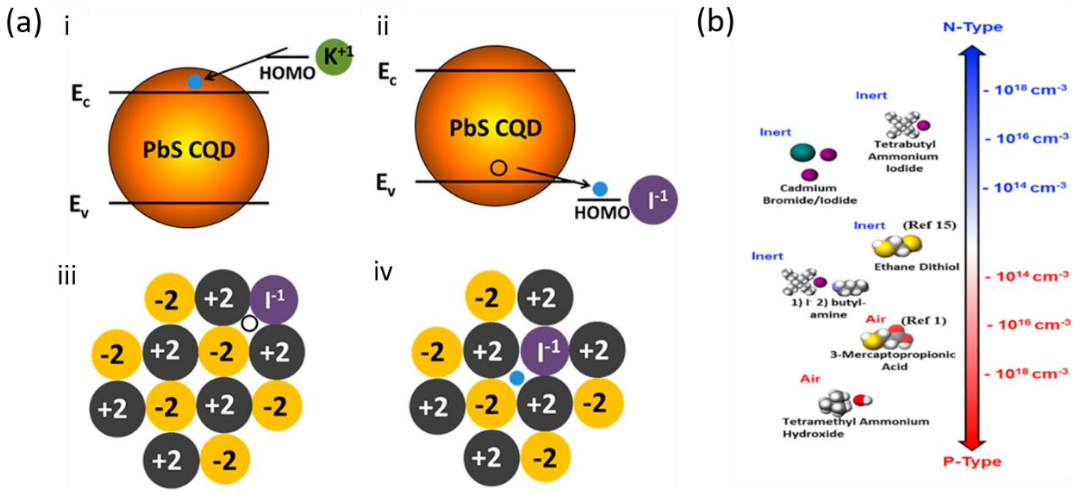

Figure 1.15: (a) Remote doping by different cations and anions. In (i) we see K^+ acting as a donor due to its HOMO level lying above CBM of QD leading to n-doping and when the HOMO level of an anion lies below the VBM of QD, p-doping occurs (ii). (iii) remote and (iv) substitutional doping by iodide ligands. (b) Doping density of PbS QDs with various ligand treatments obtained from FET measurements.[72]

1.4.5 Properties of PbS CQDs

Size-dependent bandgap tunability has been the main motivation behind the research in PbS QDs. A large Bohr radius of PbS (18 nm) enables wide bandgap tunability and by changing the size we can harness the solar spectrum ranging from 300 nm to 1600 nm. Large PbS QDs having bandgap 1 eV can be used to collect the radiation from the NIR range and can be used in tandem with Perovskite or Silicon solar cells.

Lead sulfide QDs also benefit from the direct bandgap, high dielectric constants, high photostability, and large molar extinction coefficients. Additionally, as seen above by changing the ligand passivation strategy we can tune the QDs to either n-type or p-type easily. PbS QD solar cells are highly air-stable as shown in Figure 1.16 which makes them lucrative compared to perovskite solar cells in the third generation.[75]

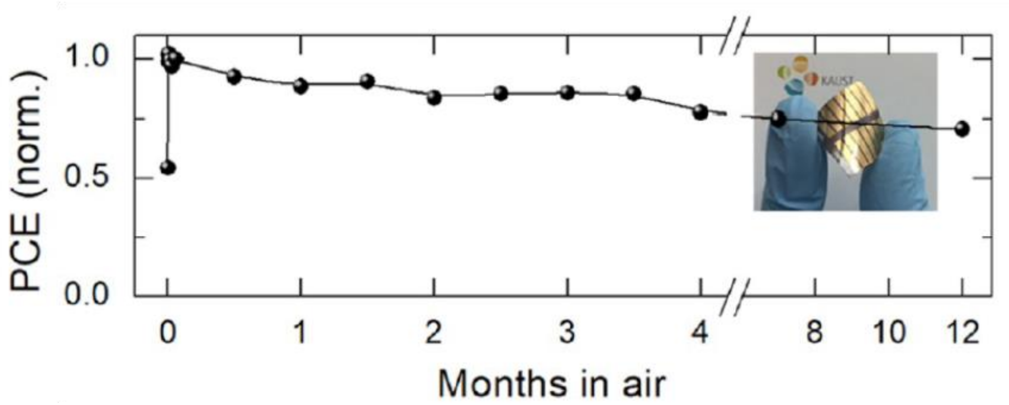

Figure 1.16: Stability of unencapsulated devices kept at high-RH (50−60%) in ambient air for over a year.

1.5 Thesis objectives

The main objectives of the study are to develop high quality Hole transport layers for boosting the performance of $CH_3NH_3PbI_3$ and PbS QD solar cells

- Increasing the grain size in $CH_3NH_3PbI_3$ grown from lead acetate precursor.
- Densification of the most commonly used HTL for perovskite, Spiro-OMeTAD which shows cracks and is prone to moisture damage.
- Improvement in PbS passivation by decreasing the polydispersity and reducing trap states via thiol passivation to achieve a p-type intrinsic layer.
- Alternate cleaning process for the conventional time-consuming PbS-EDT at the top HTL layer

1.6 Thesis outline

This thesis consists of five chapters and outlines the enhancements done to the hole conducting layers of two separate technologies as well as the role of surface passivation in reducing the trap states by introducing a p-type nature to PbS QDs. Chapter

1 (above) introduces perovskite solar cells and PbS QD solar cells along with their beneficial optical and electronic properties. We also see the previous works done to improve the technology

Chapter-2 discusses two-fold modification whereby we introduce antisolvent treatment to the $PbAc_2$ based $CH_3NH_3PbI_3$ and then blend P3HT with Spiro-OMeTAD to obtain a robust HTL thereby improving morphology and reproducibility of devices. The work has been reported:

Sharma, A.; Rath, A. K. Improved Performance and Reproducibility of Perovskite Solar Cells by Jointly Tuning the Hole Transport Layer and the Perovskite Layer Deposition. *J. Mater. Sci. Mater. Electron.* **2018**, *29* (15), 12652–12661. https://doi.org/10.1007/s10854-018-9382-8.

In Chapter-3, the focus is shifted to the emerging NIR-active PbS QDs and its p-type doping through 3-mercaptopropionate passivation which leads to reduced polydispersity and trap states and employing it in the solar cell with n-p-p^+ architecture where p^+ is the PbS QDs exchanged with 1,2-ethandithiol (EDT). The work has been reported:

Sharma, A.; Mahajan, C.; Rath, A. K. Reduction of Trap and Polydispersity in Mutually Passivated Quantum Dot Solar Cells. *ACS Appl. Energy Mater.* **2020**, *3* (9), 8903–8911. https://doi.org/10.1021/acsaem.0c01378.

Chapter-4 involves the replacement of convoluted sequential cleaning of the oleic acid capped PbS QDs by introducing ammonium thiocyanate in methanol to remove oleic acid in a single washing step. This also led to retention in excitonic peak nature and boosts hole mobility as well as p-type doping of the QDs. The work has been reported:

Sharma, A.; Dambhare, N. V; Bera, J.; Sahu, S.; Rath, A. K. Crack-Free Conjugated PbS Quantum Dot–Hole Transport Layers for Solar Cells. *ACS Appl. Nano Mater.* **2021** *4* (4), 4016–4025. https://doi.org/10.1021/acsanm.1c00373.

Chapter-5 summarizes the results of the research work done in the thesis and presents the future directions this research can take.

1.7 References

(1) ISEP Energy chart-December 2018

(2) Energy and Information Administration Annual Energy Outlook 2019

(3) bp Statistical Review of World Energy, 69th edition 2020

(4) "Global Solar Atlas". Retrieved 4 December 2018.

(5) Becquerel, A. E., Mémoire sur les Effets Électriques Produits sous L'influence des Rayons Solaires. Comptes Rendus Séances Hebd. **1839**, 9, 561-567.

(6) Adams W.G.; Day, R.E. The Action of Light on Selenium. *Proc. R. Soc. Lond.* **1877**, 25, 113-117.

(7) Fritts, C. E. (1883). "On a New Form of Selenium Photocell". American Journal of Science. 26: 465.

(8) Heinrich, H. "Ueber einen Einfluss des ultravioletten Lichtes auf die electrische Entladung". *Annalen der Physik.* **1887**, 267 (8), 983–1000.

(9) "April 25, 1954: Bell Labs Demonstrates the First Practical Silicon Solar Cell". APS News. American Physical Society. 18 (4). April 2009

(10) Rohatgi, A. Review of high efficiency silicon solar cells. SPIE Photovoltaics for Commercial Solar Power Applications. **1986**, 706, 15-21.

(11) R. M. Swanson et al., *IEEE Trans. on Electron Devices*, **1984,** 31(5), 661.

(12) Yoshikawa, K.; Kawasaki, H.; Yoshida, W.; Irie, T.; Konishi, K.; Nakano, K.; Uto, T.; Adachi, D.; Kanematsu, M.; Uzu, H.; Yamamoto, K. Silicon Heterojunction Solar Cell with Interdigitated Back Contacts for a Photoconversion Efficiency over 26%. *Nat. Energy* **2017**, *2* (5), 17032.

(13) Meillaud, F.; Boccard, M.; Bugnon, G.; Despeisse, M.; Hänni, S.; Haug, F. J.; Persoz, J.; Schüttauf, J. W.; Stuckelberger, M.; Ballif, C. Recent Advances and Remaining Challenges in Thin-Film Silicon Photovoltaic Technology. *Mater. Today* **2015**, *18* (7), 378–384.

(14) Green, M. A.; Hishikawa, Y.; Dunlop, E. D.; Levi, D. H.; Hohl-Ebinger, J.; Ho-Baillie, A. W. Y. Solar Cell Efficiency Tables (Version 52). *Prog. Photovoltaics Res. Appl.* **2018**, *26* (7), 427–436.

(15) Yablonovitch, E.; Miller, O. D.; Kurtz, S. R. The Opto-Electronic Physics That Broke the Efficiency Limit in Solar Cells. *Conf. Rec. IEEE Photovolt. Spec. Conf.* **2012**, No. 1, 1556–1559.

(16) O'Regan, B.;Gratzel, M. A low-cost, high efficiency solar cell based on dye-sensitized colloidal TiO2 films. Science, 1991, 353, 737-740.

(17) Kakiage, K.; Aoyama, Y.; Yano, T.; Oya, K.; Fujisawa, J. I.; Hanaya, M. Highly-Efficient Dye-Sensitized Solar Cells with Collaborative Sensitization by Silyl-Anchor and Carboxy-Anchor Dyes. *Chem. Commun.* **2015**, *51* (88), 15894–15897.

(18) Wang, W.; Winkler, M. T.; Gunawan, O.; Gokmen, T.; Todorov, T. K.; Zhu, Y.; Mitzi, D. B. Device Characteristics of CZTSSe Thin-Film Solar Cells with 12.6% Efficiency. *Adv. Energy Mater.* **2014**, *4* (7), 1–5.

(19) Keaens, D.; Calvin, M. Photovoltaic Effect and Photoconductivity in Laminated Organic Systems. *J. Chem. Phys.* **1958**, *29* (4), 950–951.

(20) Cui, Y.; Yao, H.; Zhang, J.; Zhang, T.; Wang, Y.; Hong, L.; Xian, K.; Xu, B.; Zhang, S.; Peng, J.; Wei, Z.; Gao, F.; Hou, J. Over 16% Efficiency Organic Photovoltaic Cells Enabled by a Chlorinated Acceptor with Increased Open-Circuit Voltages. *Nat. Commun.* **2019**, *10* (1), 1–8.

(21) Meng, L.; Zhang, Y.; Wan, X.; Li, C.; Zhang, X.; Wang, Y.; Ke, X.; Xiao, Z.; Ding, L.; Xia, R.; Yip, H. L.; Cao, Y.; Chen, Y. Organic and Solution-Processed Tandem Solar Cells with 17.3% Efficiency. *Science.* **2018**, *361* (6407), 1094–1098.

(22) Miyasaka, T.; Kojima, A.; Teshima, K.; Shirai, Y. Organometal Halide Perovskites as Visible-Light Sensitizers for Photovoltaic Cells. *J. Am. Chem. Soc.* **2009**, *131* (17), 6050–6051.

(23) Green, M. A.; Hishikawa, Y.; Dunlop, E. D.; Levi, D. H.; Hohl-Ebinger, J.; Yoshita, M.; Ho-Baillie, A. W. Y. Solar Cell Efficiency Tables (Version 53). *Prog. Photovoltaics Res. Appl.* **2019**, *27* (1), 3–12.

(24) Grätzel, M. Mesoscopic $CH_3NH_3PbI_3$/TiO 2 Heterojunction Solar Cells. **2012**, 8–11.

(25) Sun, B.; Johnston, A.; Xu, C.; Wei, M.; Huang, Z.; Jiang, Z.; Zhou, H.; Gao, Y.; Dong, Y.; Ouellette, O.; Zheng, X.; Liu, J.; Choi, M. J.; Gao, Y.; Baek, S. W.; Laquai, F.; Bakr, O. M.; Ban, D.; Voznyy, O.; García de Arquer, F. P.; Sargent, E. H. Monolayer Perovskite Bridges Enable Strong Quantum Dot Coupling for Efficient Solar Cells. *Joule* **2020**, *4* (7), 1542–1556.

(26) Dieter, W. $CH_3NH_3PbX_3$, Ein Pb(II)-System Mit Kubischer Perowskitstruktur / $CH_3NH_3PbX_3$, a Pb(II)-System with Cubic Perovskite Structure. *Zeitschrift für Naturforsch. B* **1978**, *33* (12), 1443–1445.

(27) Green, M. A.; Ho-Baillie, A.; Snaith, H. J. The Emergence of Perovskite Solar Cells. *Nat. Photonics* **2014**, *8* (7), 506–514.

(28) Im, J. H.; Lee, C. R.; Lee, J. W.; Park, S. W.; Park, N. G. 6.5% Efficient Perovskite Quantum-Dot-Sensitized Solar Cell. *Nanoscale* **2011**, *3* (10), 4088–4093.

(29) Kim, H.-S.; Lee, C.-R.; Im, J.-H.; Lee, K.-B.; Moehl, T.; Marchioro, A.; Moon, S.-J.; Humphry-Baker, R.; Yum, J.-H.; Moser, J. E.; Grätzel, M.; Park, N.-G. Lead Iodide Perovskite Sensitized All-Solid-State Submicron Thin Film Mesoscopic Solar Cell with Efficiency Exceeding 9%. *Sci. Rep.* **2012**, *2*, 591.

(30) Jeong, J.; Kim, M.; Seo, J.; Lu, H.; Ahlawat, P.; Mishra, A.; Yang, Y.; Hope, M. A.; Eickemeyer, F. T.; Kim, M.; Yoon, Y. J.; Choi, I. W.; Darwich, B. P.; Choi, S. J.; Jo, Y.; Lee, J. H.; Walker, B.; Zakeeruddin, S. M.; Emsley, L.; Rothlisberger, U.; Hagfeldt, A.; Kim, D. S.; Grätzel, M.; Kim, J. Y. Pseudo-Halide Anion Engineering for α-FAPbI3 Perovskite Solar Cells. *Nature* **2021**, *592* (7854), 381–385.

(31) Burschka, J.; Pellet, N.; Moon, S. J.; Humphry-Baker, R.; Gao, P.; Nazeeruddin, M. K.; Grätzel, M. Sequential Deposition as a Route to High-Performance Perovskite-Sensitized Solar Cells. *Nature* **2013**, *499* (7458), 316–319.

(32) Zhang, W.; Saliba, M.; Moore, D. T.; Pathak, S. K.; Hörantner, M. T.; Stergiopoulos, T.; Stranks, S. D.; Eperon, G. E.; Alexander-Webber, J. A.; Abate, A.; Sadhanala, A.; Yao, S.; Chen, Y.; Friend, R. H.; Estroff, L. A.; Wiesner, U.; Snaith, H.

J. Ultrasmooth Organic-Inorganic Perovskite Thin-Film Formation and Crystallization for Efficient Planar Heterojunction Solar Cells. *Nat. Commun.* **2015**, *6*.

(33) Konstantakou, M.; Stergiopoulos, T. A Critical Review on Tin Halide Perovskite Solar Cells. *J. Mater. Chem. A* **2017**, *5* (23), 11518–11549.

(34) Smith, I. C.; Hoke, E. T.; Solis-Ibarra, D.; McGehee, M. D.; Karunadasa, H. I. A Layered Hybrid Perovskite Solar-Cell Absorber with Enhanced Moisture Stability. *Angew. Chemie - Int. Ed.* **2014**, *53* (42), 11232–11235.

(35) Hu, Y.; Schlipf, J.; Wussler, M.; Petrus, M. L.; Jaegermann, W.; Bein, T.; Müller-Buschbaum, P.; Docampo, P. Hybrid Perovskite/Perovskite Heterojunction Solar Cells. *ACS Nano* **2016**, *10* (6), 5999–6007.

(36) Tsai, H.; Nie, W.; Blancon, J. C.; Stoumpos, C. C.; Asadpour, R.; Harutyunyan, B.; Neukirch, A. J.; Verduzco, R.; Crochet, J. J.; Tretiak, S.; Pedesseau, L.; Even, J.; Alam, M. A.; Gupta, G.; Lou, J.; Ajayan, P. M.; Bedzyk, M. J.; Kanatzidis, M. G.; Mohite, A. D. High-Efficiency Two-Dimensional Ruddlesden-Popper Perovskite Solar Cells. *Nature* **2016**, *536* (7616), 312–317.

(37) Mandal, D.; Goswami, P. N.; Rath, A. K. Application in Quantum Dot Solar Cells Colossal Photo-Conductive Gain in Low Temperature Processed TiO 2 Films and Their Application in Quantum Dot Solar Cells. **2017**, *123902*.

(38) Song, J.; Liu, L.; Wang, X. F.; Chen, G.; Tian, W.; Miyasaka, T. Highly Efficient and Stable Low-Temperature Processed ZnO Solar Cells with Triple Cation Perovskite Absorber. *J. Mater. Chem. A* **2017**, *5* (26), 13439–13447.

(39) Zhang, Y.; Elawad, M.; Yu, Z.; Jiang, X.; Lai, J.; Sun, L. Enhanced Performance of Perovskite Solar Cells with P3HT Hole-Transporting Materials: Via Molecular p-Type Doping. *RSC Adv.* **2016**, *6* (110), 108888–108895.

(40) Saliba, M.; Orlandi, S.; Matsui, T.; Aghazada, S.; Cavazzini, M.; Correa-Baena, J. P.; Gao, P.; Scopelliti, R.; Mosconi, E.; Dahmen, K. H.; De Angelis, F.; Abate, A.; Hagfeldt, A.; Pozzi, G.; Graetzel, M.; Nazeeruddin, M. K. A Molecularly Engineered Hole-Transporting Material for Efficient Perovskite Solar Cells. *Nat. Energy* **2016**, *1* (2), 1–7.

(41) Ye, S.; Sun, W.; Li, Y.; Yan, W.; Peng, H.; Bian, Z.; Liu, Z.; Huang, C. CuSCN-Based Inverted Planar Perovskite Solar Cell with an Average PCE of 15.6%. *Nano Lett.* **2015**, *15* (6), 3723–3728.

(42) You, J.; Meng, L.; Song, T. Bin; Guo, T. F.; Chang, W. H.; Hong, Z.; Chen, H.; Zhou, H.; Chen, Q.; Liu, Y.; De Marco, N.; Yang, Y. Improved Air Stability of Perovskite Solar Cells via Solution-Processed Metal Oxide Transport Layers. *Nat. Nanotechnol.* **2016**, *11* (1), 75–81.

(43) Kim, J. Y.; Lee, J. W.; Jung, H. S.; Shin, H.; Park, N. G. High-Efficiency Perovskite Solar Cells. *Chem. Rev.* **2020**, *120* (15), 7867–7918.

(44) De Wolf, S.; Holovsky, J.; Moon, S. J.; Löper, P.; Niesen, B.; Ledinsky, M.; Haug, F. J.; Yum, J. H.; Ballif, C. Organometallic Halide Perovskites: Sharp Optical Absorption Edge and Its Relation to Photovoltaic Performance. *J. Phys. Chem. Lett.* **2014**, *5* (6), 1035–1039.

(45) Sarritzu, V.; Sestu, N.; Marongiu, D.; Chang, X.; Masi, S.; Rizzo, A.; Colella, S.; Quochi, F.; Saba, M.; Mura, A.; Bongiovanni, G. Optical Determination of Shockley-Read-Hall and Interface Recombination Currents in Hybrid Perovskites. *Sci. Rep.* **2017**, *7* (January), 1–10.

(46) Lee, J. W.; Lee, D. K.; Jeong, D. N.; Park, N. G. Control of Crystal Growth toward Scalable Fabrication of Perovskite Solar Cells. *Adv. Funct. Mater.* **2019**, *29* (47), 1–18.

(47) Jeon, N. J.; Noh, J. H.; Kim, Y. C.; Yang, W. S.; Ryu, S.; Seok, S. Il. Solvent Engineering for High-Performance Inorganic-Organic Hybrid Perovskite Solar Cells. *Nat. Mater.* **2014**, *13* (9), 897–903.

(48) Nie, W.; Tsai, H.; Asadpour, R.; Neukirch, A. J.; Gupta, G.; Crochet, J. J.; Chhowalla, M.; Tretiak, S.; Alam, M. A.; Wang, H. High-Efficiency Solution-Processed Perovskite Solar Cells with Millimeter-Scale Grains. *Science*, **2015**, *347* (6221), 522–526.

(49) Liu, M.; Johnston, M. B.; Snaith, H. J. Efficient Planar Heterojunction Perovskite Solar Cells by Vapour Deposition. *Nature* **2013**, *501* (7467), 395–398.

(50) Domanski, K.; Correa-Baena, J. P.; Mine, N.; Nazeeruddin, M. K.; Abate, A.; Saliba, M.; Tress, W.; Hagfeldt, A.; Grätzel, M. Not All That Glitters Is Gold: Metal-Migration-Induced Degradation in Perovskite Solar Cells. *ACS Nano* **2016**, *10* (6), 6306–6314.

(51) Ekimov, A.; Onushchenko, A. Quantum Size Effect in Three-Dimensional Microscopic Semiconductor Crystals. *Jetp Lett* **1981**, *34* (6), 345–349.

(52) Smith, A. R.; Chao, K. J.; Niu, Q.; Shih, C. K. Formation of Atomically Flat Silver Films on GaAs with a “silver Mean” Quasi Periodicity. *Science.* **1996**, *273* (5272), 226–228.

(53) Kosyachenko, K. E. J. E.-L. A. Quantum Dots Solar Cells; IntechOpen: Rijeka, 2015; p Ch. 11.

(54) Moreels, I.; Justo, Y.; Geyter, B. De; Haustraete, K.; Martins, J. C.; Hens, Z. Quantum Dots: A Surface Chemistry Study. *ACS Nano* **2012**, *5* (3), 2004–2012.

(55) Murray, C. B.; Norris, D. J.; Bawendi, M. G. Synthesis and Characterization of Nearly Monodisperse CdE (E = Sulfur, Selenium, Tellurium) Semiconductor Nanocrystallites. *J. Am. Chem. Soc.* **1993**, *115* (19), 8706–8715.

(56) Murray, C. B.; Kagan, R.; Bawendi M. G. Synthesis And Characterization Of Monodisperse Nanocrystals And Close-Packed Nanocrystal Assemblies. *Annu. Rev. Mater. Sci.* **2006**, *30*, 545–610.

(57) Moreels, I.; Lambert, K.; Smeets, D.; De Muynck, D.; Nollet, T.; Martins, J. C.; Vanhaecke, F.; Vantomme, A.; Delerue, C.; Allan, G.; Hens, Z. Size-Dependent Optical Properties of Colloidal PbS Quantum Dots. *ACS Nano* **2009**, *3* (10), 3023–3030.

(58) Luther, J. M.; Law, M.; Beard, M. C.; Song, Q.; Reese, M. O.; Ellingson, R. J.; Nozik, A. J. Schottky Solar Cells Based on Colloidal Nanocrystal Films. *Nano Lett.* **2008**, *8* (10), 3488–3492.

(59) Piliego, C.; Protesescu, L.; Bisri, S. Z.; Kovalenko, M. V.; Loi, M. A. 5.2% Efficient PbS Nanocrystal Schottky Solar Cells. *Energy Environ. Sci.* **2013**, *6* (10), 3054–3059.

(60) Leschkies, K. S.; Beatty, T. J.; Kang, M. S.; Norris, D. J.; Aydil, E. S. Solar Cells Based on Junctions between Colloidal Pbse Nanocrystals and Thin ZnO Films. *ACS Nano* **2009**, *3* (11), 3638–3648.

(61) Carey, G. H.; Levina, L.; Comin, R.; Voznyy, O.; Sargent, E. H. Record Charge Carrier Diffusion Length in Colloidal Quantum Dot Solids via Mutual Dot-to-Dot Surface Passivation. *Adv. Mater.* **2015**, *27* (21), 3325–3330.

(62) Shi, G.; Kaewprajak, A.; Ling, X.; Hayakawa, A.; Zhou, S.; Song, B.; Kang, Y. W.; Hayashi, T.; Altun, M. E.; Nakaya, M.; Liu, Z.; Wang, H.; Sagawa, T.; Ma, W. Finely Interpenetrating Bulk Heterojunction Structure for Lead Sulfide Colloidal Quantum Dot Solar Cells by Convective Assembly. *ACS Energy Lett.* **2019**, *4* (4), 960–967. (62)

(63) Crisp, R. W.; Kroupa, D. M.; Marshall, A. R.; Miller, E. M.; Zhang, J.; Beard, M. C.; Luther, J. M. Metal Halide Solid-State Surface Treatment for High Efficiency PbS and PbSe QD Solar Cells. *Sci. Rep.* **2015**, *5*, 9945.

(64) Lan, X.; Voznyy, O.; Kiani, A.; García De Arquer, F. P.; Abbas, A. S.; Kim, G. H.; Liu, M.; Yang, Z.; Walters, G.; Xu, J.; Yuan, M.; Ning, Z.; Fan, F.; Kanjanaboos, P.; Kramer, I.; Zhitomirsky, D.; Lee, P.; Perelgut, A.; Hoogland, S.; Sargent, E. H. Passivation Using Molecular Halides Increases Quantum Dot Solar Cell Performance. *Adv. Mater.* **2016**, *28* (2), 299–304.

(65) Xu, J.; Voznyy, O.; Liu, M.; Kirmani, A. R.; Walters, G.; Munir, R.; Abdelsamie, M.; Proppe, A. H.; Sarkar, A.; García De Arquer, F. P.; Wei, M.; Sun, B.; Liu, M.; Ouellette, O.; Quintero-Bermudez, R.; Li, J.; Fan, J.; Quan, L.; Todorovic, P.; Tan, H.; Hoogland, S.; Kelley, S. O.; Stefik, M.; Amassian, A.; Sargent, E. H. 2D Matrix Engineering for Homogeneous Quantum Dot Coupling in Photovoltaic Solids. *Nat. Nanotechnol.* **2018**, *13* (6), 456–462.

(66) Zhao, Q.; Hazarika, A.; Chen, X.; Harvey, S. P.; Larson, B. W.; Teeter, G. R.; Liu, J.; Song, T.; Xiao, C.; Shaw, L.; Zhang, M.; Li, G.; Beard, M. C.; Luther, J. M. High Efficiency Perovskite Quantum Dot Solar Cells with Charge Separating Heterostructure. *Nat. Commun.* **2019**, *10* (1).

(67) Guyot-Sionnest, P.; Wang, C. Fast Voltammetric and Electrochromic Response of Semiconductor Nanocrystal Thin Films. *J. Phys. Chem. B* **2003**, *107* (30), 7355–7359.

(68) Luther, J. M.; Law, M.; Song, Q.; Perkins, C. L.; Beard, M. C.; Nozik, A. J. Structural , Optical , and Electrical Properties of Self-Assembled Films of PbSe Nanocrystals Treated With 1,2-Ethanedithiol. **2008**, *2* (2), 271–280.

(69) Ning, Z.; Dong, H.; Zhang, Q.; Voznyy, O.; Sargent, E. H. Solar Cells Based on Inks of N-Type Colloidal Quantum Dots. *ACS Nano* **2014**, *8* (10), 10321–10327.

(70) Yang, Z.; Janmohamed, A.; Lan, X.; García de Arquer, F. P.; Voznyy, O.; Yassitepe, E.; Kim, G.-H.; Ning, Z.; Gong, X.; Comin, R.; Sargent, E. H. Colloidal Quantum Dot Photovoltaics Enhanced by Perovskite Shelling. *Nano Lett.* **2015**, *15* (11), 7539–7543.

(71) Liu, M.; Voznyy, O.; Sabatini, R.; García de Arquer, F. P.; Munir, R.; Balawi, A. H.; Lan, X.; Fan, F.; Walters, G.; Kirmani, A. R.; Hoogland, S.; Laquai, F.; Amassian, A.; Sargent, E. H. Hybrid Organic–Inorganic Inks Flatten the Energy Landscape in Colloidal Quantum Dot Solids. *Nat. Mater.* **2016**, *16*, 258.

(72) Tang, J.; Kemp, K. W.; Hoogland, S.; Jeong, K. S.; Liu, H.; Levina, L.; Furukawa, M.; Wang, X.; Debnath, R.; Cha, D.; Chou, K. W.; Fischer, A.; Amassian, A.; Asbury, J. B.; Sargent, E. H. Colloidal-Quantum-Dot Photovoltaics Using Atomic-Ligand Passivation. *Nat. Mater.* **2011**, *10*, 765–771.

(73) Voznyy, O.; Zhitomirsky, D.; Stadler, P.; Ning, Z.; Hoogland, S.; Sargent, E. H. A Charge-Orbital Balance Picture of Doping in Colloidal Quantum Dot Solids. *ACS Nano* **2012**, *6* (9), 8448–8455.

(74) Rath, A. K.; Arquer, F. P. G. De; Stavrinadis, A.; Lasanta, T.; Bernechea, M.; Diedenhofen, S. L.; Konstantatos, G. Remote Trap Passivation in Colloidal Quantum Dot Bulk Nano-Heterojunctions and Its Effect in Solution-Processed Solar Cells. **2014**, 4741–4747.

(75) Kirmani, A. R.; Sheikh, A. D.; Niazi, M. R.; Haque, M. A.; Liu, M.; de Arquer, F. P. G.; Xu, J.; Sun, B.; Voznyy, O.; Gasparini, N.; Baran, D.; Wu, T.; Sargent, E. H.; Amassian, A. Overcoming the Ambient Manufacturability-Scalability-Performance Bottleneck in Colloidal Quantum Dot Photovoltaics. *Adv. Mater.* **2018**, *30* (35), 1–9.

Chapter 2

Improved performance and reproducibility of perovskite solar cells by jointly tuning the hole transport layer and the perovskite layer deposition

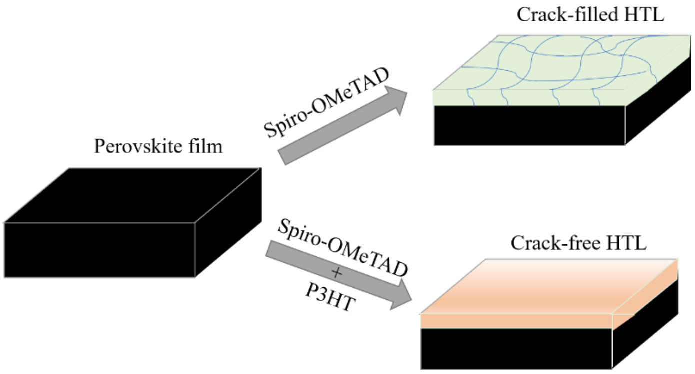

Abstract:

Solution-processed organometal trihalide materials, commonly referred to as perovskites, have gained enormous popularity due to their unprecedented performance in photovoltaic applications. However, submicron thick perovskite films are susceptible to the formation of cracks, pinholes – like morphological defects; the traits stemming from their solution-phase processing and subsequent crystallization. The issue carries forward to pinholes and cracks in the thin film of spin coated hole transport layer, Spiro-OMeTAD, which by forming these micro-shorts reduces the performance reliability and weakens the defense against moisture ingress to the intrinsic layer. For the large-scale processing and employment of perovskite solar cell from the prudent solution phase processing, morphological fallibility of both perovskite and hole transport layers need an urgent address. Usage of a non-conventional lead precursor (lead acetate) and subsequent anti-solvent treatment during film deposition, lead us to form pinhole-free and compact perovskite film. Crack-free hole conducting layer is achieved utilizing a blend of Spiro-OMeTAD and a conducting polymer without compromising the solar cell performance. A detailed investigation of the charge transport and charge extraction properties of the thus developed hole transport layer has been carried out. The developed $CH_3NH_3PbI_3$ based perovskite solar cells show improved performance and duplicability.

Chapter 2: Improved performance and reproducibility of perovskite solar cells by jointly tuning the hole transport layer and the perovskite layer deposition

2.1 Introduction

The discovery and subsequent meteoric rise in perovskite solar cells have helped boost the global green energy drive largely thanks to the immense interest and participation of groups all around the world.[1-4] Electronic properties like high carrier mobility[5], long recombination lifetime[6], ambipolar transport, high carrier diffusion length[6,7], and consequent high open-circuit voltage (V_{OC})[8,9] make perovskite a very bankable material for the next generation solar cell development. Development of various film deposition strategies along with device architectural platforms has led to the rapid improvement for perovskite solar cells and attain high power conversion efficiency (PCE). In recent past, utilizing the phenylethylammonium iodide passivation in formamidinium and methyl ammonium-based 3D perovskite ($FA_{1-x}MA_xPbI_3$)[10] have resulted in the highest PCE of 23.3%, whereas the highest reported efficiency in $CH_3NH_3PbI_3$ perovskite is around 18%.[4,11] $CH_3NH_3PbI_3$, first introduced by Kojima et al. in DSSC architecture[12], has been the choice of sensitizer and most widely studied perovskite material due to its ease in one step solution processing.[13] This processing of $CH_3NH_3PbI_3$ material has implicit implications in tuning the material electronic and surface properties which in turn regulate its performance in the eventual solar cells.[14] For instance, commonly used halide-based lead precursors (PbI_2, $PbBr_2$, and $PbCl_2$) illustrate high PCE compared to non-halide sources like lead acetate ($PbAc_2$) and lead thiocyanate.[15] However, perovskite films from non-halide sources are smoother and reproducible[15]; qualities deemed crucial for large-scale industry manufacturing and commercialization. Coming from DSSC architecture, the importance of an appropriate hole transport layer (HTL) in the stability and performance of perovskite solar cells is evident when the liquid electrolyte is replaced by the solid-state material 2,2′,7,7′-Tetrakis-(*N*,*N*-di-4-methoxyphenylamino)-9,9′-spirobifluorene (Spiro-OMeTAD).[16] Since then a number of HTLs are developed and implemented in the perovskite solar cells inclusive of aforementioned Spiro-OMeTAD, poly(triarylamine) (PTAA)[17], Poly(3-hexylthiophene-2,5-diyl) (P3HT)[18], CuSCN[19], CuI[20], Cu_2O[21], NiO[22,23] (p-i-n architecture) etc. Organic Spiro-OMeTAD yields high PCE in perovskite solar cells and consequently has been the most widely used HTL as of today. Reports, still, have shown that Spiro-OMeTAD has some serious limitations in terms of morphology, reproducibility, and large area deposition.[24] Primarily the deposition of Spiro-OMeTAD from chlorobenzene solution leads to morphological deformities as in reduced surface coverage leading to pinhole formation. This is detrimental to the performance and reproducibility of solar cells, as shown by Domanski et al., where they reported the seeping in of the top gold electrode through these pinholes and forming micro-shorts with the perovskite layer.[25] Large surface area deposition is expected to be the worst affected due to this issue. Furthermore, the pinholes which are not covered by the electrode, and hence are not filled, also lead to moisture ingress and consequent fast degradation of intrinsic perovskite layer leading to a sub-optimal performance in ambient conditions. Polymer P3HT is one other widely studied hole transport material in organic solar cells and forms compact and smooth films from solution-phase deposition.[26,27] It is, when compared to Spiro-OMeTAD, inferior in performance when used as HTL for perovskite solar cells pertaining to low mobility.[28]

In our effort to address the pinhole and micro shorts formation in solution-processed perovskite solar cells to achieve reliable and efficient solar cells, we have focused both on active perovskite layer deposition and HTL layer formation in tandem. In solution-phase perovskite film deposition, the evaporation of solvent molecules, organic residue, and the volume contraction caused by the crystallization of perovskite films bring in effect the cracks and pinholes in the film which are detrimental to both performance and reproducibility.[29] To combat this, various approaches have been tried namely two step deposition (with lead iodide, PbI_2)[30], hot casting[31], mixed solvent for deposition[32] as well as usage of mesoporous titanium dioxide (TiO_2) layer rather than planar TiO_2. From the commercial perspective, to have reproducibility over a large area, it is more facile to have a single step single solvent deposition at ambient conditions. Conventional PbI_2 and $PbCl_2$ lead sources form larger crystallites that yield high PCE but suffer from a high degree of porosity and longer annealing times.[33] Thus, we chose $PbAc_2$ as the lead precursor and methylammonium iodide as iodide source to form the smooth and compact perovskite films. $PbAc_2$ based films require lower annealing temperature as well as lower duration for perovskite crystallization in contrast to the conventional lead halide-based films as the by-product methylammonium acetate (CH_3NH_3Ac) formed in this case is highly volatile.[15,34] These films, deprived of temperature-induced anomalies show lesser defects (structural and electronic), however, generate smaller grain boundaries (< 1 μm).[15,34] For solar cell application, larger crystallites are sought after for faster transportation and suppressed recombination of photogenerated carriers.

In this chapter, we demonstrate that the grain size of perovskite crystals obtained from $PbAc_2$ can be modulated by tuning the precursor concentration for larger grain sizes and treating the perovskite films with an anti-solvent during the deposition process. This approach led to the formation of smooth films with an increasingly reduced amount of pinholes and cracks and better charge transport. Moving above to the HTL, pinholes, and cracks evident in the Spiro-OMeTAD layer are eliminated by blending Spiro-OMeTAD with polymer poly(3-hexylthiophene-2,5-diyl), commonly known as P3HT. Optimizing the P3HT: Spiro-OMeTAD blend ratio leads to both high solar cell performance and better reproducibility. From surface characterizations SEM and mobility measurements, we show that at optimum blend ratio we obtain good film morphology with no cracks and high hole mobility value obtained to explain their superior performance in solar cells.

2.2 Experimental Details

2.2.1 Substrate preparation

Transparent conductive FTO substrates were partially etched with ZnO/HCl mixture before being sequentially cleaned with soap solution, deionized water, acetone, and boiled in isopropanol. Substrates were dried with a hot gun and kept for ETL coating.

2.2.2 Electron Transport Layer (ETL) preparation

Compact titanium oxide (TiO_2) was utilized as the ETL in this study. Sol-gel was prepared as reported before but concentration was optimized, 369 µL (1.2 mmol) of titanium isopropoxide was added to 2.53 mL of 2-propanol and stirred for 12 hours.[35] 14 µL of 5 N HCl in water was added dropwise to the stirring solution followed by another 2.53 mL of 2-propanol. Solution was stirred for the next 12 hours till it was transparent and no turbidity was noticed. Planar TiO_2 layer was then coated over the FTO substrates using a spin coater at 3500 rpm for 40 s. The substrates were annealed on the hotplate at 500 °C for 1 hour. After the cooling of the planar TiO_2 substrates, they were submerged in deionized water and the bath was heated to 70 °C with a magnetic stirring bead.

Titanium chloride ($TiCl_4$) was added to this solution (135 µL per 20 mL DI water) and kept for 30 min for the formation of a compact TiO_2 layer. Substrates were then brought out of the bath, washed with copious amount of DI water, and then heated on the hotplate for 1hr at 500 °C to complete the TiO_2 ETL preparation. After cooling, the substrates are transferred to an argon-filled glovebox for further depositions

2.2.3 Perovskite layer formation

Perovskite solution was prepared inside the glovebox by mixing the precursors $PbAc_2$ and methylammonium iodide (MAI) in an optimized ratio of 1:3.2 in DMF solvent. For optimum perovskite grain sizes (without cracks), 405 mg of $PbAc_2$ was mixed with 545 mg of CH_3NH_3I in 1mL of dimethylformamide (DMF) and stirred for 2 hours before deposition. The solution was dropped on top of TiO_2 substrates and spin coated 3500 rpm for 40 s with ramp speed of 1500 rpm/s. For antisolvent treatment, the spin coating is done at 2 speeds whereby the initial speed was the same as before but duration reduced to 30 s and then the rotation speed increased to 5000 rpm. At that speed, 100µL of chlorobenzene is swiftly dropped over the rotating substrates and kept running for 10 more seconds. It is observed that the surface of the substrate immediately turned brownishly as the solvent dries during spin whereas when the antisolvent is not used, a transparent yellowish film is obtained. The films were kept aside for 2 hours before annealing at 100 °C for 15 minutes to complete the conversion to the perovskite and obtain the dark brown films.

2.2.4 Hole transport layer (HTL) optimization

Spiro-OMeTAD solution is prepared by dissolving 65 mg of Spiro-OMeTAD in 1 mL of chlorobenzene. Additives are added with 70 µL of LiTFSI solution (170 mg/mL in acetonitrile) and 20 µL of 4-tert butyl pyridine in the same Spiro-OMeTAD solution and stirring for 2 hours.[36] P3HT solution is prepared by dissolving 20 mg of P3HT in 1 mL of chlorobenzene. The blend solutions are prepared by adding a measured weight proportion of P3HT in stock Spiro-OMeTAD solution. Before film deposition, these blends are preheated at 50 °C for 1 hour. To obtain smooth films the solutions for all HTLs were dropped over rotating perovskite films at 4000 rpm and kept for 30 s. The films were then kept under dark ambient conditions for 12 hours before moving on to the electrode deposition. To complete the electrode formation, 30 nm of gold followed by

120 nm of silver is deposited on top of the films through a mask using a thermal evaporator at a base pressure of 1 x 10^{-6} Torr. Effective area of the pixel is $9 mm^2$ as dictated by the mask.

2.2.5 Materials Characterization Techniques

Surface electron microscope (SEM) images of the perovskite and HTL layers were obtained using FEI Nano SEM 450. X-ray Diffraction profiles were recorded on an X'pert Pro model PANalytical diffractometer from Philips PANalytical instruments which were operated at a voltage of 40 kV and a current of 30 mA with Cu Kα (1.5418 Å) radiation. The perovskite samples were scanned in a 2θ range from 10° to 50° with 4 scan rate of 0.4° per minute.

2.2.6 Device Characterization Techniques

2.2.6.1 Current (J) – voltage (V) measurement

Current –voltage measurement was carried out with a keithley 2634B source-meter under argon filled glovebox. The illumination intensity approximating 1 sun illumination (AM 1.5) was provided using solar simulator from Peccell technologies (PEC-L01). A shadow mask was used before the device limiting the amount of light reaching the pixel of device and matching it closely to pixel size. The light intensity was set 100 mW/cm^2 at the pixel using a Thorlab thermal sensor S302C (aperture size 9.3 mm).

2.2.6.2 Capacitance-Voltage and Impedance measurement:

PSM1735 (N4L) LCR meter was used to measure the Capacitance–Voltage and frequency response of the devices. C-V measurements were carried out at a frequency of 1 kHz. Impedance measurements were acquired in between 100 Hz to 1 MHz frequency range. AC perturbation voltage used in these studies was 50 mV.

2.3 Results and Discussions

2.3.1 SEM analysis of perovskite layer

Pinhole and crack-free perovskite layer formation is indispensable for achieving compact and consistent films to better charge transport in submicron thick solution-processed perovskite solar cells. Using $PbAc_2$ as a precursor we take the 3 molar volumes of MAI to maintain the stoichiometry. However, a little excess of iodide is known to render better films and thus a ratio of 1:3.2 $PbAc_2$:CH_3NH_3I is taken to that end. Keeping the ratio constant, the molar concentrations of the precursors were optimized in conjunction with the antisolvent treatment to obtain smooth films with larger crystallite sizes. As the concentration is increased in the precursor solution, we obtained perovskite crystals with larger grain boundaries but increasing the concentration above 1000 mg/mL resulted in visible cracks in the film whereby it was decided that 950 mg/mL in single solvent DMF serves the purpose best.

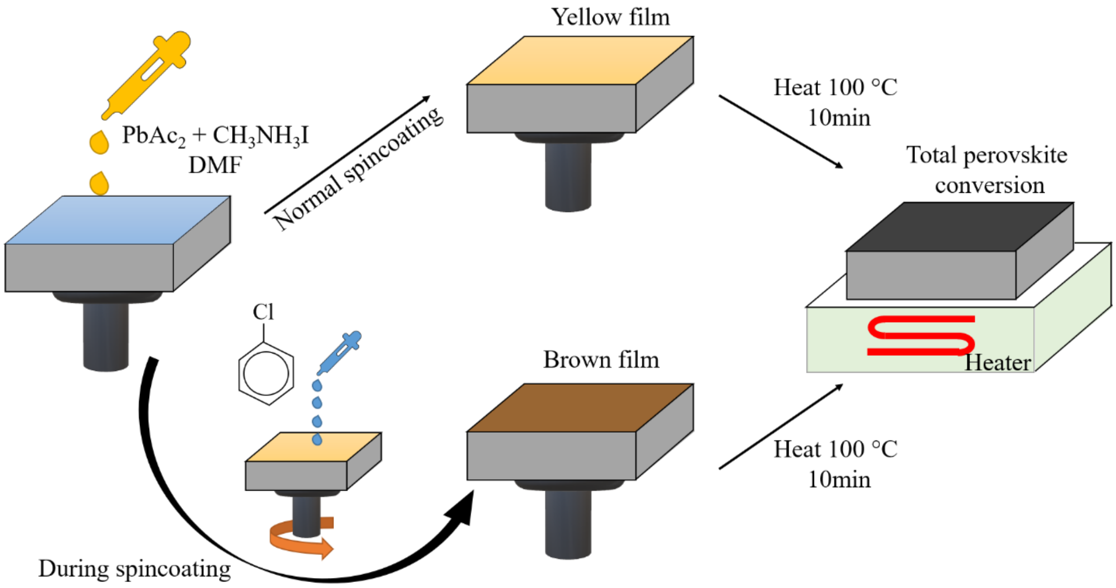

Figure 2.1: Representation of perovskite film formation with and without antisolvent treatment.

Antisolvent treatment on films made by taking PbI_2 as a precursor in single step deposition has yielded better results previously.[4] Traditionally both polar and non-polar solvents have been utilized for the purpose of antisolvent treatment, though the latter are favoured due to their reduced interaction with polar DMF solvent during crystallization. Toluene and chlorobenzene are two commonly used antisolvents and we chose chlorobenzene as we expect a slight amount of chlorine doping happening to perovskite which might be beneficial in obtaining higher performance. Figure 2.1 illustrates how antisolvent is utilized during the spin coating process to speed up the perovskite formation by removing the excess non-volatile solvent (DMF here). The antisolvent treatment for the 950 mg/mL film, as shown in Figure 2.2, shows a marked improvement in the quality of the perovskite film. In Figure 2.2(a), we see an untreated film that has crystallite sizes ranging from a minimum of 400 nm to around 1um at highest. Average size is around 800 nm and the pinholes are easily discernible at that magnification. A similar film, when subjected to antisolvent treatment using chlorobenzene, leads to larger crystallites that are fused effectually, thus eliminating the pinholes in the film studied at the same magnification as before. The average size of the perovskite crystals increases beyond 1 µm as shown in Figure 2.2(b).

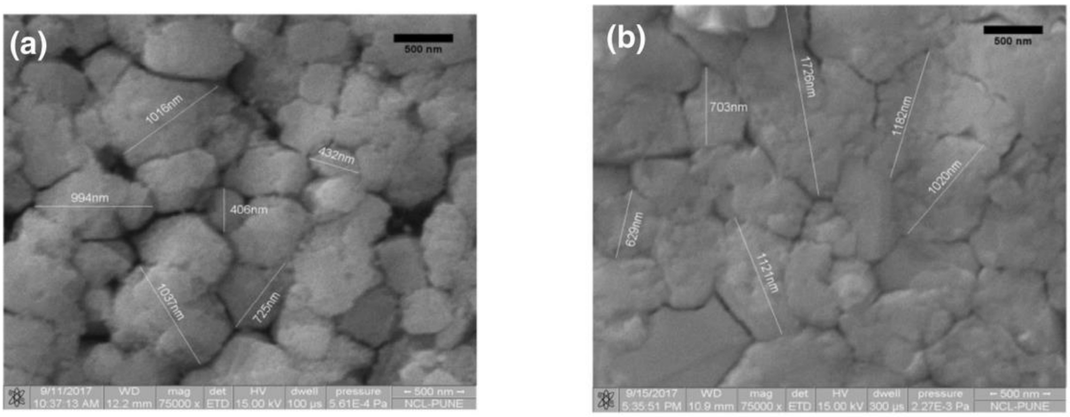

Figure 2.2: Effect of antisolvent treatment on the perovskite film prepared from 950mg/mL concentration. (a) untreated film and (b) antisolvent treated film. Scale bar 500nm.

2.3.2 XRD characteristics of Perovskite

The findings from SEM are corroborated from the XRD of the untreated and antisolvent treated perovskite films shown in Figure 2.3. XRD confirms the presence of the tetragonal phase of the $MAPbI_3$ perovskite crystals in both instances with lattice parameters a=b=2.85 Å and c= 12.64 Å. From the untreated sample, the peak at 14.2° indicates the principal growth direction of the perovskite in (110) plane which is the long axis parallel to the substrate.[37,38] Other prominent peaks are the second reflection form (220) plane at 28.4°, (112) plane, and its second reflection (224) at 20.0° and 40.6° respectively.

When the layer is treated with antisolvent, it is observed that the intensity of (110) and (220) planes rises by a factor > 2 whereas intensity corresponding to (112) and (224) planes remains practically similar. This implies the oriented growth of the perovskite crystals due to the treatment towards the (110) plane (which is parallel to the substrate) and leads to larger crystallite size and pinhole-free films, as evidenced by the FESEM images in Figure 2.2. These factors combined are expected to facilitate the carrier transport helping to boost the efficiency and reproducibility of solar cells.

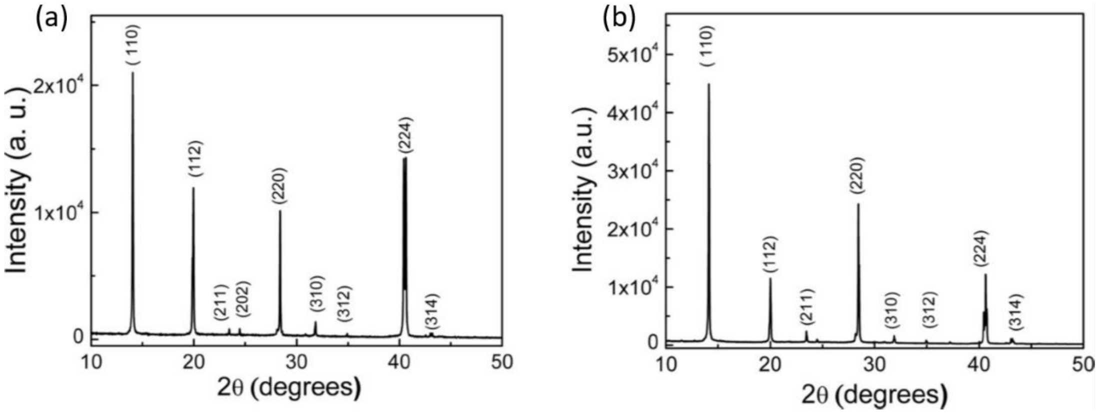

Figure 2.3: X-ray diffraction pattern of Perovskite films (a) without antisolvent treatment and (b) with antisolvent treatment. The respective planes are marked inside the figure.

2.3.3 SEM analysis of HTL

With all the improvements done to the perovskite layer, the performance of the solar cells is still limited due to the fallibilities associated with the Spiro-OMeTAD used as HTL. The films obtained with the HTL were inconsistent (the agglomeration at the top is visible even with the naked eye) and also prone to degradation under continuous electrical stress even when measured inside the Argon atmosphere.

To probe this, a high-resolution SEM study was done on the top HTL which, as seen in Figure 2.4(a), indicates the presence of large cracks in the film. These cracks are detrimental to the solar cell performance as the gold atoms vacuum deposited at the top seeps in through them and forms direct contact with the bottom perovskite layer. These filaments then provide a less resistive path for the flow of charge carriers and enhance the recombination or injection. The amount of current passing through such a small area can lead to the 'burning' of the perovskite layer and subsequent death of pixel.[25] Thus reproducibility, stability, and performance of the solar cells are affected by this electrode seepage in the case of Spiro-OMeTAD. Conducting polymer, P3HT, when used as HTL on top of perovskite, has been reported to give reasonably good efficiency but succeeds far more in stability owing to its polymeric nature helping it to form compact and pinhole-free films.[27] Herein, we attempt to improve the quality of our Spiro-OMeTAD HTL layer by blending it with P3HT in situ. P3HT is chosen in this study due to its favourable HOMO-LUMO positions in regards with perovskite and common non-polar solvent for dissolution to protect the bottom layer.

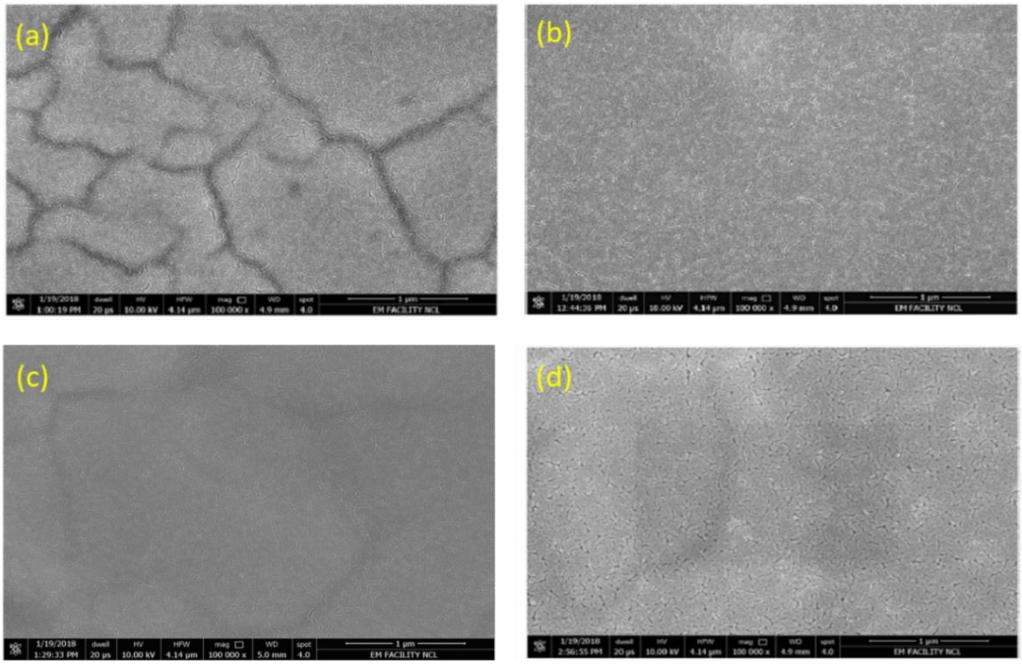

Figure 2.4: FESEM images of HTLs on top of active layer. Only (a) Spiro-OMeTAD, (b) P3HT layers. Blended HTLs in ratio (c) 1:6 and (d) 1:3 P3HT: Spiro-OMeTAD.

In order for the blend to act efficiently as HTL, we expect it to possess the following qualities: (1) a compact smooth layer on top of the perovskite layer, (2) The HOMO level matching should allow efficient transfer of holes from the perovskite layer to the HTL and (3) hole mobility of the blend layer should be considerable enough for efficient transportation of all the carriers through its thickness to the top electrode. As seen in the SEM image, the P3HT layer shows a very compact film devoid of any pinholes or cracks (Figure 2.4b). As the blend film is formed for the ratio 1:6 P3HT: Spiro-OMeTAD in Figure 2.4c we see a reduction in cracks compared to only Spiro-OMeTAD and for the ratio 1:3 we see a completely smooth film with good surface coverage closer to the P3HT only film (Figure 2.4d). These attributes prompt us to construct solar cells with blended HTL on top of the perovskite layer.

2.3.4 J-V characteristics

To elucidate the improvement in charge transport and carrier extraction with the help of improved morphology of films, solar cell devices were constructed with the architecture as shown in the cross-section image of a representative device (Figure 2.6a). Inset shows various layers with TiO_2 as ETL, followed by antisolvent treated perovskite film and top HTL deposited with a varied weight proportion of P3HT in Spiro-OMeTAD.

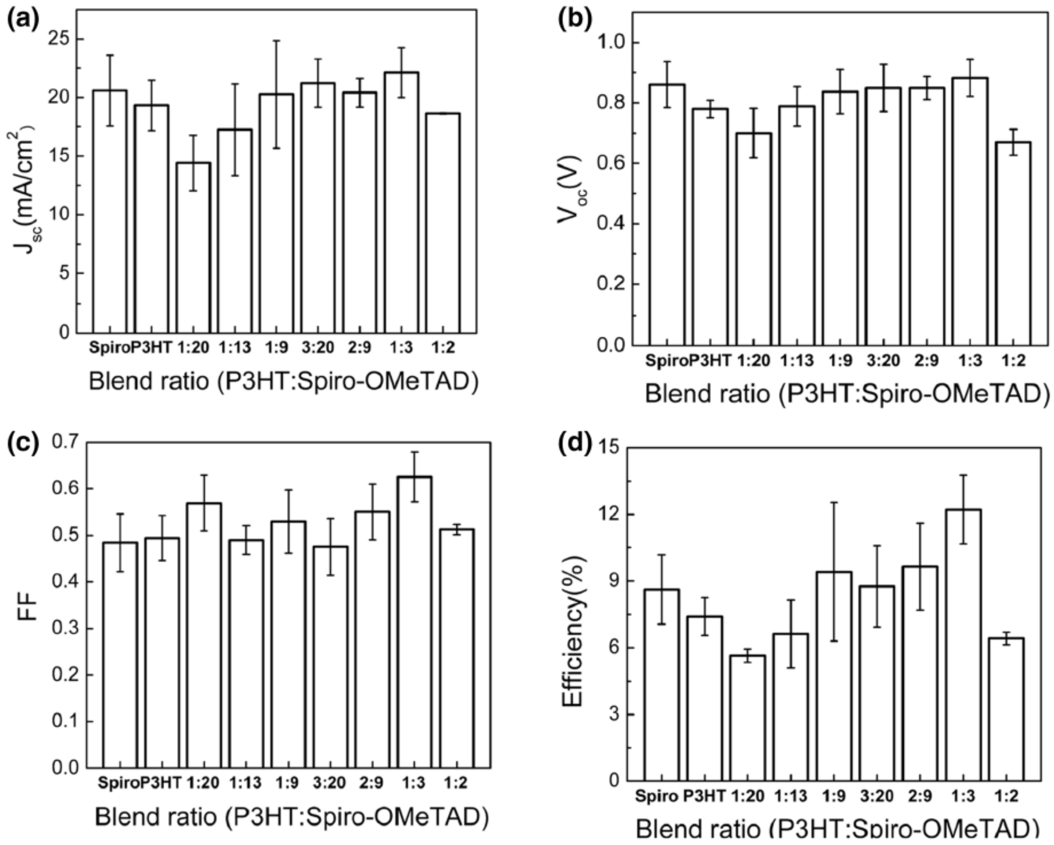

Figure 2.5: Photovoltaic figure of merits. Dependence of J_{SC}, V_{OC}, FF, and PCE with varied blend ratios of P3HT: Spiro-OMeTAD are shown in a, b, c and d respectively. The standard deviation in the parameters is shown by the error bar.

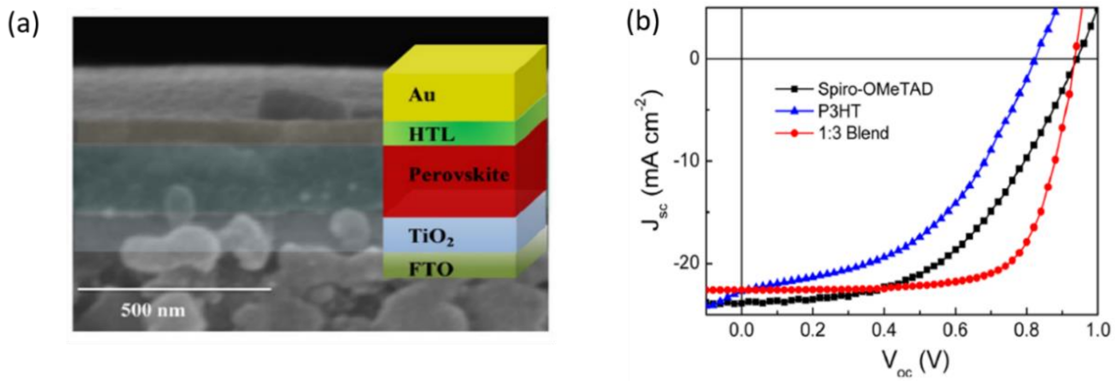

Figure 2.6: (a) shows the cross-sectional image along with the representative layers in the inset and (b) J-V curve for solar cells constructed with different HTLs – Spiro-OMeTAD, P3HT, and 1:3 blend of P3HT: Spiro-OMeTAD.

Chapter 2: Improved performance and reproducibility of perovskite solar cells by jointly tuning the hole transport layer and the perovskite layer deposition

In this chapter, the focus was to find a balanced ratio between the two materials, namely Spiro-OMeTAD and P3HT. Different photovoltaic parameters, namely J_{SC}, V_{OC}, FF, and PCE for the varied blend ratios are shown in Figure 2.5(a)–(d), respectively. The standard deviation in photovoltaic parameters for different batches is reflected by the error bar. From the J_{SC} distribution, we see that high current is obtained for most of the blend ratios (though with high deviation in many cases) barring the terminal blend ratios (1:20) and (1:2). The highest average V_{OC} is seen in the case of Spiro-OMeTAD and the 1:3 blend (P3HT:Spiro-OMeTAD) devices with the latter being more consistent and stable. Combinedly, most consistent and high photovoltaic performances are achieved for the blend ratios 2:9 and 1:3. However, 1:3 blend produces higher FF repetitively to yield the highest average PCE among the lot. The J-V characteristics of the best performing solar cells under solar illumination based on Spiro-OMeTAD, P3HT, and 1:3 blend HTLs are shown in Figure 2.6(b). The highest performance in the case of Spiro-OMeTAD is obtained to be 11.23% in which the performance is limited by the moderate FF (0.5) probably originating from the subpar layer formation. In the case of P3HT, 8.85% PCE is obtained with the dismal performance in V_{OC} (0.8 V) and FF (0.49). In contrast, the performance of the 1:3 blend-based device is superior (PCE = 14.87%) due to improvement in V_{OC} (0.94 V) and FF (0.70). All the solar cell devices show hysteresis in their J–V characteristics. The photovoltaic parameters for reverse and forward voltage scans are tabulated in Table 2.1. The P3HT and the 1:3 blend HTL based solar cell shows relatively less hysteresis compared to Spiro-OMeTAD based solar cells.

Table 2.1 Photovoltaic parameters of the best performing solar cells

HTL	Scan Direction	V_{OC} (V)	J_{SC} (mA/cm^2)	FF (%)	PCE (%)
Spiro-OMeTAD	Reverse	0.94	23.9	0.50	11.23
	Forward	0.9	24	0.33	7.13
P3HT	Reverse	0.8	22.6	0.49	8.85
	Forward	0.72	21.8	0.50	7.85
1:3 Blend	Reverse	0.94	22.6	0.70	14.87
	Forward	0.9	22.9	0.63	12.99

2.3.5 Electronic Impedance Spectroscopy measurements

To determine the factors affecting the performance of the solar cells as shown in Figure 2.6b and Table 2.1, electronic impedance spectroscopy is performed. From the Nyquist plot (Z_{real} vs. Z_{img}) of the photovoltaic devices based on Spiro-OMeTAD, P3HT, and 1:3 blend as HTL (Figure 2.7(a), (c), (e) respectively), series resistance, recombination resistance, and carrier recombination lifetimes are determined. The Nyquist plot for Spiro-OMeTAD clearly shows two semicircular arcs appearing at separate applied frequency regimes, whereas P3HT and 1:3 blend-based solar cells show a single arc for the entire frequency range of 100 Hz – 1 MHz range. The equivalent circuit model requires a minimum of two parallel R–C combinations in order to contemplate the Nyquist plot for Spiro-OMeTAD based solar cells (Figure 2.6(b)), whereas one R–C combination is sufficient to simulate the Nyquist plots obtained for P3HT and 1:3 blend based solar cells (Figure 2.6(d)). In the case of Spiro-OMeTAD HTL, two R–C combinations may originate from two interfaces - perovskite/Spiro-OMeTAD and perovskite/metal. We suspect the pinholes in the Spiro-OMeTAD HTL allow the direct contact of the metal electrode with the perovskite layer which in turn facilitates the alternate transport path for the charge carrier to bypass the Spiro-OMeTAD layer and makes the perovskite/Spiro-OMeTAD junction leaky.

Due to the high conductivity of the metals, the R–C arc of perovskite/metal contact should appear at a higher frequency regime. Therefore, we attribute the low-frequency arc to leaky perovskite/Spiro-OMeTAD junction and the high-frequency arc to perovskite/metal junction. In the case of P3HT and 1:3 blend HTL based solar cells appearance of one arc in the Nyquist plot implies good junction properties between perovskite and the HTLs.

Series and recombination resistance of the solar cells are determined from Z_{real}–Z_{img} plots using the following approximation, at low frequency (100 Hz), Z_{real} = series resistance + recombination resistance, and at frequency 1 MHz, Z_{real} = series resistance. Series resistance is found to be 30 ± 2 Ω for all the devices (Figure 2.8(a)), suggesting no apparent variation in series resistance for different blend layers. This is consistent with the fact that major contribution in series resistance arises from the space charge region of the junctions, not from the quasi-neutral region of individual layers. The recombination resistance accounts for much deeper insight into the recombination process of the solar cells. Higher recombination resistance reduces photo carrier recombination and improves FF and current for the solar cells.

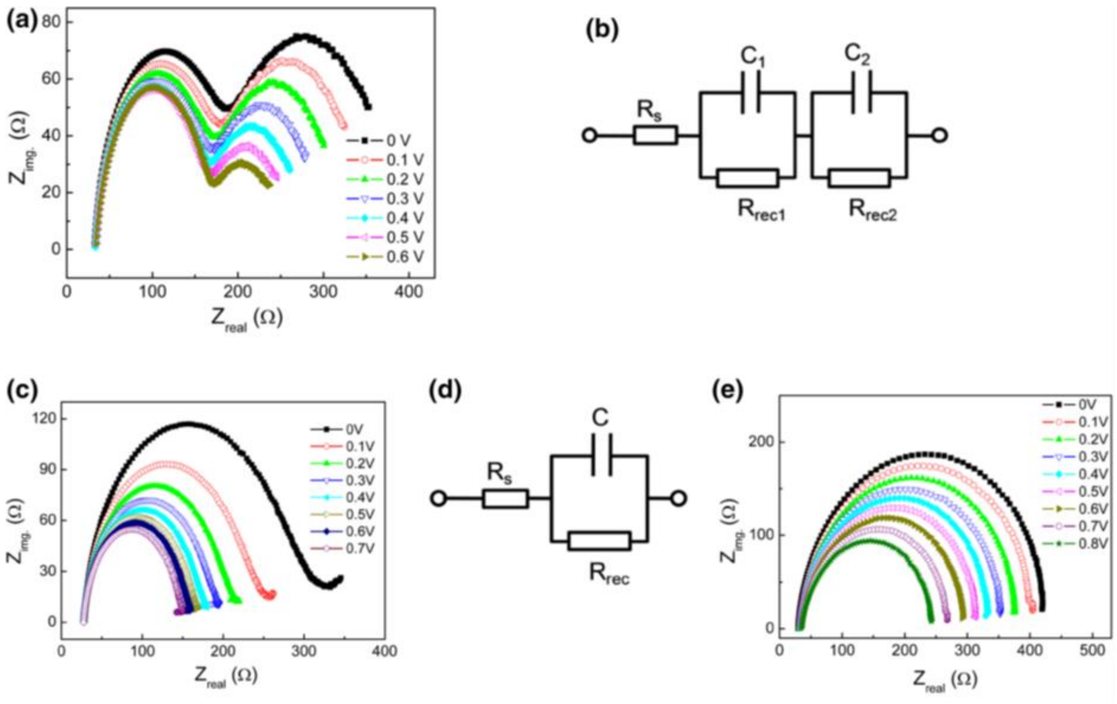

Figure 2.7: Impedance spectroscopy of the solar cells for different HTLs. a and b show the Nyquist plot (Z_{real}–Z_{img}) and the corresponding equivalent circuit for Spiro-OMeTAD. The Nyquist plots for P3HT and 1:3 blend is shown in c and e respectively and their common equivalent circuit is shown in d.

The recombination resistances are determined and compared for different HTLs (Figure 2.8(b)) under solar illumination for varied applied bias between 0 V and V_{OC}. The recombination resistances for 1:3 blend layer are higher than P3HT and Spiro-OMeTAD at any given applied bias. In the case of P3HT as HTL the recombination resistance shows abrupt decay with the increase in bias, suggesting the lack of diffusion transport and dominance of drift transport of photo carriers in the P3HT layer, which may originate from low carrier mobility of the P3HT film. This property is reflected in the low FF of the P3HT-based solar cells. In the case of Spiro-OMeTAD, the leak in the perovskite/ Spiro-OMeTAD junction reduces the effective recombination resistance which comes in between P3HT and blend.

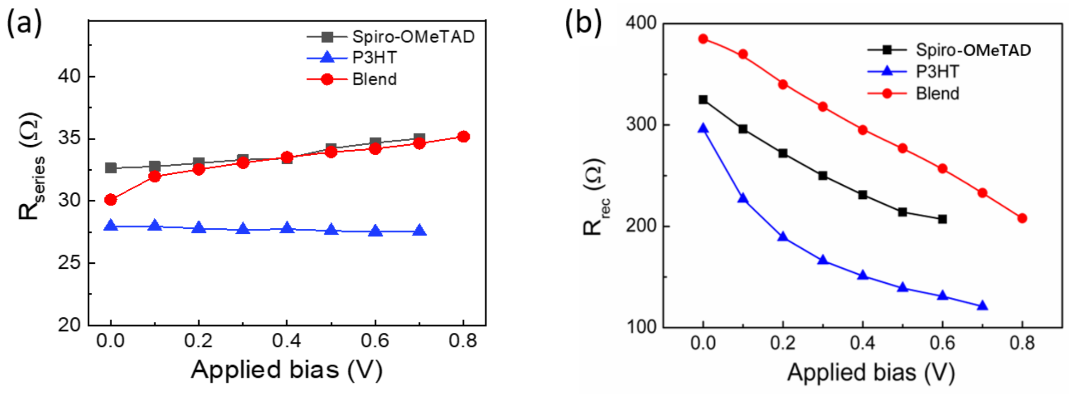

Figure 2.8: (a) Series resistance and (b) Recombination resistance with different applied voltage bias.

Photo carrier recombination lifetime in the photovoltaic devices is determined from the Nyquist plots by obtaining the frequency (f) at which Z_{img} is maximum, also denoted as characteristic frequency ($\omega_0 = 2\pi f$).[39] Under 1.5 A.M. illumination recombination lifetimes ($\tau = 1/\omega_0$) for different HTLs are plotted against applied bias as shown in Figure 2.9. The carrier lifetime for the blend HTL shows very little dependence with the applied bias which could be responsible for the high FF (0.70) in their solar cell characteristics. In comparison to blending both P3HT and Spiro-OMeTAD based devices shows a steady decay in their carrier lifetime with the increase in applied bias which is reflected in the shape of their J–V characteristics. Spiro-OMETAD based solar cell shows the lowest carrier lifetime values, this could be due to fast recombination of electron and hole at the perovskite-metal interface.

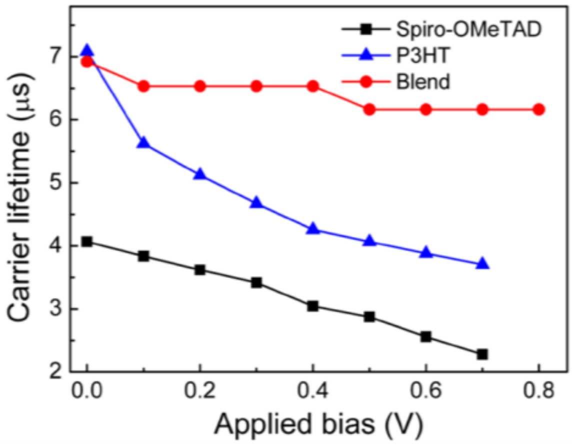

Figure 2.9: Carrier lifetime for different HTL based perovskite solar cell at varied voltage bias.

2.3.8 Hole Mobility measurements of the HTLs

The charge transport properties of the blend layer should depend on the formation of a continuous charge transport network through individual components i.e., Spiro-OMeTAD and P3HT. In the case of organic semiconductors, charge transport is dominated by hopping transport from one site to another. In the absence of a continuous charge transport network in the blend layer, hole transport would be hindered by the HOMO level energy mismatch between adjacent sites, which would result in the decrease in hole mobility and increase in potential drop across the HTL in solar cells. We sought to investigate the hole mobility for different HTLs used in this study. Hole mobility is determined by space charge limited conduction mechanism (SCLC) using ITO–HTL–Au device configuration. ITO and Au are chosen as electrodes to establish ohmic contact for the hole with the HTLs and to ensure that at a given applied bias only hole injection to the HTLs is possible. At the high injection region current inside the HTLs would be controlled by the accumulation of holes inside the bulk of the HTLs and can be explained by Mott Gurney law in space charge region i.e., J = $\frac{9\varepsilon\varepsilon_0\mu}{8L^3}V^2$, where J is the current density, V_a is the applied bias, L is the HTL layer thickness, μ is the mobility, ε is the permittivity of air and ε_0 is the relative dielectric constant of HTLs which is considered as 3.5 in this study. The J–V characteristics for different HTLs are shown in Figure 2.10. The corresponding hole mobilities determined for different HTLs are shown in Table 2.2.

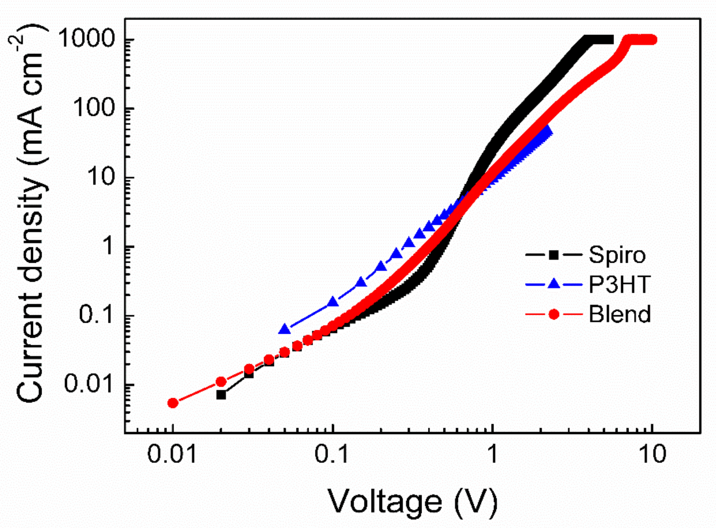

Figure 2.10: Current density versus voltage plot in log–log scale for the hole only metal-semiconductor-metal devices is shown.

As can be seen that the hole mobility for the P3HT is lowest, intermediate for the blend, and highest for the Spiro-OMeTAD. From the observation, we infer that the charge transport inside the blend layer is dominated by the Spiro-OMeTAD and the small reduction in blend mobility in comparison to pristine Spiro-OMeTAD could be due to the reduction in effective area and a possible increase in path length through the higher conducting Spiro-OMeTAD channel inside the blend layer. The magnitude of the hole mobility further emphasizes that the charge transport network through the Spiro-OMeTAD network is not breached for the optimum blend ratio which is critical for high solar cell performances.

Table 2.2. Hole mobility for different HTLs from SCLC method

Name of the HTL	Hole mobility ($cm^2V^{-1}s^{-1}$)
Spiro-OMeTAD	2.15×10^{-3}
P3HT	1.67×10^{-3}
1:3 Blend	2.01×10^{-3}

2.4 Conclusion

In this chapter, we have shown that the use of anti-solvent and optimal precursor concentration allows to form consistent, pinhole-free, compact, and large crystallite size perovskite film using $PbAc_2$ as the lead precursor. The pinholes and cracks of the Spiro-OMeTAD HTL layer are effectively removed by blending Spiro-OMeTAD with the polymer P3HT. From a series of blend ratios, the optimum ratio is identified to be 1:3 P3HT:Spiro-OMeTAD to yield the highest PCE of 14.87% in $CH_3NH_3PbI_3$ perovskite solar cells. In optimum blend layer, high hole mobility from Spiro-OMeTAD and compact film morphology from the P3HT polymer is duly obtained to improve the performance and consistency of the perovskite solar cell. The developed strategy to form compact and pinhole-free HTL by blending Spiro-OMeTAD and P3HT could further be implemented to develop high-performance solar cells using low band gap complex perovskite materials.

2.5 References

(1) Stranks, S. D.; Snaith, H. J. Metal-Halide Perovskites for Photovoltaic and Light-Emitting Devices. *Nat. Nanotechnol.* **2015**, *10*, 391.

(2) Tsai, H.; Nie, W.; Blancon, J. C.; Stoumpos, C. C.; Asadpour, R.; Harutyunyan, B.; Neukirch, A. J.; Verduzco, R.; Crochet, J. J.; Tretiak, S.; Pedesseau, L.; Even, J.; Alam, M. A.; Gupta, G.; Lou, J.; Ajayan, P. M.; Bedzyk, M. J.; Kanatzidis, M. G.; Mohite, A. D. High-Efficiency Two-Dimensional Ruddlesden-Popper Perovskite Solar Cells. *Nature* **2016**, *536* (7616), 312–317.

(3) Chen, W.; Wu, Y.; Yue, Y.; Liu, J.; Zhang, W.; Yang, X.; Chen, H.; Bi, E.; Ashraful, I.; Grätzel, M.; Han, L. Efficient and Stable Large-Area Perovskite Solar Cells with Inorganic Charge Extraction Layers. *Science* **2015**, *350* (6263), 944–948.

(4) Jeon, N. J.; Noh, J. H.; Kim, Y. C.; Yang, W. S.; Ryu, S.; Seok, S. Il. Solvent Engineering for High-Performance Inorganic-Organic Hybrid Perovskite Solar Cells. *Nat. Mater*. **2014**, *13* (9), 897–903.

(5) Stoumpos, C. C.; Malliakas, C. D.; Kanatzidis, M. G. Semiconducting Tin and Lead Iodide Perovskites with Organic Cations: Phase Transitions, High Mobilities, and near-Infrared Photoluminescent Properties. *Inorg. Chem.* **2013**, *52* (15), 9019–9038.

(6) Alcocer, M. J. P.; Leijtens, T.; Herz, L. M.; Petrozza, A.; Snaith, H. J. Electron-Hole Diffusion Lengths Exceeding Trihalide Perovskite Absorber. *Science* **2013**, *342* (6156), 341–344.

(7) Xing, G.; Mathews, N.; Lim, S. S.; Lam, Y. M.; Mhaisalkar, S.; Sum, T. C. Long-Range Balanced Electron- and Hole-Transport Lengths in Organic-Inorganic $CH_3NH_3PbI_3$. **2013**, *342* (6156), 344-347.

(8) Jiang, F.; Rong, Y.; Liu, H.; Liu, T.; Mao, L.; Meng, W.; Qin, F.; Jiang, Y.; Luo, B.; Xiong, S.; Tong, J.; Liu, Y.; Li, Z.; Han, H.; Zhou, Y. Synergistic Effect of PbI_2 Passivation and Chlorine Inclusion Yielding High Open-Circuit Voltage Exceeding 1.15 V in Both Mesoscopic and Inverted Planar $CH_3NH_3PbI_3$(Cl)-Based Perovskite Solar Cells. *Adv. Funct. Mater.* **2016**, *26* (44), 8119–8127.

(9) Yang, W.; Yao, Y.; Wu, C. Q. Origin of the High Open Circuit Voltage in Planar Heterojunction Perovskite Solar Cells: Role of the Reduced Bimolecular Recombination. *J. Appl. Phys.* **2015**, *117* (9).

(10) Yang, W. S.; Park, B. W.; Jung, E. H.; Jeon, N. J.; Kim, Y. C.; Lee, D. U.; Shin, S. S.; Seo, J.; Kim, E. K.; Noh, J. H.; Seok, S. Il. Iodide Management in Formamidinium-Lead-Halide-Based Perovskite Layers for Efficient Solar Cells. *Science* **2017**, *356* (6345), 1376–1379.

(11) Burschka, J.; Pellet, N.; Moon, S. J.; Humphry-Baker, R.; Gao, P.; Nazeeruddin, M. K.; Grätzel, M. Sequential Deposition as a Route to High-Performance Perovskite-Sensitized Solar Cells. *Nature* **2013**, *499* (7458), 316–319.

(12) Miyasaka, T.; Kojima, A.; Teshima, K.; Shirai, Y. Organometal Halide Perovskites as Visible-Light Sensitizers for Photovoltaic Cells. *J. Am. Chem. Soc.* **2009**, *131* (17), 6050–6051.

(13) Lee, M. M.; Teuscher, J.; Miyasaka, T.; Murakami, T. N.; Snaith, H. J. Efficient Hybrid Solar Cells Based on Meso-Superstructured Organometal Halide Perovskites. *Science* **2012**, *338* (6107), 643–647.

(14) Zhao, Y.; Zhu, K. Organic–Inorganic Hybrid Lead Halide Perovskites for Optoelectronic and Electronic Applications. *Chem. Soc. Rev.* **2016**, *45* (3), 655–689.

(15) Zhang, W.; Saliba, M.; Moore, D. T.; Pathak, S. K.; Hörantner, M. T.; Stergiopoulos, T.; Stranks, S. D.; Eperon, G. E.; Alexander-Webber, J. A.; Abate, A.; Sadhanala, A.; Yao, S.; Chen, Y.; Friend, R. H.; Estroff, L. A.; Wiesner, U.; Snaith, H. J. Ultrasmooth Organic-Inorganic Perovskite Thin-Film Formation and Crystallization for Efficient Planar Heterojunction Solar Cells. *Nat. Commun.* **2015**, *6*.

(16) Kim, H. S.; Lee, C. R.; Im, J. H.; Lee, K. B.; Moehl, T.; Marchioro, A.; Moon, S. J.; Humphry-Baker, R.; Yum, J. H.; Moser, J. E.; Grätzel, M.; Park, N. G. Lead Iodide Perovskite Sensitized All-Solid-State Submicron Thin Film Mesoscopic Solar Cell with Efficiency Exceeding 9%. *Sci. Rep.* **2012**, *2*, 591.

(17) Jeon, N. J.; Noh, J. H.; Yang, W. S.; Kim, Y. C.; Ryu, S.; Seo, J.; Seok, S. Il. Compositional Engineering of Perovskite Materials for High-Performance Solar Cells. *Nature* **2015**, *517* (7535), 476–480.

(18) Zhang, Y.; Elawad, M.; Yu, Z.; Jiang, X.; Lai, J.; Sun, L. Enhanced Performance of Perovskite Solar Cells with P3HT Hole-Transporting Materials: Via Molecular p-Type Doping. *RSC Adv.* **2016**, *6* (110), 108888–108895.

(19) Qin, P.; Tanaka, S.; Ito, S.; Tetreault, N.; Manabe, K.; Nishino, H.; Nazeeruddin, M. K.; Grätzel, M. Inorganic Hole Conductor-Based Lead Halide Perovskite Solar Cells with 12.4% Conversion Efficiency. *Nat. Commun.* **2014**, *5* (1), 3834.

(20) Karuppuchamy, S.; Murugadoss, G.; Ramachandran, K.; Saxena, V.; Thangamuthu, R. Inorganic Based Hole Transport Materials for Perovskite Solar Cells. *J. Mater. Sci. Mater. Electron.* **2018**, *29* (10), 8847–8853.

(21) Chatterjee, S.; Pal, A. J. Introducing Cu_2O Thin Films as a Hole-Transport Layer in Efficient Planar Perovskite Solar Cell Structures. *J. Phys. Chem. C* **2016**, *120* (3), 1428–1437.

(22) Manders, J. R.; Tsang, S. W.; Hartel, M. J.; Lai, T. H.; Chen, S.; Amb, C. M.; Reynolds, J. R.; So, F. Solution-Processed Nickel Oxide Hole Transport Layers in High Efficiency Polymer Photovoltaic Cells. *Adv. Funct. Mater.* **2013**, *23* (23), 2993–3001.

(23) Weber, S.; Rath, T.; Mangalam, J.; Kunert, B.; Coclite, A. M.; Bauch, M.; Dimopoulos, T.; Trimmel, G. Investigation of NiO_x-Hole Transport Layers in Triple Cation Perovskite Solar Cells. *J. Mater. Sci. Mater. Electron.* **2018**, *29* (3), 1847–1855.

(24) Besleaga, C.; Abramiuc, L. E.; Stancu, V.; Tomulescu, A. G.; Sima, M.; Trinca, L.; Plugaru, N.; Pintilie, L.; Nemnes, G. A.; Iliescu, M.; Svavarsson, H. G.; Manolescu, A.; Pintilie, I. Iodine Migration and Degradation of Perovskite Solar Cells Enhanced by Metallic Electrodes. *J. Phys. Chem. Lett.* **2016**, *7* (24), 5168–5175.

(25) Domanski, K.; Correa-Baena, J. P.; Mine, N.; Nazeeruddin, M. K.; Abate, A.; Saliba, M.; Tress, W.; Hagfeldt, A.; Grätzel, M. Not All That Glitters Is Gold: Metal-

Migration-Induced Degradation in Perovskite Solar Cells. *ACS Nano* **2016**, *10* (6), 6306–6314.

(26) Holliday, S.; Ashraf, R. S.; Wadsworth, A.; Baran, D.; Yousaf, S. A.; Nielsen, C. B.; Tan, C.-H.; Dimitrov, S. D.; Shang, Z.; Gasparini, N.; Alamoudi, M.; Laquai, F.; Brabec, C. J.; Salleo, A.; Durrant, J. R.; McCulloch, I. High-Efficiency and Air-Stable P3HT-Based Polymer Solar Cells with a New Non-Fullerene Acceptor. *Nat. Commun.* **2016**, *7* (1), 11585.

(27) Zhang, M.; Yu, H.; Yun, J.-H.; Lyu, M.; Wang, Q.; Wang, L. Facile Preparation of Smooth Perovskite Films for Efficient Meso/Planar Hybrid Structured Perovskite Solar Cells. *Chem. Commun.* **2015**, *51* (49), 10038–10041.

(28) Yang, L.; Cappel, U. B.; Unger, E. L.; Karlsson, M.; Karlsson, K. M.; Gabrielsson, E.; Sun, L.; Boschloo, G.; Hagfeldt, A.; Johansson, E. M. J. Comparing Spiro-OMeTAD and P3HT Hole Conductors in Efficient Solid State Dye-Sensitized Solar Cells. *Phys. Chem. Chem. Phys.* **2012**, *14* (2), 779–789

(29) Wang, J.-F.; Zhu, L.; Zhao, B.-G.; Zhao, Y.-L.; Song, J.; Gu, X.-Q.; Qiang, Y.-H. Surface Engineering of Perovskite Films for Efficient Solar Cells. *Sci. Rep.* **2017**, *7* (1), 14478.

(30) Im, J.-H.; Kim, H.-S.; Park, N.-G. Morphology-Photovoltaic Property Correlation in Perovskite Solar Cells: One-Step versus Two-Step Deposition of $CH_3NH_3PbI_3$. *APL Mater.* **2014**, *2* (8), 81510.

(31) Nie, W.; Tsai, H.; Asadpour, R.; Blancon, J.; Neukirch, A. J.; Gupta, G.; Crochet, J. J.; Chhowalla, M.; Tretiak, S.; Alam, M. A.; Wang, H.; Mohite, A. D. High-Efficiency Solution-Processed Perovskite Solar Cells with Millimeter-Scale Grains. *Science* **2014**, *347* (6221), 522-525.

(32) Rong, Y.; Tang, Z.; Zhao, Y.; Zhong, X.; Venkatesan, S.; Graham, H.; Patton, M.; Jing, Y.; Guloy, A. M.; Yao, Y. Solvent Engineering towards Controlled Grain Growth in Perovskite Planar Heterojunction Solar Cells. *Nanoscale* **2015**, *7* (24), 10595–10599.

(33) Stranks, S. D.; Nayak, P. K.; Zhang, W.; Stergiopoulos, T.; Snaith, H. J. Formation of Thin Films of Organic-Inorganic Perovskites for High-Efficiency Solar Cells. *Angew. Chemie - Int. Ed.* **2015**, *54* (11), 3240–3248.

(34) Forgács, D.; Sessolo, M.; Bolink, H. J. Lead Acetate Precursor Based P-i-n Perovskite Solar Cells with Enhanced Reproducibility and Low Hysteresis. *J. Mater. Chem. A* **2015**, *3* (27), 14121–14125.

(35) Docampo, P.; Hanusch, F. C.; Stranks, S. D.; Döblinger, M.; Feckl, J. M.; Ehrensperger, M.; Minar, N. K.; Johnston, M. B.; Snaith, H. J.; Bein, T. Solution Deposition-Conversion for Planar Heterojunction Mixed Halide Perovskite Solar Cells. *Adv. Energy Mater.* **2014**, *4* (14), 1400355.

(36) Tan, H.; Jain, A.; Voznyy, O.; Lan, X.; de Arquer, F. P.; Fan, J. Z.; Quintero-Bermudez, R.; Yuan, M.; Zhang, B.; Zhao, Y.; Fan, F.; Li, P.; Quan, L. N.; Zhao, Y.; Lu, Z.-H.; Yang, Z.; Hoogland, S.; Sargent, E. H. Efficient and Stable Solution-Processed Planar Perovskite Solar Cells via Contact Passivation. *Science* **2017**, *355* (6326), 722–726.

(37) Docampo, P.; Hanusch, F. C.; Giesbrecht, N.; Angloher, P.; Ivanova, A.; Bein, T. Influence of the Orientation of Methylammonium Lead Iodide Perovskite Crystals on Solar Cell Performance. *APL Mater.* **2014**, *2* (8), 81508.

(38) Zhou, Q.; Jin, Z.; Li, H.; Wang, J. Enhancing Performance and Uniformity of $CH_3NH_3PbI_{3-x}Cl_x$ Perovskite Solar Cells by Air-Heated-Oven Assisted Annealing under Various Humidities. *Sci. Rep.* **2016**, *6* (1), 21257

(39) Garcia-Belmonte, G.; Munar, A.; Barea, E. M.; Bisquert, J.; Ugarte, I.; Pacios, R. Charge Carrier Mobility and Lifetime of Organic Bulk Heterojunctions Analyzed by Impedance Spectroscopy. *Org. Electron.* **2008**, *9* (5), 847–851.

Chapter 3

Reduction of trap and polydispersity in mutually passivated quantum dot solar cell

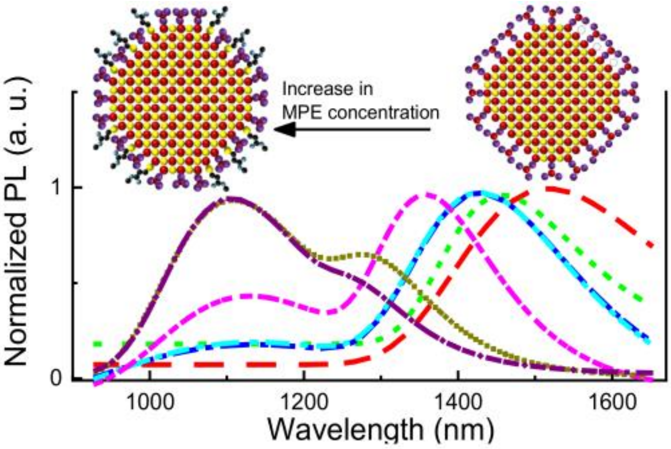

Abstract:

Control over surface passivation is a key to manage the optoelectronic properties in low dimensional nanomaterials due to their high surface to volume ratio. Tunable band gap quantum dots (QDs) are a potential building block for the development of optoelectronic devices like solar cells, photodetectors, and light-emitting diodes. Long and insulating surface ligands of colloidally synthesized QDs are exchanged by short ligands, to attain compact arrangement in thin films to facilitate the charge transport process. However, the ligand exchange process often resulted in reduced surface passivation, inhomogeneous QD fusion, and deterioration of energy bandgap, which adversely impact their performance in solar cells. Here we introduce a surface passivation strategy where the QDs are mutually passivated by organic ligand 3-methyl mercapto propionate and inorganic halometallate ligands to develop conducting QD ink. The mutually passivated quantum dots (MPQDs) show significant improvement in optoelectronic properties in maintaining the trap-free energy bandgap and size monodispersity. The photovoltaic performance of MPQDs shows a 33% average increase in power conversion efficiency (PCE) over the conventional halometallate passivation, to attain 9.6% PCE in MPQD solar cells. The improvements in photovoltaic parameters are corroborated by the reduction in density of intermediate trap states, increase in depletion width, and diffusion length in MPQD based solar cells.

Chapter 3: Reduction of trap and polydispersity in mutually passivated quantum dot solar cell

3.1 Introduction

Organic-inorganic perovskites, though being a lucrative material in solar cells, suffer from stability issues and non-utilization of near-IR radiation. To alleviate those concerns and to develop tandem solar cells with one material absorbing in the IR region, we focussed on lead sulfide (PbS) quantum dots. The Colloidal quantum dots have attracted significant research attention due to their potential applications in light-emitting diodes[1-2], photodetectors[3,4], lasers[5], and solar cell[6-8] development. The broadband tunability of energy bandgap through size control[9] has opened up innumerable possibilities of their applications in optoelectronic device development.[10] Passivation of unsaturated surface atoms through ligand engineering plays a crucial role in controlling the optical and electrical properties of QDs due to their high surface to volume ratio.[11,12] Understanding and manipulation of surface chemistry have enabled the bottom-up design of QD properties to trigger continued evolution in device efficiency. The performance of QD solar cells has been benefited from sustained development in surface passivation[8, 13] and device engineering[7, 14] to reach certified power conversion efficiency (PCE) of 12.47%.[15]

PbS QDs are at the forefront of QD solar cell research, thanks to their NIR wavelength bandgap tunability, low-temperature processibility, ambient stability, and long carrier lifetime.[16,17] As-synthesized, oleic acid capped QDs show a high degree of monodispersity and strong and narrow emission, at the cost of efficient charge transport. Replacing long and insulating oleic acid ligands by short and conducting ligands increases the conductivity of the QD films by orders of magnitudes.[18,19] However, incomplete surface passivation and reduced dot-to-dot distance in the case of short ligands lead to QD fusion and size dispersion of varying degrees in QD films.[20] Facet-dependent heterogeneity of the QD surface further adds to the odds in achieving atomic-level precision in the surface passivation by any particular ligand type.[11] For instance, PbS QDs are terminated by polar (111) facets (consists of Pb atoms) and charge-neutral (200) facets (consists of alternate Pb and S atoms).[21,22] As a result, X-type ionic ligands ($RCOO^-$, RS^- and I^-) preferably bind with the polar (111) facets terminated by unsaturated Pb atoms. The charge neural (200) surface, made of an alternate arrangement of Pb and S atoms, can be passivated by coordinating with the neutral donor (RCOOH, RSH, RNH_2 to passivate Pb sites) and neural acceptor ($Pb(RCOO)_2$ and $CdCl_2$ to passivate S sites) ligands.[11, 22] Size polydispersity can also be introduced during the course of the ligand exchange process, as observed in the case of the layer-by-layer solid-state ligand exchange process.[23] Uncontrolled ligand exchange and poor surface coverage promote QD fusion and aggregation in the case of the layer-by-layer solid-state ligand exchange process. A significant advancement in surface passivation has been made when the colloidal dispersion of QDs in solution-phase surface passivation is achieved using halometallate ligands.[24,25] Solution phase ligand exchange offered homogeneous surface passivation, which helped to reduce the QD size dispersion and intermediate trap density in QD solids.[8] Recently, hybrid passivation using halometallate and organic thiol is introduced, which shows promising results in controlling doping type and doping density to improve solar cell performances.[15, 26,27]

Organic thiol molecules have long been perused as a surface ligand to build layer-by-layer QD films for solar cell applications.[28,29] 3-mercaptopropionic acid (MPA) is the most sought-after ligand for the development of QD solar cells using the layer-by-layer approach, as it produces the highest PCE.[13,30] Unfortunately, solution-phase ligand exchange using MPA leads to aggregation and precipitation of QDs.[15] We chose to use 3-methyl mercapto propionate (MPE) (which is just the ester form of MPA) due to its similarity with MPA. FTIR study confirms no interaction of MPE ligand with butylamine solvent.

In this chapter, we highlight the development of colloidally stable QD ink, where the QD surface is simultaneously passivated by lead iodide and MPE ligands. Dual passivation of the QD surface has been achieved in a facile single-step ligand exchange process. The advantage of the developed ligand treatment process is, it allows us to tune the ratio between the ligands (lead halide and MPE) to attain maximum passivation while maintaining the colloidal disparity of the QD ink. Thus, the competition between both ligands to interact with the quantum dot turns into a symbiotic relationship where their '*mutual*' agreement to share the space leads to enhanced passivation and higher performance. We manage to retain the monodispersity and trap free energy bandgap of pristine oleic acid capped QDs in mutually passivated QDs (MPQDs), which otherwise substantially suffered in conventional lead iodide passivation. QD solar cells fabricated from MPQDs, are benefitted from low intermediated trap density, higher lifetime, and higher mobility to show a 33% increase in overall efficiency to reach 9.6% of solar cell efficiency.

3.2 Experimental Details

3.2.1 PbS QD synthesis

PbS quantum dots were prepared according to the reported method.[29] Typically, 0.45 g of lead oxide (PbO) is dissolved in 3 mL of 1-octadecene (ODE) and 1.5 mL of oleic acid (OA) mixture. The solution is then heated to 95 °C under vacuum and kept for 12 hours under continuous stirring. The reaction environment is then switched to inert argon without breaking the vacuum. The reaction mixture is then heated to 120 °C and 210 µL of hexamethyldisilithiane (TMS, in 10 mL ODE) is then swiftly injected into the reaction mixture. The heating source is switched off immediately and the reaction mixture is then allowed to cool naturally for the next 1 hour. At 35 °C, 10 mL acetone is injected into the reaction mixture and stirred for another 2 minutes. The aliquots are then centrifuges at 3500 RPM to separate the QDs. The QDs are washed again by their dispersion in 4 mL of toluene, followed by precipitation using acetone. The QDs are dried and finally dispraised in octane for the ligand exchange process.

3.2.2 Ligand exchange

230 mg lead iodide (PbI_2) and 72 mg ammonium iodide (NH_4I) are added to 5 mL of dimethylformamide (DMF) to obtain the stock solution (0.1 M) for halometallate ligands. The ligand solution is used to achieve PbI_3^- passivated PbS QDs.[43] Different concentrations of MPE are added to the halometallate ligand stock solutions to form the ligand solutions for mutual passivation. To prepare 0.45 mM, 0.9 mM, 4.5 mM, 18 mM, 36 mM and 72 mM 3-methyl mercaptopropionate (MPE) solutions, 0.27 mg, 0.54 mg, 2.70 mg, 10.80 mg, 21.60 mg and 42.00 mg respectively are added separately in each 5 mL of halometallate ligand stock solutions. In a typical ligand exchange process, 5mL of 15 mg/mL PbS-OA QDs solution in octane is added slowly to 5 mL of ligand solution in a centrifuge tube. The resulting mixture solution is vortexed vigorously for two minutes to facilitate the phase transfer of QDs from octane to the DMF phase. The clear octane solution is then discarded, and the QD solution in DMF is washed two more times using octane. The QDs are then precipitated from DMF by adding 3 mL of toluene to it. The resulting solution is centrifuged, and the supernatant is discarded. The precipitated QDs are dried under continuous vacuum for 20 minutes and finally dispersed in butylamine to obtain 200mg/mL concentration.

3.2.3 Device fabrication

ZnO nanocrystals are deposited by the spin coating method to develop the electron transport layer on top of pre-cleaned ITO substrates, following the earlier reported method.[50] Butylamine dispersion of PbS QDs is deposited on ZnO coated ITO substrates using spin coating. The rotation speed is varied between 2000 r.p.m. - 4000 r.p.m to obtain the layer thickness between 370 nm to 220 nm. The PbS QD films are transferred to an Argon-filled glovebox and annealed at 70 °C for 15 minutes. Oleic acid capped PbS QDs are taken in toluene and cleaned eight times using repeated precipitation and dispersion using methanol for the development of the hole transport layer (HTL). 0.01% 1,2-ethandithiol (EDT) in acetonitrile is used to grow two layers of PbS QD films on top of the pre-coated substrates. Typically 60 nm to 70 nm PbS-EDT layer is formed for the HTL layer. To complete the solar cell, 10nm of molybdenum oxide (MoO_3), 30 nm of gold (Au), and 100 nm of silver (Ag) are deposited using a thermal evaporation process (HHV BC-300) at a base pressure of 2×10^{-6} Torr. The active area of the solar cells is 9 mm^2, as defined by the top electrode.

3.2.5 Materials Characterization Techniques

Optical absorption measurements are carried out by a Shimadzu UV−vis−IR (UV-3600 Plus) spectrophotometer. Thin-film absorption is measured using an integrating sphere (ISR-603), attached to a Shimadzu UV-3600 Plus spectrophotometer. Steady-state photoluminescence measurements (both liquid and thin-film) are performed utilizing Spectrofluorometer FS5 (Edinburgh Instruments). Thermo Scientific K-Alpha+ spectrometer is utilized to perform the XPS studies with the chamber in ultrahigh vacuum condition (10^{-9} mbar). XPS measurements are performed with a monochromatic Al Kα X-ray source (1486.6 eV) with pass energy 50 eV for individual core levels. The XPS images are calibrated to the C1s peak at a binding energy of 284.8 eV. Deconvolution and peak fitting of the XPS peak is done by CasaXPS software. All of the measurements are carried out using an electron flood gun source for surface charge neutralization. UPS measurement is also carried out by the same instrument using He-Iα radiation of energy 21.22 eV. Cross-sectional images of the device are taken by a field emission scanning electron microscope (FESEM, NNS 450). High-resolution images of QDs are captured by a high-resolution transmitted electron microscope (HRTEM, JEOL JEM 2200FES).

3.2.6 Device Characterization Techniques

3.2.6.1 Current (J) – voltage (V) measurement

Current−voltage measurements are carried out under dark and illuminated conditions using a solar simulator (PEC-L01, Peccel) with a Keithley 2634B source meter. The solar intensity is set to 1 sun illumination (AM 1.5) using a calibrated thermal detector (ThorlabS302C).

3.2.6.2 EQE Measurement

EQE was measured by illuminating the pixel with monochromatic light of different wavelengths with the help of a monochromator (SLS-M266) and a 75 W Xenon lamp light source. The current at zero bias for different wavelengths was recorded using the Keithley source meter. The power of monochromatic lights was measured using Thorlabs detectors S120VC (300-1100 nm) and S122VC (700-1800 nm).

3.2.6.3 Capacitance-Voltage Measurement

Capacitance measurements were performed by PSM1735 (N4L) LCR meter under dark. The measurement was carried out at a frequency of 1KHz and a.c. perturbation voltage of 50 mV.

3.2.6.4 Transient Measurement

A diode laser of 658 nm (Newport LQA658- 30C), modulated through a function generator (Tektronics, AFG 3021C), is used to generate short light pulses. White light bias is applied by the solar simulator (PEC-L01), and different V_{OC} values are obtained by modulating the intensity of the white light bias. The pulse width of the laser pulse is maintained to 1 μs, and the intensity of the light pulse is adjusted to attain less than 10% perturbation of the steady-state V_{OC}. The solar cell, illuminated by both, laser pulse and white light, is connected to a digital oscilloscope (Tektronics, MDO 3104) through an output resistance to record the transient characteristics. For transient photovoltage (TPV) measurement, the output resistance is set to 1 MΩ, so that all the photogenerated carriers are forced to recombine inside the solar cell. To measure the transient photocurrent the light bias is switched off and the output resistance is set to 50 Ω so that the photo carriers generated by short light pulse come out of the solar cell and recombine at the external circuit. All the measurements were conducted inside a controlled environment with temperature of 25 ± 2 °C and 50 - 60 % relative humidity.

3.2.6.5 Mobility Measurement

To measure the mobility of the photogenerated carriers under the solar illumination we used bias-dependent transient photocurrent measurement. The device under test is kept under the constant light bias of 1.5 AM illumination (using solar simulator PEC-L01), simultaneously the device is excited by the short pulse of 1 μs (wavelength 658 nm) using Newport LQA658- 30C diode laser. The voltage across the solar cell is varied by changing the DC bias across its electrodes. The transient signal from the device is measured across a 50 Ω resistance using an oscilloscope (Tektronics, MDO 3104). Different DC bias to the solar cell is applied using the inbuild function generator of the oscilloscope. The decay of the photocurrent, generated by the short light pulse, is recorded against time for different applied biases. All the measurements were conducted inside a controlled environment with temperature of 25 ± 2 °C and 50 - 60 % relative humidity.

3.3 Results and Discussions

3.3.1 FTIR of MPA and MPE

As discussed above, the strong interaction of the carboxylic group of MPA with the amine solvent (butylamine in this case) leads to the aggregation of QDs. In figure 3.1a, (stage-1) shows the PbS QD solution in octane and ligand solutions in DMF. After the ligand exchange, 3-mercaptopropionic acid (MPA) treated QDs are precipitated whereas MPE treated QDs are dispersed in DMF solution (stage-2). Stage-3 shows the homogeneous dispersion of MPE treated QDs in butylamine (BA) whereas MPA treated QDs are precipitated in BA and hence rendered useless for spin coating. Infrared absorption spectra of BA, MPA, and MPA+BA are shown in Figure 3.1(b). The IR spectrum for MPA+BA shows possible amide formation in view of signatures arising from supposedly Amide-I at 1640 cm^{-1} (corresponding to C=O stretch) and Amide-II bands at 1573 cm^{-1} (corresponding to N-H bend) via losing the C=O stretch of MPA situated at 1715 cm^{-1}. Figure 3.1(c) shows the IR spectra of BA, MPE, and MPE+BA, indicating non-interaction of MPE with BA and the C=O stretch at 1743 cm^{-1} of MPE is unaffected in presence of BA. This prompted us to utilize MPE as the thiol ligand in this study.

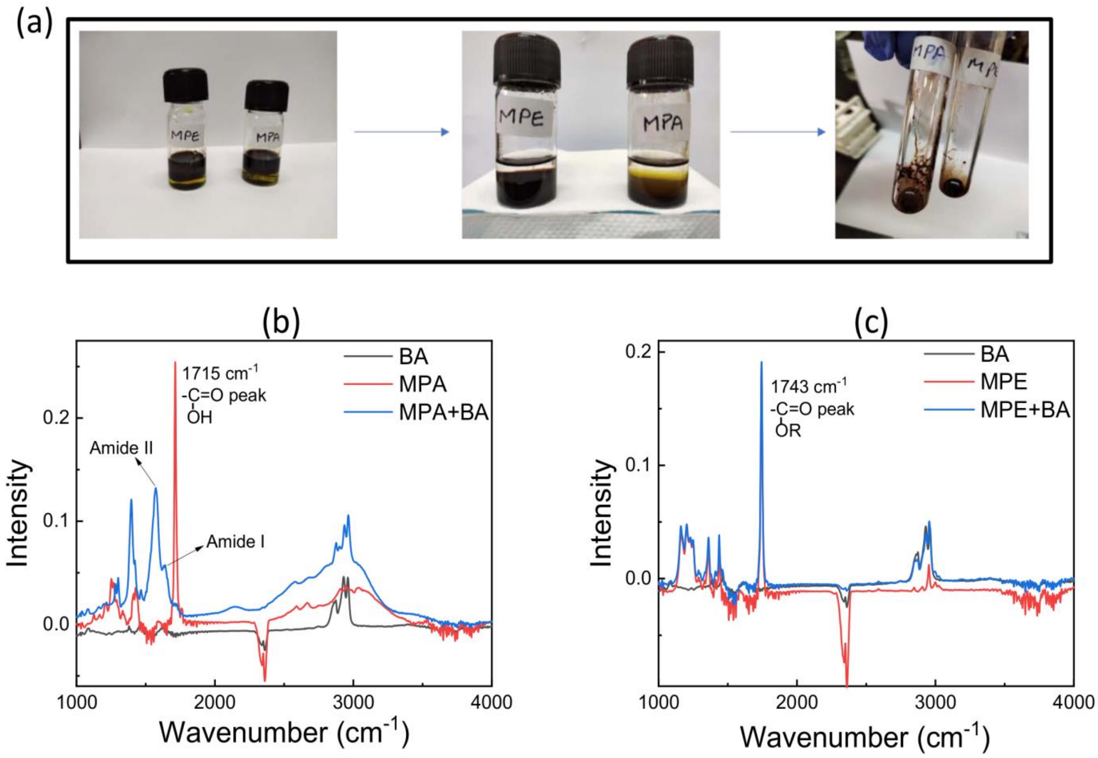

Figure 3.1: (a) Depiction of the ligand exchange process of PbS QDs using mix ligand solution containing [3-mercaptopropionic acid (MPA)+halometallate] and [3-methyl mercaptopropionate (MPE)+halometallate] ligands. Infrared absorption spectra of (b) BA, MPA, and MPA+BA and (c) BA, MPE, and MPE+BA.

3.3.2 Optical properties of PbS QDs in solution phase

As synthesized, oleic acid capped QDs show narrow size distribution and low electronic trap traps, but the long chain oleic acid molecules are deterrent for charge transport. Replacement of oleic acid molecules by small dimension ligands is critical to attaining efficient charge transport in QD solid. However, the incomplete surface coverage of the surfactants, especially in the case of small ligands, may lead to inter QD diffusion as the QDs come very close together. Additionally, the uncontrolled chemical reaction in unsaturated surface atoms leads to intermediate localized electronic states in-between the bandgap of QDs, which are detrimental for photovoltaic operation.

In the present study, oleic acid capped PbS QDs (PbS-OA) are treated with a combination of halometallate (PbI_3^-) and MPE ligands to attain mutually passivated QDs, where the MPE concentration is varied to optimize the passivation process. Schematic illustration of the QD surface in the case of pristine oleic acid passivation and mutual passivation is shown in Figure 3.2. In a typical ligand exchange process, the octane solution of oleic acid capped PbS QDs is added to the DMF solution of halometallate and

MPE ligands. Within two minutes of vigorous mixing, the QDs are phase transferred to the DMF solution, indicating successful removal of oleic acid ligands by halometallate and MPE ligands. The QD dispersion is DMF solvent is further cleaned to remove excess ligands, and taken for optical characterizations.

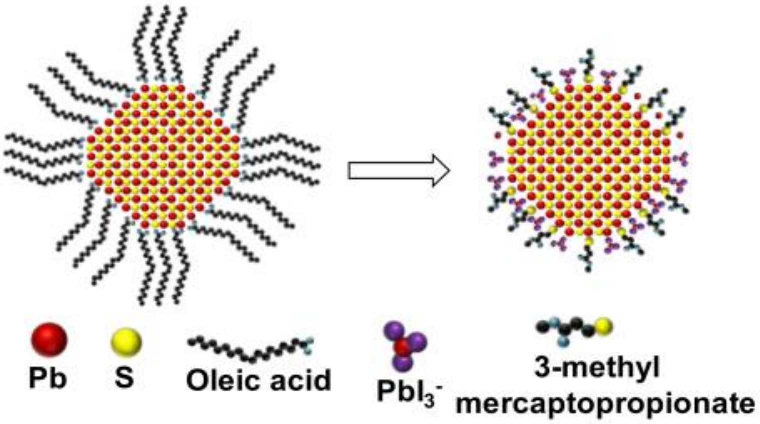

Figure 3.2: Schematic representation of oleic acid capped and mutually passivated QD surface.

The excitonic absorption peak of QD is very sensitive to a small change in their dimension[31], as the energy bandgap is inversely proportional to their size. Hence, we probe the 1st excitonic peak of PbS QDs in their DMF dispersion, as a tool to monitor the surface passivation process. The as-synthesized oleic acid capped PbS QDs show the excitonic peak at 880 nm and full width half maximum (FWHM) of 223 meV in toluene solution (Figure 3.3a and Table 3.2). Upon treatment with only PbI_3^- ligands, the excitonic peak redshifts to 896 nm, and the FWHM increases to 270 meV. While the redshift in excitonic peak implies the growth, the increase in FWHM suggests the increase in size polydispersity due to the inhomogeneous growth of PbS QDs in the case of PbI_3^- ligand passivation. For mutually passivated QDs, we treat the oleic acid capped QDs with the mixed ligands of (PbI_3^- + MPE), where the MPE concentration increases systematically for the fixed PbI_3^- (0.1 M) concentration. It is observed that as the concentration of MPE ligand is increased, the excitonic peak position shifted incrementally to longer wavelengths, but the FWHM decreases systematically. The incremental redshift in PbS QD excitonic peak due to attachment of thiol molecule is expected due to the mixing of S2p orbital of sulfur with the highest occupied states of PbS QDs.[32] The FWHM of the excitonic peak reduced steadily from 270 meV to 202 meV with the increase in MPE concentrations. This suggests that though the effective core size of QDs increases marginally due to MPE attachment, however, the increment is homogeneous for all the QDs.

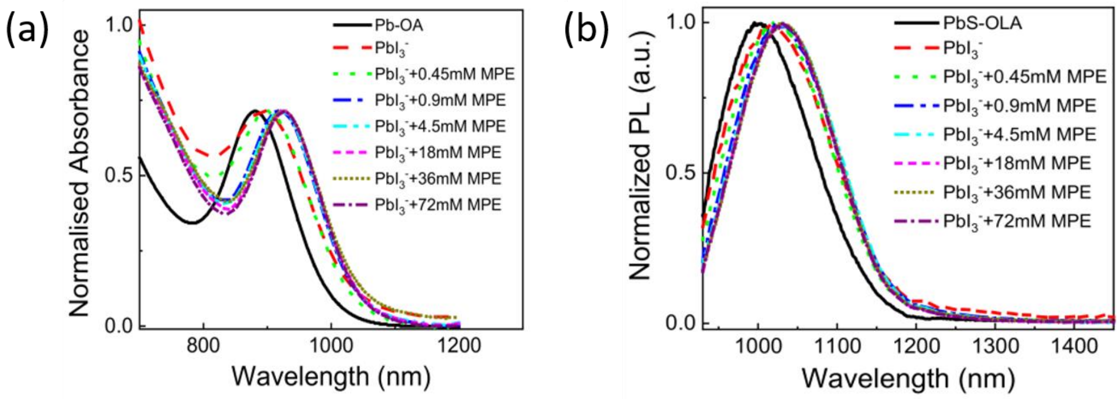

Figure 3.3: Improvement in optical properties due to mutual passivation. (a) absorbance and (b) photoluminescence (PL) of PbS QDs in DMF solution for different concentrations of MPE. The absorbance spectra are normalized for the 1st excitonic peak, and PL spectra are normalized at their emission peak for their comparison.

Further, we determined the Urbach tail energy from absorbance spectra[33], which is a direct consequence of inhomogeneous growth (Figure 3.4).[34] The Urbach energy 'E_u' is determined using the following equation

$$\ln A = lnA_0 + \frac{E - E_0}{E_u}$$

where A is the absorbance, E is the energy determined for photon energy (hν). Urbach energy E_u is determined from the inverse slope of *ln(A)* vs E plot. The Urbach energy for PbI_3^- treated QD increased to 71 meV, from 42 meV of oleic acid capped QD, which recovered fully to 38 meV in the case of MPQDs (Table 3.1). Lower Urbach energy in MPQDs indicates a narrower distribution of electronic tail states within the bandgap.

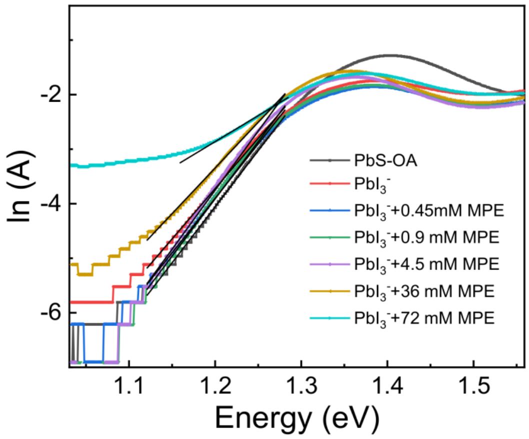

Figure 3.4: Figure shows the absorbance Vs energy in a semi-log plot. Urbach energy (E_u) is calculated from the linear fit of the absorbance onset (lower energy region of the 1st excitonic peak). Higher concentrations of MPE show lower Urbach energy, indicating less band tail states.

Table 3.1. Calculated E_u values for different concentration of MPE are shown in tabular form.

Ligand	**E_u (meV)**
OA-PbS	42.35
PbI_3^-	71.28
PbI_3^-+0.45mM MPE	44.11
PbI_3^-+0.9mM MPE	43.38
PbI_3^-+4.5mM MPE	44.84
PbI_3^-+18mM MPE	42.61
PbI_3^-+72mM MPE	37.57

We closely monitored the Stokes shift and the FWHM broadening of the photoluminescence (PL) spectrum as they are directly related to the inhomogeneous growth and sub-bandgap states of QDs. Figure 3.3b shows the normalized PL spectra of PbS QD for various surface ligands in their DMF solution. The comparative analysis of the absorbance and PL spectra of QDs in their DMF solutions is given in Table 3.2. The

PL spectra further corroborate the findings from absorption measurements. PbI_3^- treated QDs show the highest stokes shift (133 nm) and highest FWHM (187 meV) in its PL emission, following the inhomogeneous growth of QD size. In the case of MPQDs, a systematic decrease in both stokes shift and FWHM of PL emission properties are observed when the MPE concentration increases. In the case of high MPE concentrations, the Stokes shift and FWHM of emission peak reduced to 110 nm and 166 meV, respectively, which tally better than as-synthesized oleic acid capped QDs (Stokes shift 114 nm, FWHM 175 meV).

Table 3.2. Tabular representation of absorption and PL spectra of PbS QDs for different ligands in DMF solution.

Ligands	**1st excitonic peak position (nm)**	**FWHM [absorbance] (meV)**	**PL peak position (nm)**	**FWHM [PL] (meV)**	**Stokes shift (nm)**
OA-PbS	881	223	995	175	114
PbI_3^-	889	270	1022	187	133
PbI_3^-+0.45mM MPE	896	250	1025	177	129
PbI_3^-+0.9mM MPE	916	221	1032	174	116
PbI_3^-+4.5mM MPE	918	217	1035	172	117
PbI_3^-+18mM MPE	922	206	1035	166	113
PbI_3^-+36mM MPE	922	207	1035	166	113
PbI_3^-+72mM MPE	924	202	1034	166	110

Further, we monitor the relative PL emission intensity of PbS QDs for different ligand environments in their solution-phase dispersion. To determine the relative PL emission intensity of PbS QDs for different ligand passivation, absorption spectra for the respective solutions are measured first. Next, the absorption at 550nm wavelength is unified for all the samples using suitable multiplication factors (Figure 3.5a). We measure the PL spectrum using the 550 nm excitation wavelength while maintaining the same excitation and emission slit width of the instrument. Finally, we multiplied the PL spectrums using the respective multiplication factors that arise from absorption unification (Figure 3.5b). The relative PL emission shows near unity recovery of PL emission in the case of MPQDs, whereas PbI_3^- treated QDs show 80% less emission in comparison to oleic acid capped PbS QDs (Figure 3.5b). Full recovery of PL emission indicates no increase in trap density and trap distribution in the case of MPQDs, whereas intermediate traps increase substantially in the case of PbI_3^- treated QDs.

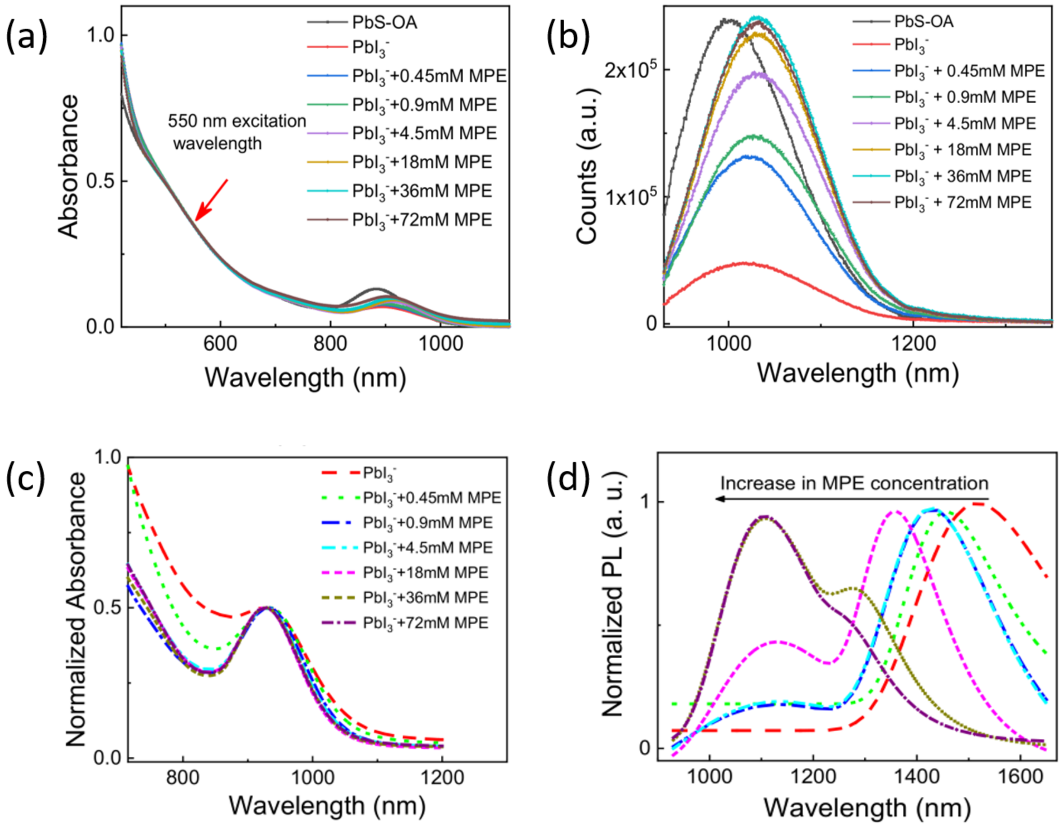

Figure 3.5: (a) Absorbance and (b) relative photoluminescence intensity of PbS QDs for different surface passivations. In the case of thin films, normalized absorbance and PL spectra are shown in (c) and (d), respectively. Colour code of (c) and (d) are maintained the same. All emissions are recorded for 550nm excitation wavelength.

Next, we turn our attention to the thin films of the PbS QDs passivated with different mixed ligand combinations. While the MPQDs show negligible redshift (~2 nm) in the 1st excitonic peak with respect to their solution-phase absorption, the PbI_3^- treated QDs suffered significant redshift (~26 nm) in their thin films (Figure 3.5c). In the case of incomplete ligand coverage, the QDs can grow through unpassivated surface sites when they come in physical contact with each other, through either Ostwald ripening[35], or infrequent formation of QD dimer[36], or both. We argue that the large redshift (~26 nm) and the broadening of the excitonic peak of PbI_3^- treated QD films could be due to inhomogeneous inter-dot diffusion, triggered by their incomplete ligand coverage. Whereas negligible redshift (~2 nm) in MPQDs could be due to the increase in QD to QD coupling in their thin-film, but the growth of QDs is restricted due to their near-optimal ligand coverage. The most striking change is observed in the PL spectra of the thin films (Figure 3.5d). In the case of PbI_3^- treated PbS QDs, the PL peak appears at 1520 nm, with the red shift of 594 nm. Upon increment of MPE ligands, the emission peak gradually blue shifts, and a separate peak at 1100 nm starts to appear. For MPQD films, the emission peak at 1100 nm is attributed to band edge emission from PbS QDs with the Stokes shift of 173 nm. The Stokes shift of band edge emission is increased by 63 nm in thin films, with respect to their solution-phase emission (Figure 3.5b). This could be due to efficient energy transfer towards lower bandgap QDs, facilitated by increased electronic coupling between QDs, in their thin films.[37] The systematic blue shift of long-wavelength emission peak (1520 nm) of PbI_3^--PbS QDs with the increase in MPE concentration indicates gradual elimination of low energy trap states from the QD film. The trap emission at lower energies (wavelength range 1250 nm to 1520 nm as shown in Figure 3.5d) could originate from infrequent fusion of QDs to form QD dimers in the solid films[36], or formation of sub-bandgap electronic traps states[38] due to sub-optimal surface passivation. The addition of MPE is not only successful in removing the low energy trap emission but also recovers the band edge emission of the PbS QDs in their thin films. Removal of intermediate trap states may reduce the recombination in solar cells to facilitate the current generation. Recovery in band edge emission would help restrict the Fermi energy pinning and increase the quasi-Fermi level splitting of electron and hole under optical illumination. This may help in increasing the photovoltage and current generation in solar cells.

3.3.3 Band edge determination by UPS

To take advantage of the superior optical properties of MPQDs, we fabricated solar cell devices using the reported n-p-p^+ device architecture.[8,26] We perform the Ultraviolet photoelectron spectroscopy (UPS) measurement to determine the valence band, conduction band, and Fermi energy values of the QD solids. PbS QD films are spin-coated on gold-coated silicon wafers for the UPS measurement. The samples are prepared and stored in air before they are transferred for the UPS measurement. He-Iα radiation of 21.22 eV is used for the measurement. From the full UPS spectra (Figure 3.6a), the onset energy region (OER) and secondary energy cutoff (SEC) is determined as shown in Figure 3.6b and 3.6c respectively. Band positions are determined as

Fermi energy level, $E_F = - (21.22 – SEC)$

Valence band level, $E_{VB} = E_F – OER$

Conduction band level, $E_{CB} = E_{VB} + E_g$

where the bandgap Eg is calculated from the 1st excitonic peak of the absorption spectra of the PbS QDs.

UPS study shows shallower conduction and valence band positions in MPQDs with respect to PbI_3^- passivated QDs (Figure 3.6d). This is consistent with the literature report, where thiol molecule passivation leads to shallower conduction and valence band edges in comparison to halogen ligands.[39] The positioning of Fermi energy close to the valence band indicates the p-type nature of PbS QDs for both the surface ligands.

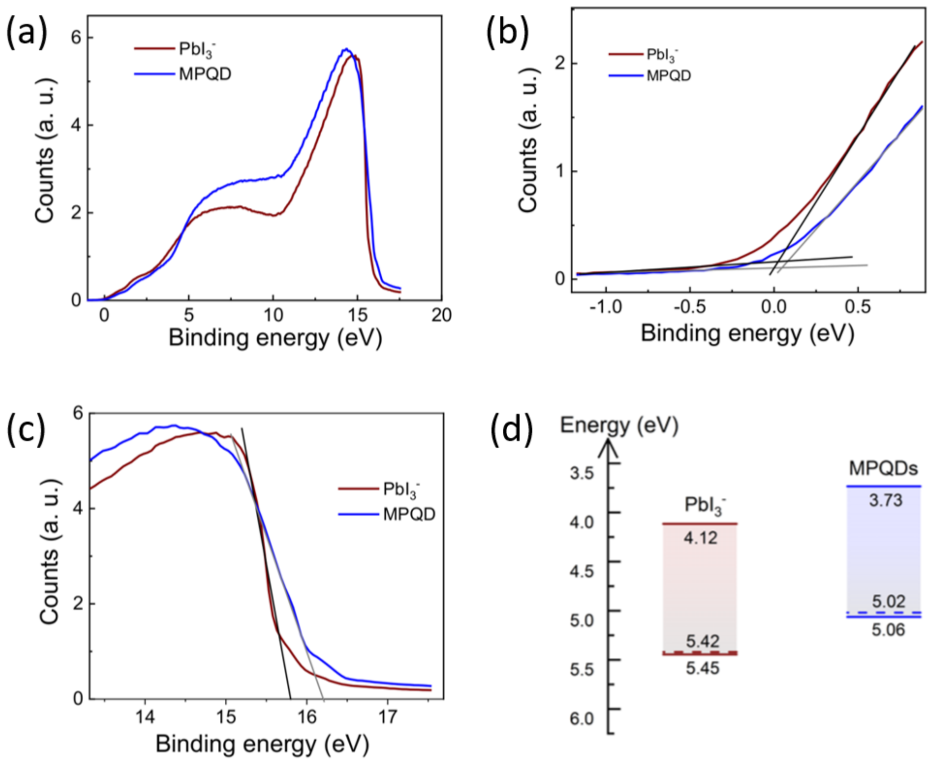

Figure 3.6: (a) Full range UPS spectra for PbI_3^--QD and MPQD films (b) shows the magnified view of the onset energy region (low binding energy region) and (c) shows the zoomed view of the secondary energy cut off region of the UPS spectrum. (d) band energy diagram of PbI_3^--QD and MPQD, determined from their UPS spectrum.

3.3.4 Current-voltage characteristics

To fabricate the photovoltaic devices, the electron transport n-layer is deposited by spin coating ZnO nanocrystals on top of the ITO-coated glass substrate.[7,8,26] The main light-absorbing p-layer is formed by depositing MPQDs (or PbI_3^- passivated PbS QDs) on top of the ZnO layer. The p-type, hole transport layer is formed by depositing 1,2-ethandithiol (EDT) treated PbS QDs by layer-by-layer approach.

The cross-sectional SEM image of a representative solar cell and the schematic picture of the device structure is shown in Figure 3.8a. Photovoltaic devices of mixed ligands treated QDs with varied concentrations of MPE ligands (0-72 mM) are studied to determine the optimum ligand combination. The comparative study of photovoltaic performances is shown in Figure 3.7, and Table 3.3. The power conversion efficiency of solar cells increases systematically with the increase in MPE concentration from 0 mM to 36 mM, due to the gradual increase in V_{OC}, J_{SC}, and FF. The increase in photovoltaic figure of merits with the increase in MPE concentrations suggests a steady improvement in QD passivation. However, MPE concentration beyond 36 mM, leads to a decrease in photovoltaic performances, even though superior emission properties are observed for 72 mM of MPE ligand (Figure 3.5d). Thin films for higher MPE concentrations (72 mM and higher concentrations) show a substantial increase in agglomerations, which could be responsible for their lower photovoltaic performances. Substitution of PbI_3^- ligand by MPE beyond a critical proportion compromises their dispersity in polar butylamine solvent, which leads to the agglomeration of QDs in their thin films. The highest photovoltaic performance is achieved for the mixed ligand combination of 0.1M PbI_3^- + 36 mM MPE. The optimum ligand combination for MPQDs is studied further, and the device parameters are compared with the reference PbI_3^- treated solar cells.

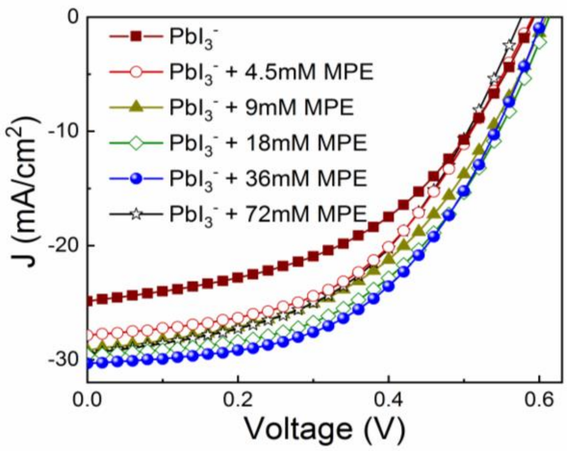

Figure 3.7: J-V characteristics of solar cells for different concentration of MPE ligands indicate improvement in photovoltaic parameters with increase in MPE concentration. The optimum ligand combination is found to be 0.1M PbI_3^- + 36 mM MPE.

Table 3.3 J-V characteristics of PbI_3^- and various concentrations of MPQDs.

Ligand	V_{OC} **(V)**	J_{SC} **(mA/cm^2)**	**FF**	**Efficiency (%)**
PbI_3^-	0.59	24.9	0.48	7.05
PbI_3^- + 4.5mM MPE	0.59	27.8	0.482	7.9
PbI_3^- + 9mM MPE	0.6	29.2	0.485	8.5
PbI_3^- + 18mM MPE	0.62	29.6	0.50	9.17
PbI_3^- + 36mM MPE	0.61	30.3	0.52	9.6
PbI_3^- + 72mM MPE	0.58	29.5	0.47	8.04

J-V characteristics of the best performing PbI_3^- and MPQDs based solar cells are shown in Figure 3.8b. The reference device shows V_{OC}: 0.59 V, J_{SC}: 24.9 mA cm^{-2}, FF: 0.48, and PCE: 7.05% in comparison to V_{OC}: 0.61 V, J_{SC}: 30.3 mA cm^{-2}, FF: 0.52, PCE: 9.6% of MPQDs based solar cell. The statistical variations of the photovoltaic parameters are compared for 10 numbers of reference PbI_3^- treated solar cells and 20 numbers of MPQD based solar cells. The measured photovoltaic parameters are shown in boxes, and the average values are indicated by lines, as shown in Figure 3.8c. The average gain in V_{OC}, J_{SC}, FF, and PCE in the case of MPQDs based solar cells is 4%, 22%, 5%, and 33% respectively. The EQE data shows enhanced photon to current conversion efficiency for the entire wavelength range of interest for MPQD based solar cells. The deviation in J_{SC}

calculated from EQE and measured from solar illumination is within 10%, as shown in Figure 3.8d.

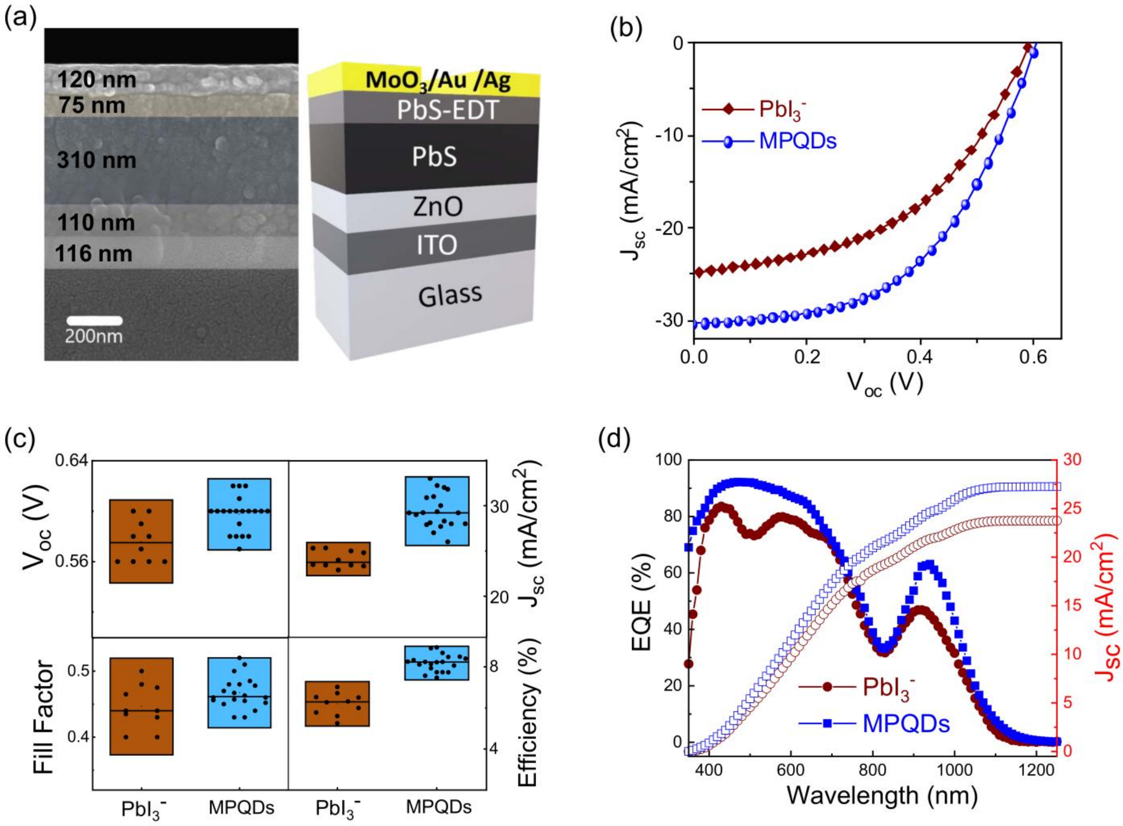

Figure 3.8: Solar cell characterizations. (a) cross-sectional SEM image of a representative solar cell along with schematic representation of various layers. (b) J-V characteristics (scan rate 0.1 V s^{-1}) of best performing solar cells based on reference PbI_3^- and mutually passivated QDs (MPQDs). (c) statistical distribution of photovoltaic parameters V_{OC}, J_{SC}, FF, and PCE are given. The average values of the parameters are represented by lines inside the boxes. (d) comparison of external quantum efficiency (EQE) of solar cells based on PbI_3^- and MPQDs.

3.3.5 Trap state densities for PbQDs and MPQDs

The increase in average V_{OC} (30 mV) is in line with the observation of lesser PL stokes shift and lesser Urbach energy in the case of MPQDs. The built-in potential estimated from the difference of light current and dark current is 0.67 V and 0.63 V for MPQDs and PbI_3^- treated QDs, respectively (Figure 3.9).[40] This indicates despite having identical energy bandgap and similar electron and hole transport layers, the open-circuit voltage increases in the case of MPQDs due to reduction in intermediate trap states and Fermi energy pinning across the interfaces.

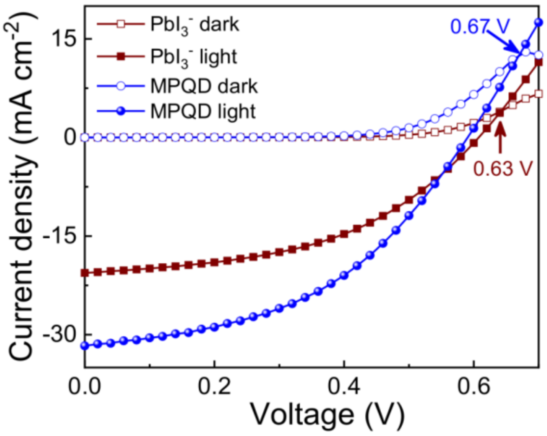

Figure 3.9: Built-in-potential is calculated from the inflection point of dark and light J-V curves of PbI_3^- and MPQD solar cells respectively. Built-in-potential for PbI_3^- is 0.63 V and MPQD shows 0.67 V.

We further estimated the density of intermediate trap states (DOS) across the bandgap of QDs, using the method reported for transient photovoltage and photocurrent measurements.[41-43] The number of trap states 'n' that need to be filled to generate a given V_{OC} is determined by

$$n = \frac{1}{Aqd}\int_0^{V_{oc}} C\, dV \quad \text{--} \quad (3.1)$$

Where q is electronic charge and A and d are the area and thickness of the solar cell. The differential capacitance C is determined from $C = \frac{\Delta Q}{\Delta V_{oc}}$; where ΔV_{oc} is the change in V_{OC} due to the light pulse measured from TPV data. The density of trap states can be expressed as $\frac{dn}{dV_{oc}}$.

The plot of $\frac{dn}{dV_{oc}}$ vs V_{OC} is shown in Figure 3.10a where DOS is significantly lower in MPQDs at any given V_{OC}. V_{OC} of a solar cell can be expressed as $V_{OC} = 1/q(E_{Fn}-E_{Fp})$[44]; where q is the electronic charge, E_{Fn} and E_{Fp} are quasi-Fermi levels for electron and hole respectively under photo-illumination. The situation is schematically depicted in Figure 3.10b. The estimation of DOS for different V_{OC} values give a vivid picture of the distribution of trap states across the bandgap of the active-PbS light-absorbing layer. The splitting of E_{Fn} and E_{Fp} is determined by the ratio of photo carriers that are at the conduction and valence band to the number of carriers that are trapped by the intermediate trap states. In the case of higher DOS, the number of trapped carriers will be higher to limit the quasi-Fermi energy splitting for electrons and holes. Lower DOS thereof produces higher photovoltage, as observed in the case of MPQDs based solar cells.

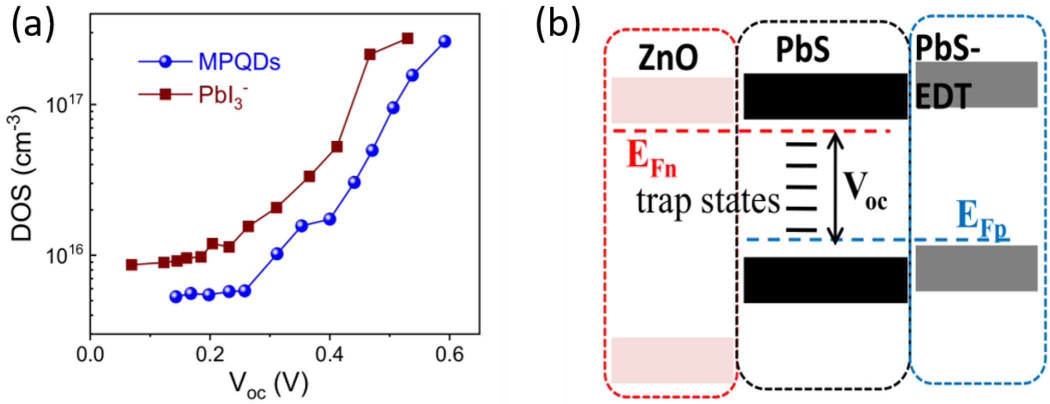

Figure 3.10: (a) Density of trap states at different V_{OC} values as determined from transient photovoltage and transient photocurrent measurements. (b) Schematic presentation of trap states across the band gap of PbS QDs.

3.3.6 Capacitance voltage measurement

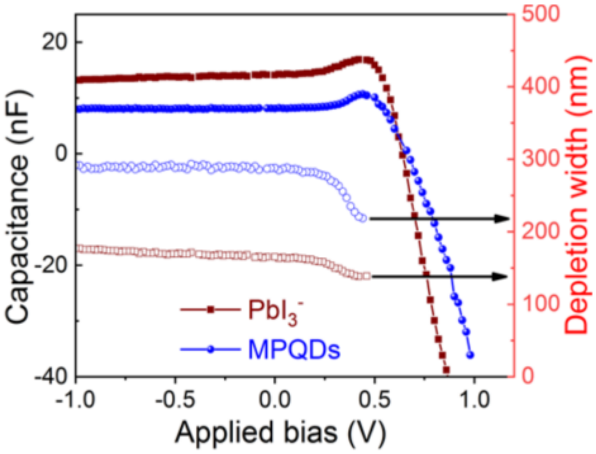

Figure 3.11: Capacitance-voltage characteristics measured under dark conditions at 1 kHz with scan rate of 0.1 V s^{-1}. Depletion width at various applied voltages is indicated by right hand side axis of the graph.

We carried out the capacitance-voltage measurement to estimate the depletion width in our n-p-p^+ type solar cells (Figure 3.11).[26,40] We note that due to the complexity in device configuration (heterogeneous interfaces and formation of two junctions n-ZnO/p-PbS and p-PbS/p^+-PbS-EDT), it is difficult to determine the depletion width accurately. Considering negligible depletion in highly doped ZnO and PbS-EDT layer and considering the relative permeability of 18 in the p-PbS layer,[45] we estimated the depletion width of 288 nm for MPQDs and 165 nm for PbI_3^- treated solar cells. Higher depletion width implies lower doping density in MPQDs, which corroborates with the findings from PL and DOS measurements. The carrier density determined from the capacitance-voltage data shows a doping density of 1.96×10^{16} cm^{-3} for MPQDs and 9.94×10^{16} cm^{-3} for PbI_3^- treated QDs.

3.3.7 Transient lifetime of MPQDs

Photocarrier lifetime and carrier mobility are the two important parameters that determine the diffusion length of the photocarriers. Transient photovoltage measurement (TPV) is used to determine the photocarrier lifetime at different open-circuit voltages.[29,46] The white light bias of varying intensities is used to generate different V_{OC} values, and a perturbation laser pulse is used to estimate the voltage decay time at a given V_{OC} (shown in Figure 3.12a). Photocarrier lifetime at any given V_{OC} is significantly higher in the case of MPQDs (Figure 3.12b), which could be due to the reduced recombination through the intermediate trap states.

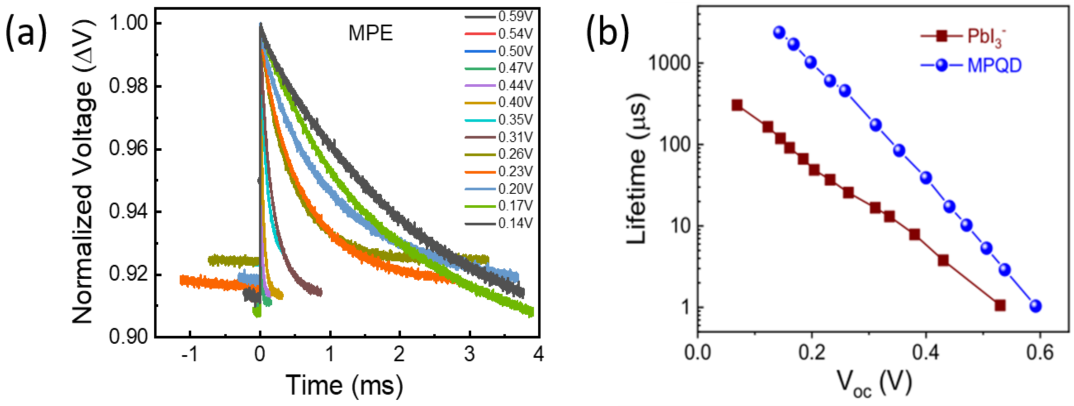

Figure 3.12: (a) Transient photovoltages obtained for MPE at different V_{OC} values. (b) Photocarrier lifetime at different V_{OC} measured from transient photovoltage (TPV) decay.

3.3.8 Carrier Mobility determination

Bias-dependent photocurrent decay measurement is employed to determine the carrier mobility in the solar cells.[43,47] The advantage of the technique is that it can be used readily in solar cell devices to estimate mobility. The photocurrent decay characteristics for MPQDs and conventional PbI_3^- treated solar cells are given in Figure 3.13(a,b). The carrier transit time (τ_{tr}) is estimated as the time taken to decay 1/e times of the maximum current value. Carrier mobility (μ) is determined using the formula, $\mu = d^2/(\tau_{tr} \times V)$; where d is the film thickness, and V is the applied bias. From the slope of the d^2/τ_{tr} vs V plot, carrier mobility for MPQDs is found to be slightly higher than conventional PbI_3^- as shown in Figure 3.13c. From the knowledge of carrier mobility and carrier lifetime, we estimated the diffusion length ($L_D=\sqrt{\mu(KT)\tau/q}$; K -Boltzmann constant, T –temperature (300 K), τ -carrier lifetime, and q -electronic charge) to be 94 nm and 52 nm for MPQDs and PbI_3^- treated solar cells, respectively. Higher carrier depletion width (Figure 3.11) and higher diffusion length (determined from Figure 3.10a and 3.12) facilitate efficient carrier extraction from thicker MPQDs layer, which corroborates with enhanced J_{SC} and higher FF in their solar cell devices.

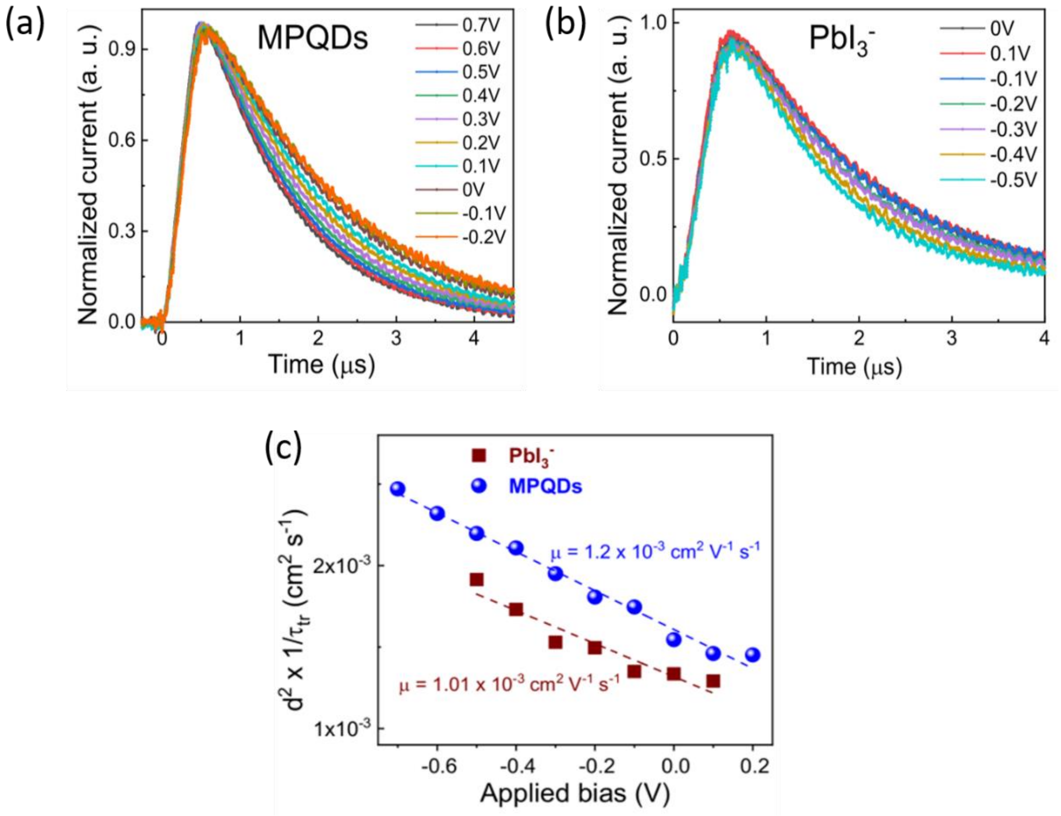

Figure 3.13: Decay profile of photocurrent under the influence of varied applied biases is shown for (a) MPQDs and (b) PbI_3^- solar cells. The carrier transit time (τ_{tr}) is determined as the time taken to decay 1/e times of the peak current value. (c) Charge carrier mobility is determined by measuring transient current decay at different applied biases. From the slope of d^2/τ_{tr} vs applied bias plot (where d is film thickness, and τ_{tr} is the carrier transit time) the mobility is estimated.

Table 3.4 Diffusion length and Drift length of PbI_3^-QDs and MPQDs

Ligand	**Depletion width (nm)**	**Diffusion length (L_d) (nm)**	**Drift length (D_l) (µm)**
PbI_3^-	165	52	0.5
MPE	290	94	1.06

3.3.9 X-ray photoelectron spectroscopy for passivation evidence

The involvement of MPE in the passivation of the QD surface is confirmed from the X-ray photoelectron spectroscopy (XPS) measurements. XPS study is carried out on thin film of PbS QDs deposited on gold-coated silicon substrates. High-resolution XPS spectra for S2p and C1s are fitted using CASA-XPS software. High-resolution S2p spectrum is deconvoluted using the following constraints: (i) for each chemical environment of sulfur, S2p peak is split into two peaks- $S2p_{3/2}$ and $S2p_{1/2}$, (ii) binding energy of $S2p_{1/2}$ appears at 1.18 eV higher energy than $S2p_{3/2}$ peak, and (iii) area under $S2p_{3/2}$ and $S2p_{1/2}$ peaks are maintained equal after relative sensitivity factor (RSF) consideration.[48,49] In the case of PbI_3^--QD film, the S2p spectrum is fitted by two sets of peaks, for which the binding energies of $S2p_{3/2}$ peaks appear at 161.59 eV and 165.12 eV. A minimum of three sets of peaks is required to fit the S2p spectrum of MPQDs, for which $S2p_{3/2}$ peaks appear at 161.56 eV and 163.91 eV and 165.96 eV. $S2p_{3/2}$ peak at 161.56 eV is attributed to the Pb-S bond of lead sulfide; 163.91 eV is attributed to the C-S bond of MPE and 165.96 eV is attributed to $S\text{-}O_x$ bond formation ($PbSO_x$) at the QD surface[48]. A comparison of C1s peaks shows that the characteristic peak of ester (COO) of MPE appeared at 288.35 eV, which is absent in PbI_3^--QD film. C1s peak of C-S bond superimposed with the C1s peak of C-N bond of butylamine which makes it difficult to identify. However, the presence of the C-S bond peak in S2p spectra and COO peak at C1s spectra confirms the presence of MPE at the QD surface. Further, to get insight into the surface condition of MPQDs, we performed an XPS study for varying concentrations of MPE ligands.

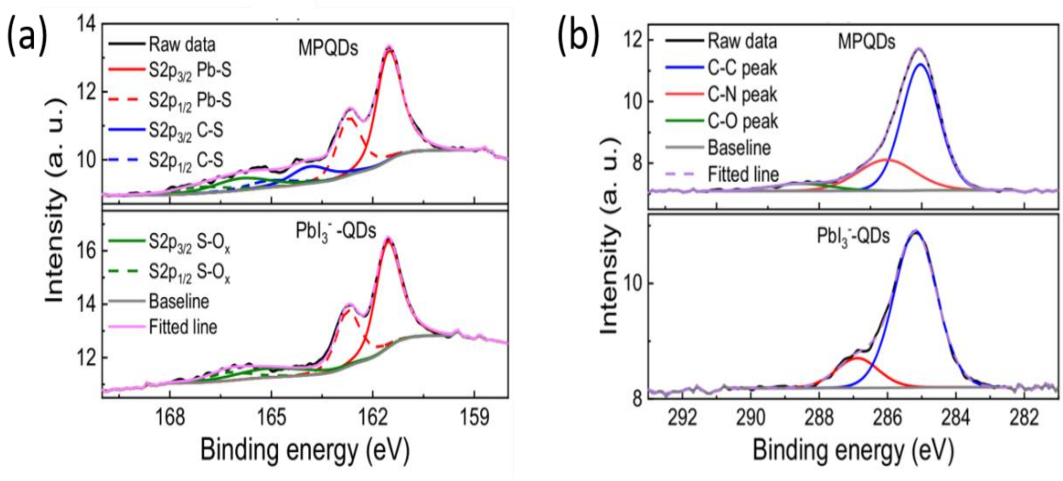

Figure 3.14: High-resolution XPS spectra of (a) S2p, and (b) C1s orbitals. The chemical environments of S for all deconvoluted peaks are assigned in the legends.

For the fixed PbI_3^- ligand concentration, as the MPE concentration increases, the Sulfur/Iodine ratio in MPQDs increases systematically, as observed from the XPS study (Figure 3.15). The increase in Sulfur/Iodine ratios with the increase in MPE concentrations, suggests the progressive addition of thiol molecules and decrease in iodine contribution at the QD surface.

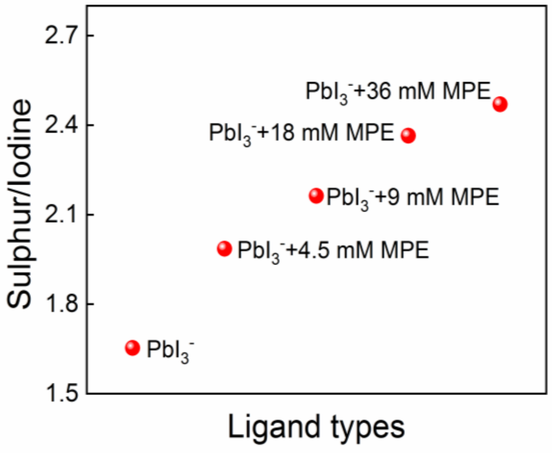

Figure 3.15: Sulfur to iodine ratio of PbS QDs for varied concentration of MPE ligands, determined from XPS analysis. Sulfur/iodine ratio increases with increase in MPE ligand concentrations.

3.3.10 TEM study of MPE passivated QDs

To elucidate the physical properties of the mutually passivated PbS QDs, we have carried out transmission electron microscopy (TEM) imaging. We note that amorphous and low electron density of the MPE molecule cannot be seen under TEM imaging, but we are interested in the morphological change of PbS QDs imparted by the mutual passivation. The TEM image of as-synthesized oleic acid capped QDs (Figure 3.16) shows a uniform size of 3 nm in diameter, consistent with their excitonic peak at 880 nm wavelength (Figure 3.3a). However, MPQDs and PbI_3^--QDs show a high degree of polydispersity in their shape and size, as shown in Figures 3.16 (a) and (b). The distribution of particle size as determined from the TEM images (Figure 3.16c), shows the average particle size for MPQDs is 5.84 nm, and 6.67 nm for PbI_3^--QDs. The TEM images of the MPQDs and PbI_3^--QDs show a significant increase in average particle size with respect to oleic acid-capped PbS QDs. The optical properties (absorbance and PL data) of the MPQDs and PbI_3^--QDs suggest that the size of the oleic acid capped PbS QDs increases only marginally (<0.1 nm) due to the ligand treatments. The discrepancy in size, observed in TEM images, and optical data could be due to the formation of the shell layer at the surface of QDs. As reported earlier, PbI_2 based ligand treatment forms a thick layer of perovskite shell (BA_2PbI_4) at the PbS QD surface during the solidification process[42]. For the TEM imaging, ultra-dilute (<1 mg/mL) solution of QD from their butylamine dispersion is drop cast on the TEM grids and allow them to dry slowly. The ionic ligands (PbI_3^- anions and BA^+ cations) present in the QD solution arrange to form the perovskite matrix shell during the film solidification process. We believe that the highly diluted solution of QDs allows the formation of a thick shell layer during the slow drying process on the TEM grids.

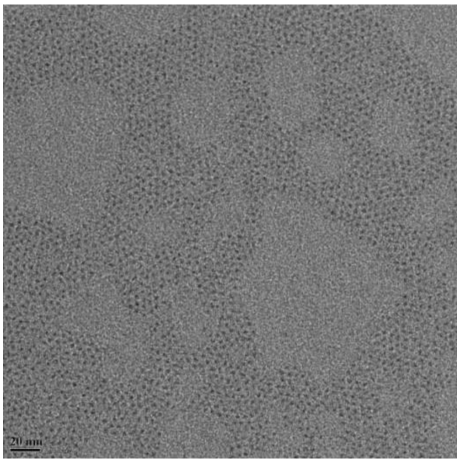

Figure 3.16: TEM image of oleic acid capped PbS QDs having excitonic peak at 880 nm. The average particle size is ~ 3nm.

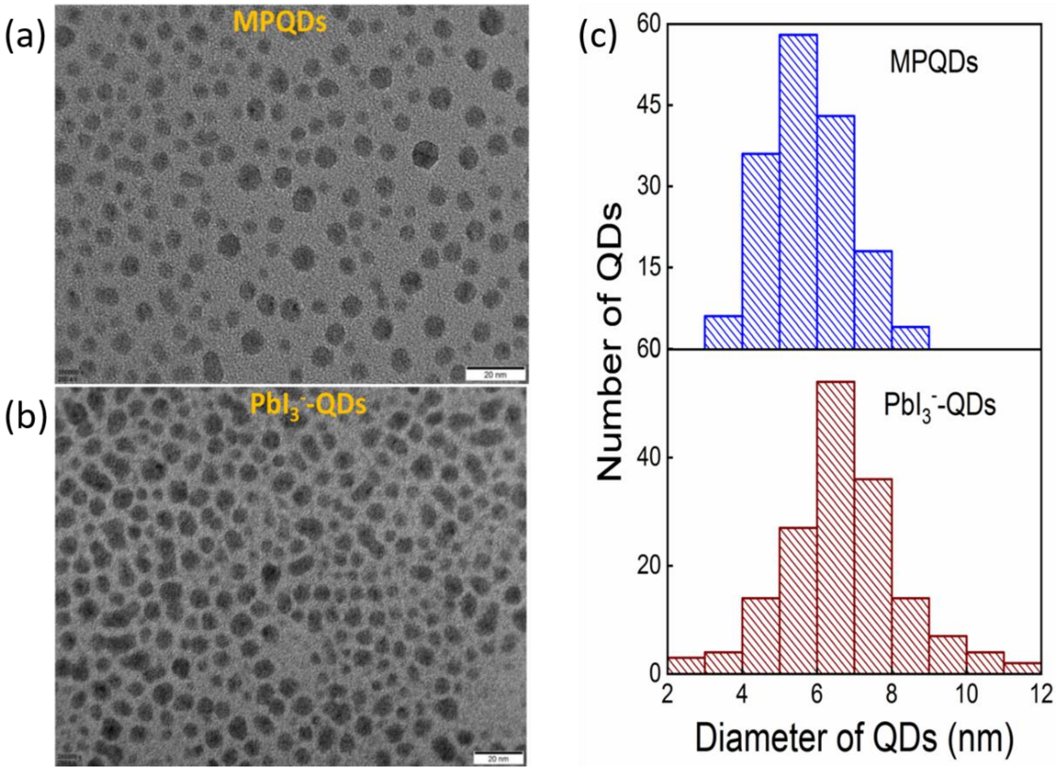

Figure 3.17: TEM images of (a) MPQDs and (b) PbI_3^--QDs are shown for comparison. (c) Size dispersion of MPQDs and PbI_3^--QDs, determined from their TEM images as shown beside.

3.4 Conclusion

In this chapter of the thesis, we have introduced MPE as a novel organic ligand to develop mutually passivated PbS QD ink, in conjugation with halometallate ligand. Size uniformity and trap free energy bandgap of as-synthesized oleic acid capped QDs, which normally deteriorate under short ligand exchange step, are maintained in the mutually passivated QDs. In comparison to conventional halometallate passivation, MPQDs show a five-time increase in PL emission, smaller stokes shift, and narrow Urbach energy, indicative of their excellent surface passivation. The resultant solar cells show higher V_{OC}, J_{SC}, and FF to improve the average solar cell performance by 33%. Improved photovoltaic parameters are supported by the significant reduction in intermediate trap density, increase in depletion width, and diffusion length in MPQD solar cells. The proposed strategy of mutual passivation can have significant implications in improving the optoelectronic properties of QD solids. This may find useful applications for the development of light-emitting diodes, photodetectors, and solar cells.

3.5 References

(1) Sun, Q.; Wang, Y. A.; Li, L. S.; Wang, D.; Zhu, T.; Xu, J.; Yang, C.; Li, Y. Bright, multicoloured light-emitting diodes based on quantum dots. *Nat. Photonics* **2007**, *1*, 717−722.

(2) Shirasaki, Y.; Supran, G. J.; Bawendi, M. G.; Bulović, V. Emergence of colloidal quantum-dot light-emitting technologies. *Nat. Photonics* **2013**, *7*, 13−23.

(3) Konstantatos, G.; Badioli, M.; Gaudreau, L.; Osmond, J.; Bernechea, M.; de Arquer, F. P. G.; Gatti, F.; Koppens, F. H. L. Hybrid graphene-quantum dot phototransistors with ultrahigh gain. *Nat. Nanotechnol.* **2012**, *7*, 363−368.

(4) Lee, J.-S.; Kovalenko, M. V.; Huang, J.; Chung, D. S.; Talapin, D. V. Band-like transport, high electron mobility and high photoconductivity in all-inorganic nanocrystal arrays. *Nat. Nanotechnol.* **2011**, *6*, 348−352.

(5) Lim, J.; Park, Y.-S.; Klimov, V. I. Optical gain in colloidal quantum dots achieved with direct-current electrical pumping. *Nat. Mater.* **2018**, *17*, 42−49.

(6) Semonin, O. E.; Luther, J. M.; Choi, S.; Chen, H. Y.; Gao, J. B.; Nozik, A. J.; Beard, M. C. Peak External Photocurrent Quantum Efficiency Exceeding 100% via MEG in a Quantum Dot Solar Cell. *Science* **2011**, *334*, 1530−1533.

(7) Chuang, C.-H. M.; Brown, P. R.; Bulović, V.; Bawendi, M. G. Improved performance and stability in quantum dot solar cells through band alignment engineering. *Nat. Mater.* **2014**, *13*, 796−801.

(8) Liu, M.; Voznyy, O.; Sabatini, R.; García de Arquer, F. P.; Munir, R.; Balawi, A. H.; Lan, X.; Fan, F.; Walters, G.; Kirmani, A. R.; Hoogland, S.; Laquai, F.; Amassian, A.; Sargent, E. H. Hybrid organic inorganic inks flatten the energy landscape in colloidal quantum dot solids. *Nat. Mater.* **2017**, *16*, 258−263.

(9) Hines, M. A.; Scholes, G. D. Colloidal PbS nanocrystals with size-tunable near-infrared emission: Observation of post-synthesis self-narrowing of the particle size distribution. *Adv. Mater.* **2003**, *15*, 1844−1849.

(10) Kagan, C. R.; Lifshitz, E.; Sargent, E. H.; Talapin, D. V. Building devices from colloidal quantum dots. *Science* **2016**, *353,* 5523.

(11) Boles, M. A.; Ling, D.; Hyeon, T.; Talapin, D. V. The surface science of nanocrystals. *Nat. Mater.* **2016**, *15*, 141−153.

(12) Kroupa, D. M.; Voros, M.; Brawand, N. P.; McNichols, B. W.; Miller, E. M.; Gu, J.; Nozik, A. J.; Sellinger, A.; Galli, G.; Beard, M. C. Tuning colloidal quantum dot band edge positions through solutionphase surface chemistry modification. *Nat. Commun.* **2017**, *8*, 15257.

(13) Tang, J.; Kemp, K. W.; Hoogland, S.; Jeong, K. S.; Liu, H.; Levina, L.; Furukawa, M.; Wang, X.; Debnath, R.; Cha, D.; Chou, K. W.; Fischer, A.; Amassian, A.; Asbury, J. B.; Sargent, E. H. Colloidal quantum-dot photovoltaics using atomic-ligand passivation. *Nat. Mater.* **2011**, *10*, 765−771.

(14) Rath, A. K.; Bernechea, M.; Martinez, L.; de Arquer, F. P. G.; Osmond, J.; Konstantatos, G. Solution-processed inorganic bulk nano-heterojunctions and their application to solar cells. *Nat. Photonics* **2012**, *6*, 529−534.

(15) Choi, M.-J.; García de Arquer, F. P.; Proppe, A. H.; Seifitokaldani, A.; Choi, J.; Kim, J.; Baek, S.-W.; Liu, M.; Sun, B.; Biondi, M.; Scheffel, B.; Walters, G.; Nam, D.-H.; Jo, J. W.; Ouellette, O.; Voznyy, O.; Hoogland, S.; Kelley, S. O.; Jung, Y. S.; Sargent, E. H. Cascade surface modification of colloidal quantum dot inks enables efficient bulk homojunction photovoltaics. *Nat. Commun.* **2020**, *11*, 103.

(16) Yuan, M.; Liu, M. X.; Sargent, E. H. Colloidal quantum dot solids for solution-processed solar cells. *Nat. Energy* **2016**, *1*, 16016.

(17) Carey, G. H.; Abdelhady, A. L.; Ning, Z.; Thon, S. M.; Bakr, O. M.; Sargent, E. H. Colloidal Quantum Dot Solar Cells. *Chem. Rev.* **2015**, *115*, 12732−12763.

(18) Zhang, J.; Tolentino, J.; Smith, E. R.; Zhang, J.; Beard, M. C.; Nozik, A. J.; Law, M.; Johnson, J. C. Carrier Transport in PbS and PbSe QD Films Measured by Photoluminescence Quenching. *J. Phys. Chem. C* **2014**, *118*, 16228−16235.

(19) Liu, Y.; Gibbs, M.; Puthussery, J.; Gaik, S.; Ihly, R.; Hillhouse, H. W.; Law, M. Dependence of Carrier Mobility on Nanocrystal Size and Ligand Length in PbSe Nanocrystal Solids. *Nano Lett.* **2010**, *10*, 1960−1969.

(20) Weidman, M. C.; Nguyen, Q.; Smilgies, D.-M.; Tisdale, W. A. Impact of Size Dispersity, Ligand Coverage, and Ligand Length on the Structure of PbS Nanocrystal Superlattices. *Chem. Mater.* **2018**, *30*, 807−816.

(21) Voznyy, O.; Zhitomirsky, D.; Stadler, P.; Ning, Z.; Hoogland, S.; Sargent, E. H. A Charge-Orbital Balance Picture of Doping in Colloidal Quantum Dot Solids. *ACS Nano* **2012**, *6*, 8448−8455.

(22) Zherebetskyy, D.; Scheele, M.; Zhang, Y.; Bronstein, N.; Thompson, C.; Britt, D.; Salmeron, M.; Alivisatos, P.; Wang, L.-W. Hydroxylation of the surface of PbS nanocrystals passivated with oleic acid. *Science* **2014**, *344*, 1380−1384.

(23) Erslev, P. T.; Chen, H. Y.; Gao, J. B.; Beard, M. C.; Frank, A. J.; van de Lagemaat, J.; Johnson, J. C.; Luther, J. M. Sharp exponential band tails in highly disordered lead sulfide quantum dot arrays. *Phys. Rev. B: Condens. Matter Mater. Phys.* **2012**, *86*, 155313.

(24) Balazs, D. M.; Dirin, D. N.; Fang, H.-H.; Protesescu, L.; ten Brink, G. H.; Kooi, B. J.; Kovalenko, M. V.; Loi, M. A. Counterion- Mediated Ligand Exchange for PbS Colloidal Quantum Dot Superlattices. *ACS Nano* **2015**, *9*, 11951−11959.

(25) Yang, Z.; Janmohamed, A.; Lan, X.; García de Arquer, F. P.; Voznyy, O.; Yassitepe, E.; Kim, G.-H.; Ning, Z.; Gong, X.; Comin, R.; Sargent, E. H. Colloidal Quantum Dot Photovoltaics Enhanced by Perovskite Shelling. *Nano Lett.* **2015**, *15*, 7539−7543.

(26) Mandal, D.; Goswami, P. N.; Rath, A. K. Thiol and Halometallate, Mutually Passivated Quantum Dot Ink for Photovoltaic Application. *ACS Appl. Mater. Interfaces* **2019**, *11*, 26100−26108.

(27) Gu, M.; Wang, Y.; Yang, F.; Lu, K.; Xue, Y.; Wu, T.; Fang, H.; Zhou, S.; Zhang, Y.; Ling, X.; Xu, Y.; Li, F.; Yuan, J.; Loi, M. A.; Liu, Z.; Ma, W. Stable PbS quantum dot ink for efficient solar cells by solution-phase ligand engineering. *J. Mater. Chem. A* **2019**, *7*, 15951− 15959.

(28) Tang, J.; Sargent, E. H. Infrared Colloidal Quantum Dots for Photovoltaics: Fundamentals and Recent Progress. *Adv. Mater.* **2011**, *23*, 12−29.

(29) Goswami, P. N.; Mandal, D.; Rath, A. K. The role of surface ligands in determining the electronic properties of quantum dot solids and their impact on photovoltaic figure of merits. *Nanoscale* **2018**, *10*, 1072−1080.

(30) Jeong, K. S.; Tang, J.; Liu, H.; Kim, J.; Schaefer, A. W.; Kemp, K.; Levina, L.; Wang, X.; Hoogland, S.; Debnath, R.; Brzozowski, L.; Sargent, E. H.; Asbury, J. B. Enhanced Mobility-Lifetime Products in PbS Colloidal Quantum Dot Photovoltaics. *ACS Nano* **2012**, *6,* 89−99.

(31) Moreels, I.; Lambert, K.; Smeets, D.; De Muynck, D.; Nollet, T.; Martins, J. C.; Vanhaecke, F.; Vantomme, A.; Delerue, C.; Allan, G.; Hens, Z. Size-Dependent Optical Properties of Colloidal PbS Quantum Dots. *ACS Nano* **2009**, *3*, 3023−3030.

(32) Giansante, C.; Infante, I.; Fabiano, E.; Grisorio, R.; Suranna, G. P.; Gigli, G. ″Darker-than-Black″ PbS Quantum Dots: Enhancing Optical Absorption of Colloidal Semiconductor Nanocrystals via Short Conjugated Ligands. *J. Am. Chem. Soc.* **2015**, *137*, 1875−1886.

(33) Hassanien, A. S.; Akl, A. A. Effect of Se addition on optical and electrical properties of chalcogenide CdSSe thin films. *Superlattices Microstruct.* **2016**, *89*, 153−169.

(34) Jean, J.; Mahony, T. S.; Bozyigit, D.; Sponseller, M.; Holovsky, J.; Bawendi, M. G.; Bulovic, V. Radiative Efficiency Limit with Band Tailing Exceeds 30% for Quantum Dot Solar Cells. *ACS Energy Lett.* **2017**, *2*, 2616−2624.

(35) Zhang, C.; Xia, Y.; Zhang, Z.; Huang, Z.; Lian, L.; Miao, X.; Zhang, D.; Beard, M. C.; Zhang, J. Combination of Cation Exchange and Quantized Ostwald Ripening for Controlling Size Distribution of Lead Chalcogenide Quantum Dots. *Chem. Mater.* **2017**, *29*, 3615−3622.

(36) Gilmore, R. H.; Liu, Y.; Shcherbakov-Wu, W.; Dahod, N. S.; Lee, E. M. Y.; Weidman, M. C.; Li, H.; Jean, J.; Bulović, V.; Willard, A. P.; Grossman, J. C.; Tisdale, W. A. Epitaxial Dimers and Auger- Assisted Detrapping in PbS Quantum Dot Solids. *Matter* **2019**, *1*, 250−265.

(37) Voznyy, O.; Levina, L.; Fan, F.; Walters, G.; Fan, J. Z.; Kiani, A.; Ip, A. H.; Thon, S. M.; Proppe, A. H.; Liu, M.; Sargent, E. H. Origins of Stokes Shift in PbS Nanocrystals. *Nano Lett.* **2017**, *17*, 7191−7195.

(38) Giansante, C.; Infante, I. Surface Traps in Colloidal Quantum Dots: A Combined Experimental and Theoretical Perspective. *J. Phys. Chem. Lett.* **2017**, *8*, 5209−5215.

(39) Brown, P. R.; Kim, D.; Lunt, R. R.; Zhao, N.; Bawendi, M. G.; Grossman, J. C.; Bulović, V. Energy Level Modification in Lead Sulfide Quantum Dot Thin Films through Ligand Exchange. *ACS Nano* **2014**, *8*, 5863−5872.

(40) Luther, J. M.; Law, M.; Beard, M. C.; Song, Q.; Reese, M. O.; Ellingson, R. J.; Nozik, A. J. Schottky Solar Cells Based on Colloidal Nanocrystal Films. *Nano Lett.* **2008**, *8*, 3488−3492.

(41) Ip, A. H.; Thon, S. M.; Hoogland, S.; Voznyy, O.; Zhitomirsky, D.; Debnath, R.; Levina, L.; Rollny, L. R.; Carey, G. H.; Fischer, A.; Kemp, K. W.; Kramer, I. J.; Ning, Z.; Labelle, A. J.; Chou, K. W.; Amassian, A.; Sargent, E. H. Hybrid passivated colloidal quantum dot solids. *Nat. Nanotechnol.* **2012**, *7*, 577−582.

(42) Shuttle, C. G.; O'Regan, B.; Ballantyne, A. M.; Nelson, J.; Bradley, D. D. C.; de Mello, J.; Durrant, J. R. Experimental determination of the rate law for charge carrier decay in a polythiophene: Fullerene solar cell. *Appl. Phys. Lett.* **2008**, *92*, 093311.

(43) Mandal, D.; Rath, A. K. Quantum Dots Coupled to an Oriented Two-Dimensional Crystalline Matrix for Solar Cell Application. *ACS Appl. Mater. Interfaces* **2018**, *10*, 39074−39082.

(44) Qi, B.; Wang, J. Open-circuit voltage in organic solar cells. *J. Mater. Chem.* **2012**, *22*, 24315−24325.

(45) Grinolds, D. D. W.; Brown, P. R.; Harris, D. K.; Bulovic, V.; Bawendi, M. G. Quantum-Dot Size and Thin-Film Dielectric Constant: Precision Measurement and Disparity with Simple Models. *Nano Lett.* **2015**, *15*, 21−26.

(46) Zhao, N.; Osedach, T. P.; Chang, L.-Y.; Geyer, S. M.; Wanger, D.; Binda, M. T.; Arango, A. C.; Bawendi, M. G.; Bulovic, V. Colloidal PbS Quantum Dot Solar Cells with High Fill Factor. *ACS Nano* **2010**, *4*, 3743−3752.

(47) Li, Z.; Gao, F.; Greenham, N. C.; McNeill, C. R. Comparison of the Operation of Polymer/Fullerene, Polymer/Polymer, and Polymer/Nanocrystal Solar Cells: A Transient Photocurrent and Photovoltage Study. *Adv. Funct. Mater.* **2011**, *21*, 1419−1431.

(48) Cao, Y.; Stavrinadis, A.; Lasanta, T.; So, D.; Konstantatos, G. The role of surface passivation for efficient and photostable PbS quantum dot solar cells. *Nat. Energy* **2016**, *1*, 16035.

(49) Castner, D. G.; Hinds, K.; Grainger, D. W. X-ray photoelectron spectroscopy sulfur 2p study of organic thiol and disulfide binding interactions with gold surfaces. *Langmuir* **1996**, *12*, 5083−5086.

(50) Rath, A. K.; Pelayo Garcia de Arquer, F.; Stavrinadis, A.; Lasanta, T.; Bernechea, M.; Diedenhofen, S. L.; Konstantatos, G. Remote Trap Passivation in Colloidal Quantum Dot Bulk Nanoheterojunctions and Its Effect in Solution-Processed Solar Cells. *Adv. Mater.* **2014**, *26*, 4741−4147.

Chapter 4

Solution phase partial ligand exchange for crack free and conjugated quantum dot hole transport layer

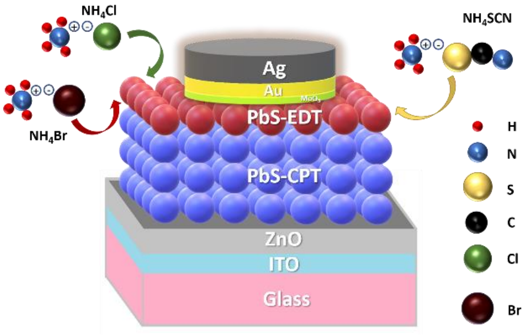

Abstract:

Colloidal quantum dots (QDs) have benefitted from solution-phase processing and bandgap tuning for their application in solar cell development. Today's QD solar cells rely on the solid-state ligand exchange (SLE) to replace bulky oleic acid ligands with short 1,2-ethanedithiol (EDT) ligands to develop conducting hole transport layer (HTL). However, high volume contraction in EDT conjugated QD films leads to crack and porosity in the HTL layer, which are detrimental to photovoltaic performance and device stability. We show that partial removal of oleic acid ligands in the solution phase reduces the volume contraction in solid films, thereby allow the growth of crack-free QD films in the SLE process. Conventional cleaning process by repeated precipitation and redispersion using protic methanol solvent helps partial removal of oleic acid ligands, but it is detrimental to the electronic properties of QDs. We develop a one-step solution-phase partial ligand exchange process using ammonium salts, which enables partial replacement of oleic acid ligands and passivation of the QD surface. The advancement in the partial ligand exchange process eliminates the need for tedious and wasteful multiple cleaning steps with MeOH while improving the photophysical properties of QDs. Partial ligand exchange with NH_4SCN leads to a 1.5 times increase in p-doping and mobility over MeOH cleaned PbS QD film. HTLs developed using NH_4SCN QDs shows improve photovoltaic performance to attain 10.5% power conversion efficiency. Improvement in depletion width and hole collection efficiency leads to superior photovoltaic performance, confirmed from experimental studies and one-dimensional solar cell capacitance simulation (SCAPS).

Chapter 4: Solution phase partial ligand exchange for crack free and conjugated quantum dot hole transport layer

4.1 Introduction

The previous chapter has illustrated the various benefits of colloidal quantum dots (QDs) as a potential building block for the development of next-generation optoelectronic devices.[1-11] Lead Sulfide (PbS) QDs as one of the top contenders in photovoltaic device development, owing to their wide range tunable bandgap[12], strong near infra-red (NIR) absorption[13], higher humidity tolerance[14], and high material abundance[15]. The advancements in QD surface functionalization have helped immensely in controlling physical properties[1,7,16,17], like solution-phase processing, size monodispersity (as evidenced in chapter 3), compact QD film formation, and reduction in the inter-dot distance in QD solids. Electrical properties of QDs solids like doping density[18,19], carrier mobility[20,21], intermediate trap states[22], and energy band positions[3] are also tuned by controlling the ligand chemistry. Advancements in surface passivation and device engineering have led to the steady progress of the QD solar cells.

The device architecture of a QD solar cell consists of a transparent electrode, an n-type electron transport window layer (ETL), a light-absorbing active QD layer, a hole transport layer (HTL), and a metal electrode.[1,4] Several excellent advancements have been made to improve the ETL[23-26] and the active QD layer[1,16,17,22,27-29] in the past. The development of the HTL to improve the performance of QD solar cells has gained significant research attention lately.[30-35] Several materials have been investigated for the development of the HTL layer, including organic semiconductors[36-38], metal oxides (e.g., MoO_3, NiO_x, etc.)[39-41], 2D semiconductors[42,43], and p-type QDs.[1,3,7,30,44,45] HTL layers made using surface-functionalized p-doped QDs yields the highest photovoltaic performance as of date.[1,44]

State-of-the-art HTLs are made by solid-state ligand exchange (SLE) of PbS QDs using 1,2-ethandithiol (EDT) as a ligand, first demonstrated by Luther et al., in 2008.[46] There have been efforts to improve the PbS-EDT layer by fluorenylmethyloxycarbonyl protected EDT,[47] mixing EDT with potassium thiocyanate[32] or methiopropamine,[33] infusing sulfur into the PbS-EDT layer,[35] and treatment by oxygen plasma.[48,49] In a typical SLE process, oleic acid (OA) capped native QDs solution is spin-coated to grow a thin film, the EDT ligand solution is then drop-cast and soaked for few seconds for the ligand exchange to complete. Finally, the film is washed with excess solvent to remove the unreacted ligands. The whole sequence is repeated to grow thicker films. Removal of eighteen carbon chain bulky OA by short ligand EDT (two carbon chain) leads to significant volume contraction (approximately 50%) in QD films, which often results in cracks and pores in the HTL layer.[46,50] Porous HTL layers are detrimental for solar cells as they allow the direct contact of the top electrode with the active QD layer, leading to poor photovoltaic performance and stability.

Protic solvents (ex: Methanol, ethanol) are reported to cleave the covalently bond OA from the QD surface via proton exchange.[51,52] We show that partial removal of OA ligand from the QD surface using repeated cleaning with methanol (MeOH), reduces the volume compression and improves the compactness of QD films grown using the SLE process. However, the electronic landscape of QDs deteriorates significantly due to repeated cleaning with MeOH, which increases size polydispersity and midgap trap states. We posit that partial replacement of surface-bound OA ligand using control interaction with short ligands in the solution phase would be rewarding. In this chapter, we discuss the development of a one-step solution-phase partial ligand exchange of native OA-PbS QDs using ammonium salts (NH_4Cl, NH_4Br, and NH_4SCN) as ligands. Ammonium salts assist partial removal of OA ligands and passivate of the surface sites by Cl, Br, or SCN ligands while maintaining their stable dispersion in non-polar solvents. The ammonium salts treated QDs enable growing compact and crack-free HTL layers in the SLE process, using EDT as a ligand (scheme shown in Figure 4.1). QDs subjected to one-step partial exchange with ammonium salts show improved photophysical properties and surface passivation compared to multiple cleaned methanol (MeOH). In the case of NH_4SCN ligand, QD films show 1.5 times increase mobility and doping density when compared with repeated MeOH treated films. HTLs fabricated using NH_4SCN QDs show an 11% increase in photovoltaic performance to attain absolute power conversion efficiency (PCE) of 10.5%. With the help of experimental studies and SCAPS simulation, we prove that increase in solar cell depletion width and superior hole collection by the NH_4SCN HTL layer leads to enhance photovoltaic performance.

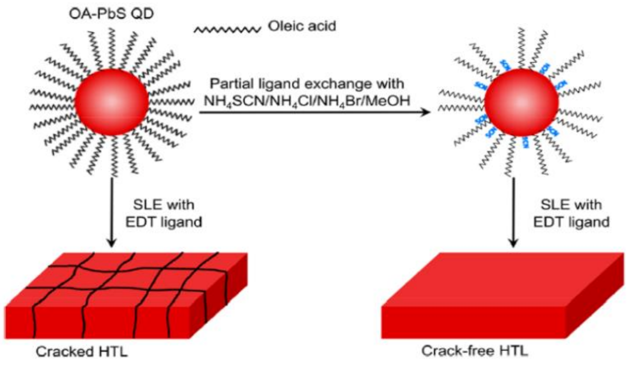

Figure 4.1: SLE of as-Synthesized OA-Capped PbS QDs by EDT, which causes cracks in the HTL. Smooth HTL film is obtained after partial OA removal with ammonium salts.

4.2 Experimental Details

4.2.1 PbS QD synthesis

Lead sulfide quantum dots were synthesized following a report from the literature.[17] In a three-necked flask, 0.45 g lead oxide (PbO) was taken followed by 3 mL 1-octadecene (ODE) and 1.5 mL of oleic acid (OA). The mixture was then degassed at a high vacuum at 95 °C under constant stirring overnight. The lead oleate is then shifted to argon atmosphere and temperature increased to 120 °C. 210 µL of hexamethyldisilithiane (TMS, in 10 mL ODE) is then swiftly injected into the lead oleate mixture and heating switched off. After cooling down, 10 mL of acetone is injected and stirred for 5 minutes. After precipitating with acetone, aliquots were centrifuged at 3000 rpm to separate PbS QDs. The QDs are redispersed in 4 mL toluene and precipitated by acetone. The QDs are were dried and finally dispersed in octane for further processing.

4.2.2 Ligand exchange

172 mg lead iodide (PbI_2), 45 mg lead bromide ($PbBr_2$), and 72 mg ammonium iodide (NH_4I) were dissolved in 5mL of dimethylformamide (DMF), and 10uL of 3-chloro-1-propanethiol (CPT) was added to prepare the stock solution (0.1 M) for p-type CPT PbS active layer. In a typical ligand exchange process, 5 mL of 14 mg/mL PbS QDs in octane were added to 5 mL of stock solution in a 30 mL centrifuge tube and vortexed vigorously for 2 minutes. This is to facilitate the transfer of QDs to the polar DMF phase. The clear octane solution at the top is then discarded and QDs are washed thrice with octane to remove any remaining traces of OA. DMF solution was filtered and then QDs

were precipitated by adding 6 mL toluene to it. QDs were centrifuged and the supernatant discarded. QDs were dried in vacuum for 20 minutes and then finally dispersed in butylamine to obtain a concentration of 250 mg/mL concentration.

4.2.3 OLA-PbS cleaning for HTL layer

Oleic acid capped PbS QDs (in octane) from stock solution were separately cleaned for HTL layer preparation. For the regular cleaning, PbS QDs were washed 8 times via sequential precipitation and dispersion using methanol and toluene respectively. After the 8th cleaning and final centrifugation step, PbS QDs were dried via argon flow and dispersed in octane with a concentration of 45 mg/mL. For the ammonium salts, 0.17 mM solution of respective salts (NH_4Br, NH_4Cl, and NH_4SCN) was prepared in methanol and added dropwise to diluted OLA-PbS QDs until clear precipitation was observed. Precipitated QDs were collected after centrifugation, dried as before, and dispersed in octane in a similar concentration.

4.2.4 Device fabrication

The bottom ETL layer was prepared by depositing ZnO nanocrystals on top of pre-cleaned ITO and heated at 250 °C as reported elsewhere.[28] CPT-PbS QDs from butylamine were then coated on top of the ZnO. The rotation speed of the spin coater was varied from 2000 r.p.m. – 4000 r.p.m. to obtain the layer thickness between 400 to 220 nm. The films thus formed were transferred to an Argon-filled glovebox where they were annealed at 70 °C for 10 minutes prior to HTL deposition. 0.01% 1,2-ethandithiol was used to grow 2 layers of respective PbS QD layers (arising out of different HTLs) on top of the pre-coated substrates to get a thickness of around 60 – 70nm of PbS-EDT. Substrates were stored overnight in argon atmosphere before proceeding to electrode deposition. Typically, 10 nm of molybdenum oxide (MoO_3), 30 nm of gold (Au), and 120 nm of silver (Ag) are vacuum-deposited using a thermal evaporator (HHV BC-300) at a base pressure below 5×10^{-6} Torr. The active area of the solar cells is 9 mm^2, as defined by the mask used for top electrode deposition.

4.2.5 Materials Characterization Techniques

Optical absorption measurements are carried out by a Shimadzu UV−vis−IR (UV-3600 Plus) spectrophotometer. An integrating sphere (ISR-603), attached to a Shimadzu UV-3600 Plus spectrophotometer is utilized to measure thin-film absorption.

Steady-state photoluminescence measurements are performed using Spectrofluorometer FS5 (Edinburgh Instruments). Sample holders SC-05 and SC-10 are used for holding cuvette and thin-film respectively. For the XPS study, Thermo Scientific K-Alpha+ spectrometer is utilized with the chamber in ultrahigh vacuum condition (10^{-9} mbar). Al Kα (1486.6 eV) is utilized as the monochromatic X-ray source with pass energy 50 eV for individual core levels. The XPS spectra are calibrated for the full XPS survey to the C 1s peak kept constant at a binding energy of 284.8 eV. CasaXPS software is used for the deconvolution and peak fitting of the XPS peaks. Surface charge neutralization is achieved utilizing an electron flood gun source for all of the measurements. UPS measurement is also carried out simultaneously with the same instrument using He-Iα radiation of energy 21.22 eV. Surface images under high magnification and cross-sectional images of the device are taken by a field emission scanning electron microscope (FESEM, NNS 450). The atomic force microscopy (AFM) images were taken using a Park Systems XE-70 microscope in noncontact mode with a scan rate of 0.5 Hz and a tip−sample distance of 13 nm throughout the measurements. The film roughness was determined by using the Parks XEI software.

4.2.6 Device Characterization Techniques

4.2.6.1 Current (J) – voltage (V) measurement

Current−voltage characteristics are measured under dark and illumination conditions under 1 sun illumination (AM 1.5) using a solar simulator (PEC-L01, Peccel) with a Keithley 2634B source meter. The solar intensity is set using a calibrated thermal detector (Thorlabs S302C).

4.2.6.2 Capacitance and Impedance measurement

Capacitance and Impedance measurements both were performed by PSM1735 (N4L) LCR meter. The capacitance measurement was carried out under dark at a frequency of 1KHz and a.c. perturbation voltage of 50 mV. Impedance measurement was carried out under illumination of 1 sun with frequency going from 1 KHz to 1 MHz while the applied bias was varied from 0 V to 0.55 V. The carrier density was determined from a $1/C^2$ versus voltage plot using the Mott−Schottky equation

$$N_d = \frac{2}{A^2 q \varepsilon_m \varepsilon_0 \frac{dC^{-2}}{dV}}$$

where N_d is the carrier density, C the capacitance, q the electronic charge, A the area of the pixel, ε_m the permittivity of PbS, and ε_0 the relative permittivity of air. The impedance measurement was carried out under solar illumination, with the frequency ranging between 100 Hz and 1 MHz, and the applied bias was varied between 0 and 0.55 V.

4.2.6.4 Mobility Measurement

Mobility is measured using the space charge limited current (SCLC) method. Schottky devices are constructed with HTL spin-coated (thick, >300 nm) on top of ITO substrates (pre-treated with silane to increase adhesiveness) followed by top electrode deposition. J-V measurements are taken in dark with voltage sweeping from -5 V to 5 V and linear fitting with slope = 2 is obtained from log J vs V plot which corresponds to SCLC regime ($J \alpha V^2$). The current and voltage values are then substituted in the Mott-Gurney relation $J = 9/8(\varepsilon_0 \varepsilon_r \mu V^2/L^3)$ and mobility of the HTL obtained.[35]

4.3 Results and Discussions

4.3.1 Morphological study of HTL

Crack-free and smooth HTL is crucial to prevent the direct contact of the top electrode with the active layer, which otherwise deteriorates the solar cell performance. For the efficient extraction of hole carriers, the thickness of the HTL layer is maintained below 100 nm in QD solar cells. Hence, any porosity in such a thin HTL layer would increase the chances of short formation and degradation of solar cells. When the bulky OA (18 carbon chain) ligands are replaced by small bidentate EDT (2 carbon chain) in the solid state, it leads to a rapid volume contraction and aggregation of QDs. As a result, cracks are formed in the QD films. Repeated precipitation and redispersion of QDs using protic MeOH helps to remove some of the surface-bound OA ligands from the QD surface.[51] This reduces the volume contraction in QD films grown using the SLE process. Figure 4.2 shows the surface morphology of PbS QD films for different cleaning steps with methanol (MeOH); depicted as nW-MeOH, where n-indicates the iteration number of MeOH cleaning. Atomic force microscopy (AFM) images of 2W-MeOH, 4W-MeOH, 6W-MeOH, and 8W-MeOH (Figure 4.2a-d) indicate a gradual decrease in QD agglomeration and film roughness. The average film roughness decreases sequentially from 3.72 nm to 0.89 nm with the increase in cleaning iteration from 2 to 8 times. Corresponding SEM images (Figure 4.2e-h) indicate a sequential decrease in cracks and the formation of compact QD films. This suggests multiple cleaning of OA caped PbS QDs with MeOH is critical for the development of crack-free and smooth HTL layers. However, the repeated cleaning process is highly wasteful, time-consuming, and lacks repeatability, as it involves multiple manual steps.

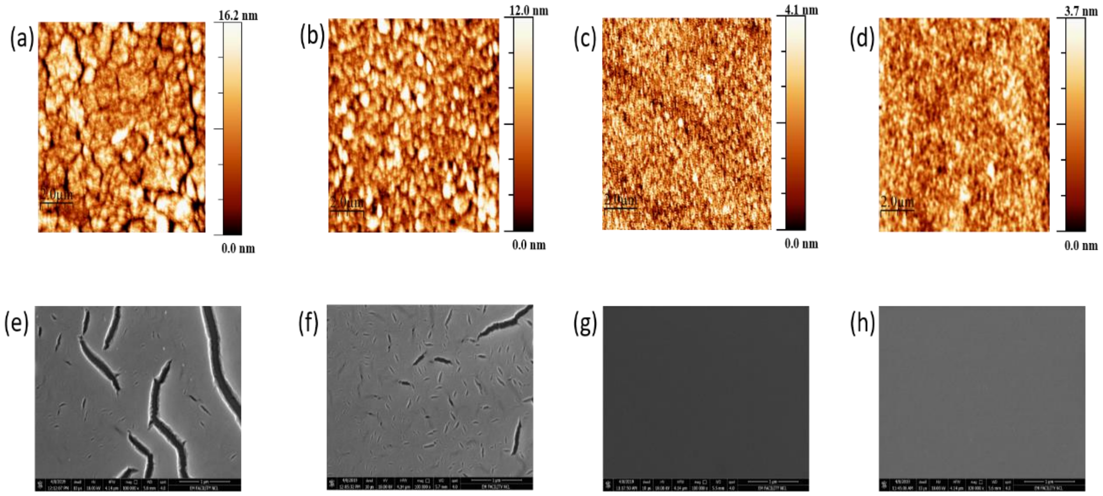

Figure 4.2: Surface properties of QD films. AFM (a, b, c, and d) and SEM (e, f, g, and h) images of PbS QD films for 2W-MeOH, 4W-MeOH, 6W-MeOH, and 8W-MeOH treatment, respectively.

We envisaged that partial replacement of bound OA ligands in the solution phase by small ligands would enable stable dispersion of QD in non-polar solvents, and the QD solution would then be used to form the compact film. This will help us bypass the tedious cleaning steps with MeOH. In this regard, we take a measured amount of ammonium salts (NH_4Cl, NH_4Br, NH_4I, and NH_4SCN) dissolved in MeOH, and add them to QD solutions in toluene separately till the QDs are precipitated from their toluene dispersion.

The precipitated QD samples are isolated, dried, and dispersed in octane (Figure 4.1) for HTL layer deposition using the SLE process. We observe that partial ligand exchange with NH_4Cl, NH_4Br, and NH_4SCN leads to a stable dispersion of QDs in nonpolar solvents, but NH_4I treated QDs are not dispersible. This can be explained using the hard-soft acid-base theory. Soft bases are more aggressive in reacting with terminal polar Pb atoms, which are considered soft acids. Due to this, I^- replace most of the OA ligands from the QD surface, which leads to the agglomeration and precipitation of PbS QDs in nonpolar solvents. AFM and SEM images of NH_4SCN, NH_4Cl, and NH_4Br (Figure 4.3 a-f) treated QDs show smooth, crack-free, and homogeneous QD film formation. The average film roughness for NH_4SCN and NH_4Cl are 0.78 nm and 0.63

nm, whereas, for NH_4Br, the average roughness increases to 4.62 nm. This could be because of mild agglomeration of PbS QDs, caused by the partial ligand exchange with NH_4Br.

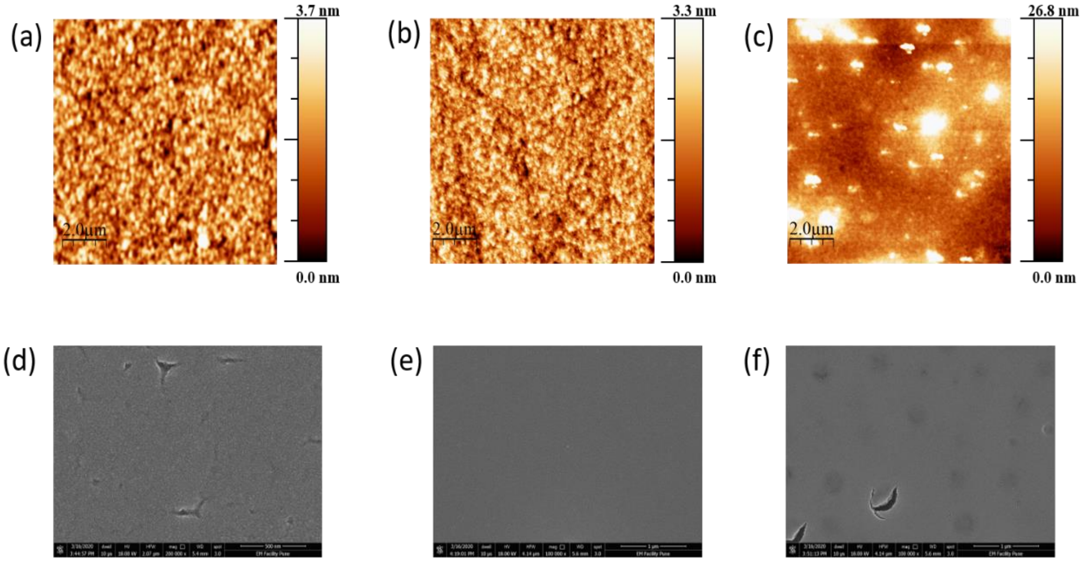

Figure 4.3: Surface properties of QD films. (a, b &c) AFM, and (d, e &f) SEM images of PbS QD films for NH_4SCN, NH_4Cl, and NH_4Br treatment.

4.3.2 Optical properties of PbS QDs in solution phase

Photophysical properties of QDs improve as we move from multiple MeOH cleaning to one-step partial ligand exchange with ammonium salts. It is observed that MeOH cleaning damages the excitonic peak of QDs. The 1st excitonic peak of PbS QDs blue shifts and broadened with every iteration of MeOH cleaning (Figure 4.4), while treatment with ammonium salts has milder effects on the excitonic absorption. Earlier reports suggest that MeOH can protonate the OA ligands to form free acid[51] and also etch the QD surface by removing the lead oleate complexes.[54] The QD core may decrease marginally because of oxidation via unprotected surface sites and etching of the lead oleate complex from the QD surface; as a result, the excitonic peak blue shifts by a few milli-electron volts. Comparison of the peak to valley ratio, half-width at half maximum (HWHM), and peak shift with respect to pristine PbS-OA are shown in Figure 4.4b. Degradation of the excitonic peak in multiple MeOH cleaned samples are evident in their large decrease in the peak to valley ratio and increase in HWHM. Ammonium salts treated QDs show a much smaller change in their peak position, HWHM, and peak to valley ratio. This shows that ammonium salts treatment is beneficial in maintaining the quantum confinement effect and size monodispersity in partially OA exchanged QDs.[12,28]

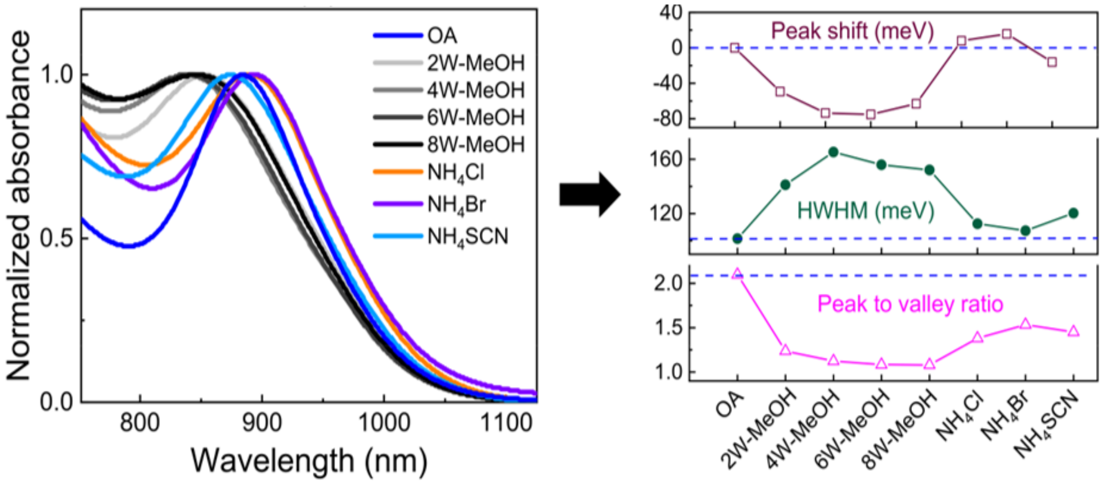

Figure 4.4: Photophysical property of QDs. Solution phase absorption of the 1st excitonic peak for various processing conditions in Octane and the evolution of peak to valley, HWHM, and peak shift with respect to pristine OA capped QDs, deduced from their corresponding absorption spectrums.

Estimation of band tail states from Urbach energy (E_u) calculation[55] shows an increase in E_u in MeOH cleaned QDs (Figure 4.5 and Table 4.1). In the case of NH_4SCN and NH_4Cl, E_u values are lower than the pristine PbS-OA, indicating a reduction in their band tail states. In the case of NH_4Br, however, E_u increases, which could be due to increased scattering due to mild agglomeration of PbS QDs in the solution phase.

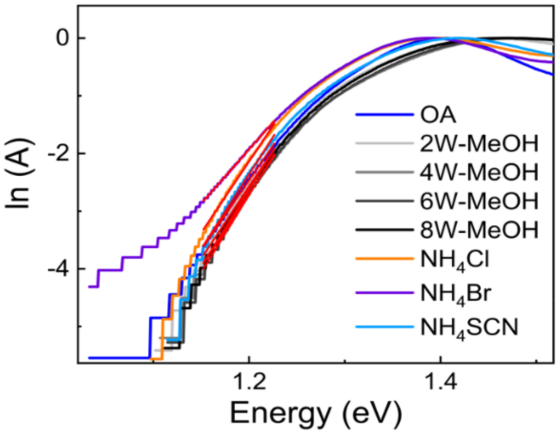

Figure 4.5: Absorbance (A) with energy in a semi-log plot. Urbach energy (E_u) is calculated from the linear fit of the absorbance onset of the 1st excitonic peak.

Table 4.1. The calculated E_u values for sequentially cleaned PbS and ammonium salts treated PbS are shown in tabular form.

HTL	E_u **(meV)**
PbS – OLA	41
PbS – 2R	44
PbS - 4R	43
PbS - 6R	42
PbS - 8R	42
NH_4Cl	38
NH_4Br	54
NH_4SCN	36

The emission spectra show a sequential decrease in peak intensity with the increase in MeOH cleaning iteration (Figure 4.6). This is consistent with earlier reports, and it is attributed to the formation of midgap electronic states in QDs due to the removal of surface-bound OA ligands.[51,53] Analysis of emission properties shows that ammonium salts treated QD samples show higher emission intensities (2 times or more compared to 8W-MeOH), lower FWHM, lower stokes shift compared with MeOH treated PbS QDs (Figure 2d). This suggests that ammonium salts treatments not only remove the OA ligands but protect the QD surface from electronic trap formation.

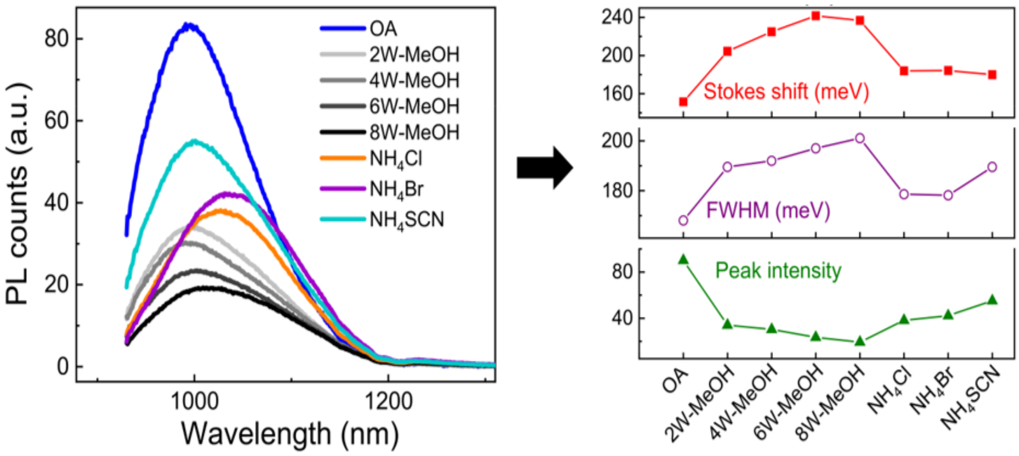

Figure 4.6: Photophysical property of QDs. (a) Emission spectra of PbS QDs dispersed in Octane. (b) Shows the peak intensity distribution, FWHM, and Stokes shift in emission spectrums.

4.3.3 X-ray photoelectron spectroscopy for passivation evidence

To probe the chemical environment of the QD surface X-ray photoelectron spectroscopy (XPS) is performed. Ammonium salts and 8W-MeOH treated QD solutions are used to grow thin films using EDT as the ligand. The films are deposited using the SLE method on gold-coated silicon substrates to carry out the XPS measurement. XPS data confirms that NH_4Cl and NH_4Br treated QDs retain Cl and Br passivation even after the EDT treatment (Figure 4.7a & b). The Fourier transform infrared data of an NH_4SCN treated QD film (grown using EDT ligands) shows a vibrational peak around 2040 cm^{-1}, corresponding to the CN stretching frequency (Figure 4.7c). The reference 8WMeOH film shows no such CN stretching peak. This confirms the presence of SCN in the NH_4SCN-treated QD film even after the EDT treatment.

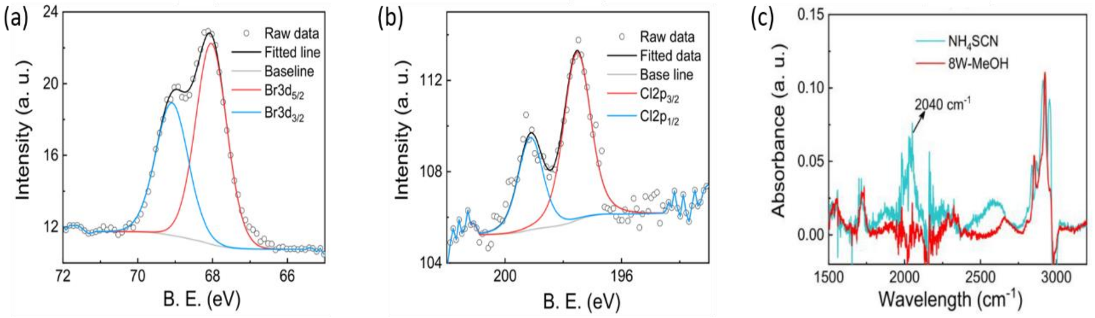

Figure 4.7: High-resolution XPS spectrum of (a) Cl 2p and (b) Br 3d orbital binding energies for NH_4Cl and NH_4Br treated QDs after their EDT treatment.

NH_4SCN treated QDs show an increase in the S/Pb ratio, suggesting an increase in S contribution with respect to 8W-MeOH films (Figure 4.8 a&b). Further, in all ammonium salts treated QD films S/Pb ratios are higher compared to 8W-MeOH films. This indicates that partial ligand exchange leads to superior ligand coverage of the QD surface. It is reported that the presence of small hydroxyl ligands (OH) on the polar (111) surface is a source of surface trap and instability in PbS QDs.[7] The high-resolution O1s XPS spectrum can be deconvoluted into three peaks, pertaining to different chemical species, as shown in Figure 4.8c. The peak at 531.86 eV (indicated by the red line) is assigned to the binding of surface Pb atoms with hydroxyl ligands.[7,56] The relative presence of OH species to unit lead contribution (OH/Pb ratio) is higher in the 8W-MeOH film in comparison to ammonium salts treated samples (Figure 4.8d). This suggests ammonium salts treated QD films possess lower numbers of OH-mediated midgap states.

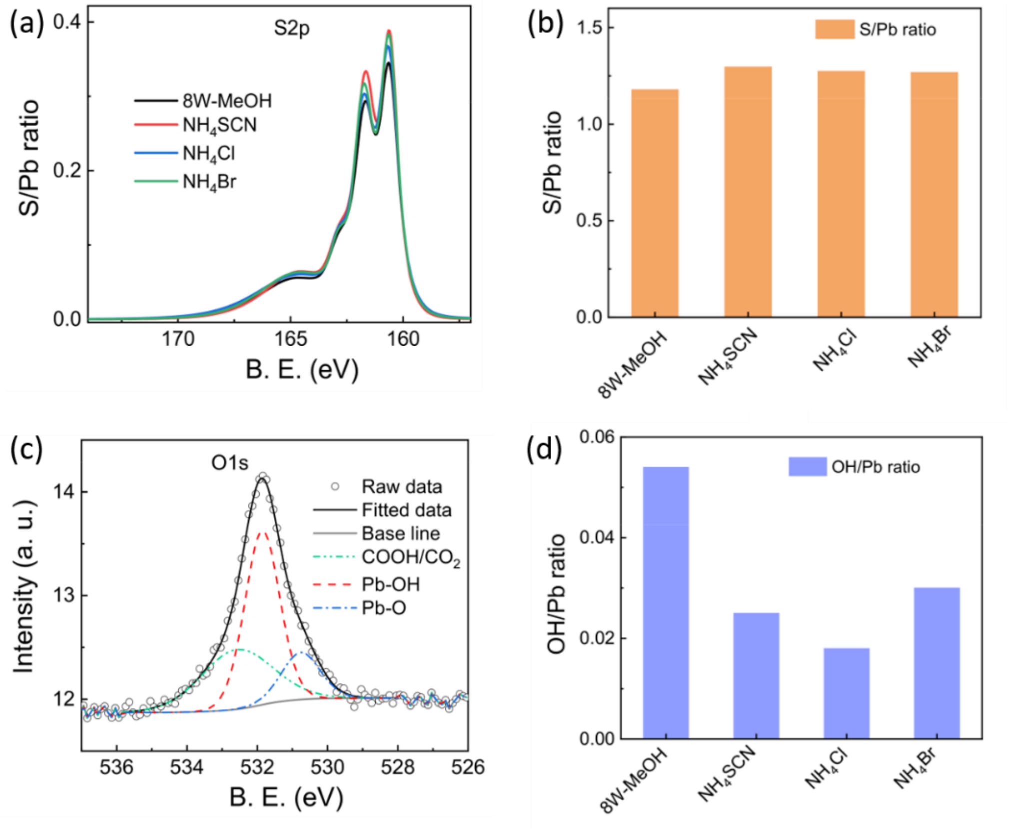

Figure 4.8: (a) S/Pb spectra and (b) S/Pb ratio for different ligands. Deconvolution of high-resolution. (c) O1s XPS spectrum for the representative 8W-MeOH PbS QD film. Legends indicate the presence of three different oxidative species on the QD surface for O1s. (d) OH/Pb ratios of PbS QD films for different ligand conditions.

Energy band positions of HTL layers are determined using ultraviolet photon spectroscopy (UPS) measurement. As discussed in the previous chapter, Fermi energy position (E_F) and valence band maxima (E_{VB}) are determined from the secondary cut-off and onset region of the UPS spectrum[57], as shown in Figure 4.9 a-c. Conduction band minima (E_{CB}) are determined from the bandgap obtained from the 1st excitonic peak position of the QDs. All the ammonium salt-treated QD samples show p-type characteristics, as shown in Figure 4.9d. There is a gradual shift in energy band edges to shallower energy values as we go from 8W-MeOH, NH_4SCN, NH_4Cl to NH_4Br. This suggests, ammonium salts treated QD films can be used as HTL for the development of QD solar cells.

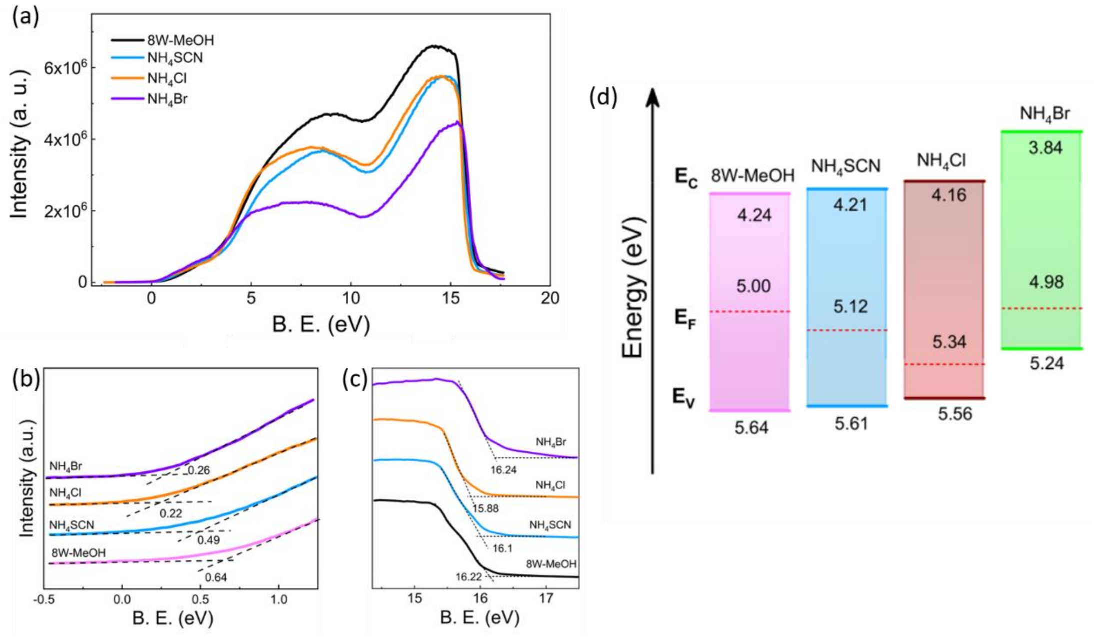

Figure 4.9: (a) Full energy range UPS spectra. Magnified low energy onset region (b) and (c) high energy secondary cut-off region of UPS spectra of different PbS QD films. (d) Energy level positions of different HTLs, determined from the UPS data. Fermi energy levels are shown with the red dotted line.

4.3.4 J-V characteristics

The schematic illustration of the device structure and the cross-sectional image of a representative solar cell device are shown in Figure 4.10a. ZnO NCs are spin-coated on pre-cleaned ITO substrate to grow the ETL layer. PbS QDs, passivated mutually by inorganic lead tri-iodide (PbI_3^-) and organic 3-Chloro-1-propanethiol (CPT)[28], is deposited on top of the ZnO layer to form the active layer (PbS-CPT). A thin HTL (approximately 80 nm thick) is deposited via the SLE method using EDT as a ligand. Partially ligand exchanged PbS QD solutions of 8W-MeOH, NH_4Cl, NH_4Br, and NH_4SCN are used to build the HTL layers. J-V characteristics of solar cells for different HTL layers are shown in Figure 4.10b and Table 4.2.

NH_4SCN treated HTL outperforms in solar cells due to the increase in all the photovoltaic parameters, and the increase in PCE is to the tune of 11% over 8W-MeOH. In the case of NH_4Cl and NH_4Br treated HTLs, V_{OC} remained unchanged, J_{SC} increases but FF decreases to yield comparable PCE with 8W-MeOH HTL. We further compare the statistical distribution of photovoltaic parameters of high-performing NH_4SCN with conventional 8W-MeOH for different batches (Figure 4.10d) of solar cells. The box chart indicates the maximum, minimum, and mean values of photovoltaic parameters. The mean values of photovoltaic parameters show increment in V_{OC}, J_{SC}, FF, and PCE in NH_4SCN treated solar cells.

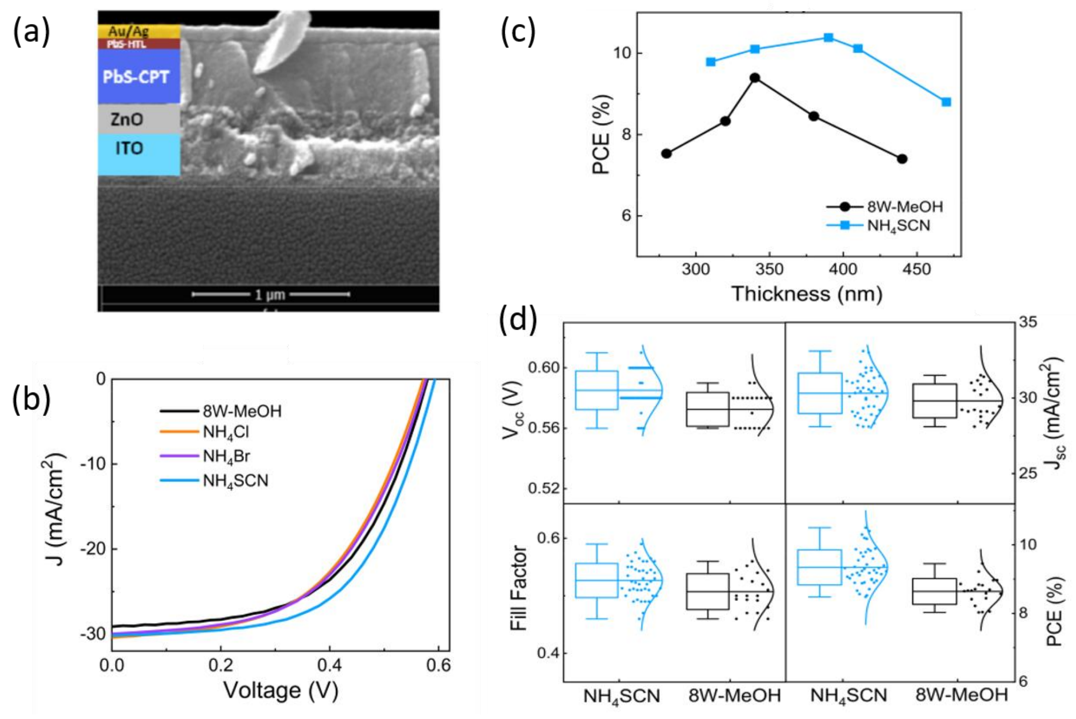

Figure 4.10: Photovoltaic device analysis. (a) cross-sectional SEM image of the solar cell device structure. (b) J - V curves of solar cells under 1.5AM illumination for various HTLs. (c) PCE as a function of thickness for solar cells. (d) The statistical distribution of photovoltaic parameters V_{OC}, J_{SC}, FF, and PCE for 8W-MeOH and NH_4SCN treated HTLs.

Table 4.2. Photovoltaic parameters of solar cell for different HTLs

HTL	V_{OC} **(V)**	J_{SC} **(mA/cm^2)**	**FF**	**PCE (%)**
8W-MeOH	0.58	29.1	0.56	9.44
NH_4Cl	0.58	30.4	0.52	9.16
NH_4Br	0.58	30	0.53	9.22
NH_4SCN	0.6	30.2	0.58	10.5

4.3.5 Capacitance voltage measurement

Capacitance voltage measurement is used to determine the carrier depletion width (W) of solar cells (Figure 4.11). Depletion width W is determined using the equation $W = \varepsilon_0\varepsilon_r A/C$; where ε_0 - permittivity of air, ε_r - relative permittivity of PbS QDs (considered as 43[28]), A - active area, C - capacitance. Depletion width at zero bias increases from 350 nm in 8W-MeOH to 400 nm in NH_4SCN. Higher depletion width would help carrier extraction from thicker active QD layer. The PCE of solar cells for the varied thickness of the active layer is shown in Figure 4.10c. NH_4SCN treated solar cells show higher

PCE values for the comparable thickness of the active layer, indicating superior charge extraction by PbS-NH_4SCN HTL. The optimized thickness for the active layer increases from 340 nm in 8W-MeOH to 390 nm in NH_4SCN solar cells, which matches closely with their respective depletion widths.

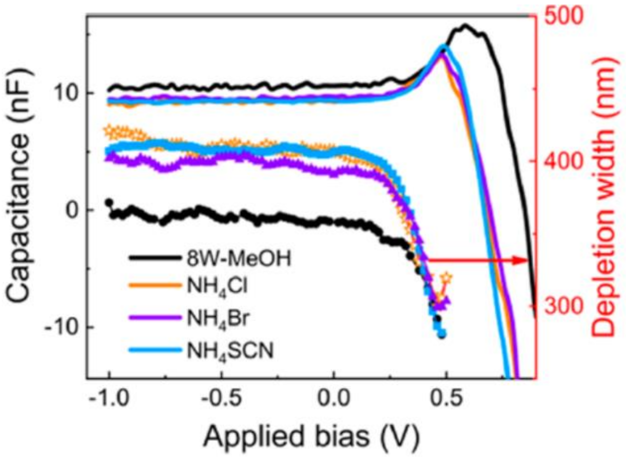

Figure 4.11: Capacitance-voltage characteristics of solar cells measured under dark conditions at 1 kHz with a scan rate of 0.1 V s^{-1}. Depletion width profiles are shown on the right-hand side axis of the graph.

4.3.6 Impedance measurement

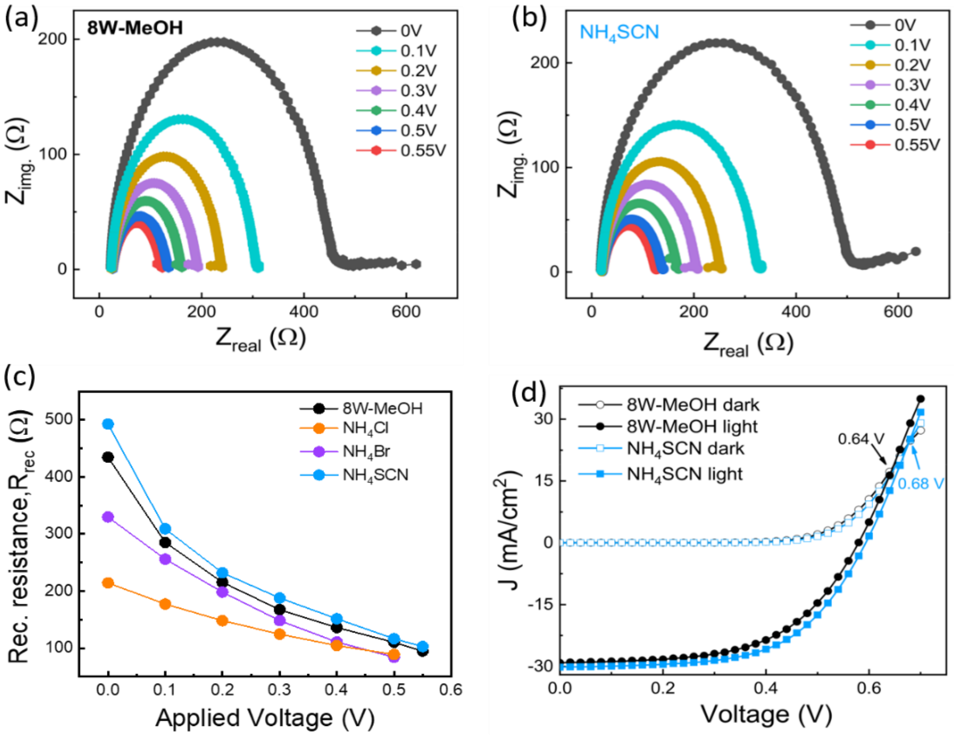

Figure 4.12: Cole-Cole plot of (a) 8W-MeOH, and (b) NH_4SCN HTL based solar cells. (c) Recombination resistance calculated from the cole-cole plot. (d) J-V characteristics of solar cells under dark and illuminated conditions.

Recombination resistances of solar cells under illumination are determined with the help of impedance spectroscopy. From the semi-circular Cole-Cole plots for different operating voltages recombination resistances are determined from their diameters (Figure 4.12 a&b)[58]. NH_4SCN solar cell shows higher recombination resistance than 8W-MeOH solar cells as evidenced from Figure 4.12c. Built-in voltages within the solar cells are compared from the inflection point of dark and light current.[59] NH_4SCN treated solar cells show 40 mV higher built-in voltage (Figure 4.12d). An increase in depletion width and recombination resistance supports the increase in J_{SC} and FF, and higher built-in voltage backs the increment in V_{OC} in NH_4SCN HTL solar cells.

4.3.7 Carrier densities for HTLs

Higher depletion width in the case of NH_4SCN HTL based solar cells points to higher hole majority carrier density. Rectifying devices are made using the device structure ITO/ZnO/HTL/Au, where ZnO-HTL junction forms the rectifying n-p junction (inset of Figure 4.13). Carrier densities are determined from $1/C^2$ vs voltage plot (Figure 4.13 a & b), using Mott-Schottky analysis[60], where C is the capacitance (please see method section for details). Relative variation of the hole carrier density for different HTLs follows the order of NH_4SCN (2.64×10^{17} cm^{-3}) > NH_4Cl (2.47×10^{17} cm^{-3}) > NH_4Br (1.80×10^{17} cm^{-3}) > 8W-MeOH (1.78×10^{17} cm^{-3}). The hole density for the best performing NH_4SCN HTL is found to be 1.5 times higher than that for the 8W-MeOH HTL.

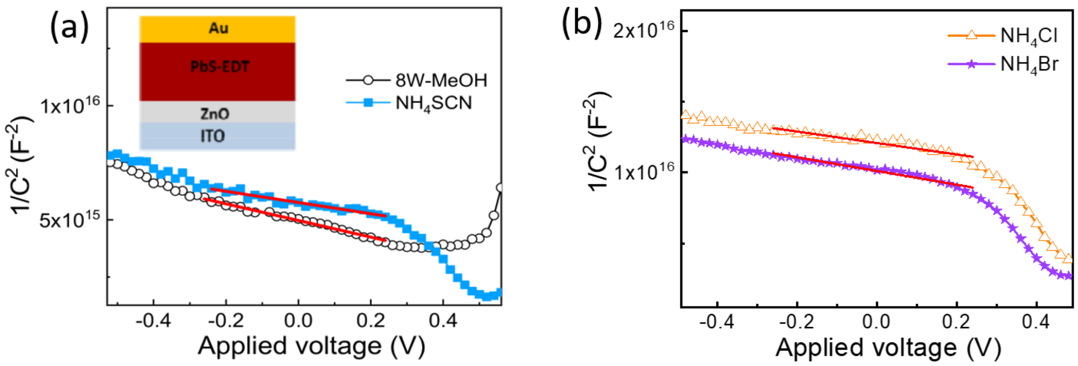

Figure 4.13: $1/C^2$ vs voltage plots for the device structure shown in the inset. Red lines indicate the fitted region around zero volts, used to determine doping densities in HTL layers.

4.3.8 Carrier Mobility determination

The space charge limited current (SCLC) method is employed to determine the hole mobility of HTLs. Hole-only devices are made using the device structure shown in Figure 4.14. From the J-V characteristics of the devices, hole mobilities are determined using Mott-Gurney's equation for the SCLC regime (please see method section for details). The HTL based on NH_4SCN shows the highest mobility (6.82×10^{-4} $cm^2/V{\cdot}s$), followed by 8W-MeOH (4.64×10^{-4} $cm^2/V{\cdot}s$), NH_4Br (3.15×10^{-4} $cm^2/V{\cdot}s$), and NH_4Cl (2.53×10^{-4} $cm^2/V{\cdot}s$). A higher hole mobility and hole density in the NH_4SCN-treated HTL would decrease the transport resistance to reduce the voltage drop due to charge transport and increase FF and J_{SC} of the solar cells.

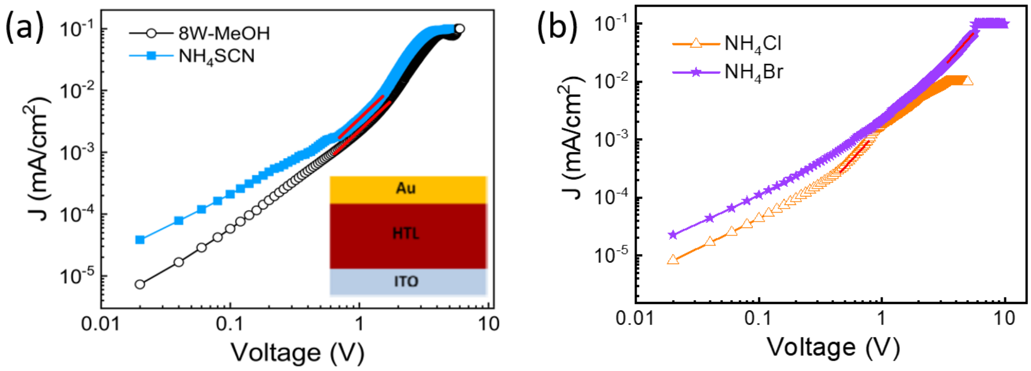

Figure 4.14: J-V curve (log-log scale) for the hole-only device (device structure is shown in the inset) to determine hole mobility from space charge limited conduction. SCLC regions are fitted using the red lines.

4.3.9 SCAPS Simulation

We further carried out the Solar Cell Capacitance Simulation (SCAPS) to elucidate the impact of improved electronic properties of the HTL layer on the solar cell performance.[35,61] Experimentally determined values of carrier mobility and doping density of HTL layers are used as inputs in SCAPS to calculate the J-V characteristics of the solar cells. SCAPS simulation of the J-V characteristics of solar cells for 8W-MeOH and NH_4SCN treated HTLs are shown in Figure 4.15a. SCAPS simulation predicts similar enhancement in V_{OC}, J_{SC}, FF, and PCE in NH_4SCN treated HTL based solar cells as observed experimentally (shown in Table 4.3). We further probe the recombination of photogenerated carriers with light travel distance inside the solar cell. For the identical thicknesses of the active layer, NH_4SCN treated HTL shows lower carrier recombination inside the active QD layer (Figure 4.15b). This suggests superior hole extraction efficiency in the case of NH_4SCN HTL. The simulation results validate the experimental findings and confirm that the improvement in the solar cell performances is due to the improvement in electronic properties of the NH_4SCN HTL layer. Details of the material parameters used for the simulation are given in Table 4.4.

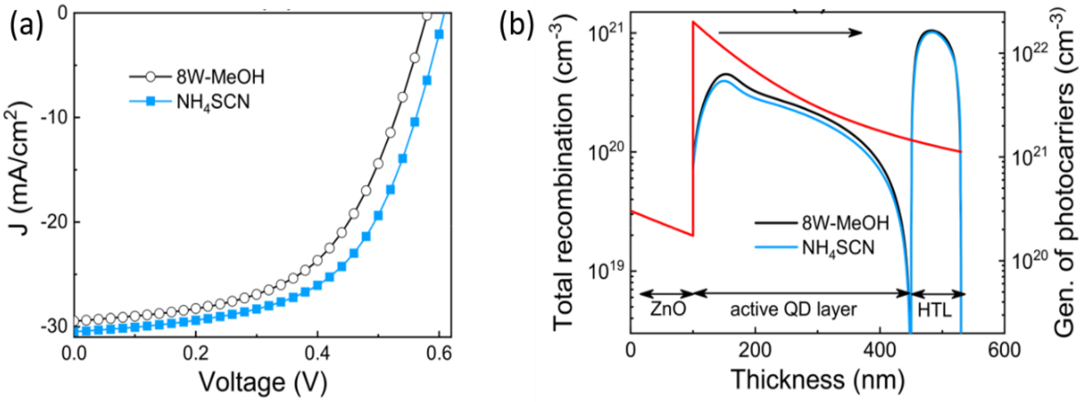

Figure 4.15: SCAPS simulation results; (a) J-V curve for solar cells, and (b) carrier generation and recombination with distance inside the solar cell. Light enters the solar cells from the ZnO side.

Table 4.3. SCAPS simulation results of solar cells for different HTLs

HTL	V_{OC} **(V)**	J_{SC} **(mA/cm^2)**	**FF**	**PCE (%)**
8W-MeOH	0.581	29.465	0.553	9.475
NH_4SCN	0.608	30.483	0.575	10.667

4.3.10 Stability

Stability of the unencapsulated solar cells with 8W-MeOH and ammonium salts HTL is observed over time wherein they are stored under argon and J - V measured in ambient conditions. The change in photovoltaic parameters (V_{OC}, J_{SC}, FF, and PCE) with time are shown in Figure 4.16. The PCE for NH_4SCN, 8W-MeOH, NH_4Br, and NH_4Cl is 0.73, 0.63, 0.60, and 0.55 of the original efficiency after ~1800 hours indicating higher stability for the NH_4SCN HTL.

Table 4.4. SCAPS parameters used for the simulation

Parameter	**ZnO**	**Active PbS QD**	**8W-MeOH PbS QD**	**NH_4SCN PbS QD**
Thickness (nm)	100	350/400	80	80
Bandgap (eV)	3.2	1.27	1.27	1.27
electron affinity (eV)	4.65	4.65	4.21	4.21
Relative dielectric permittivity	66	43	20	20
CB effective density of states ($1/cm^3$)	$1x10^{19}$	$1x10^{19}$	$1x10^{19}$	$1x10^{19}$
VB effective density of states ($1/cm^3$)	$1x10^{19}$	$1x10^{19}$	$1x10^{19}$	$1x10^{19}$
Electron & hole thermal velocity (cm/s)	$1x10^{7}$	$7x10^{3}$	$7x10^{3}$	$7x10^{3}$
electron mobility (cm^2/Vs)	$5x10^{-2}$	$7x10^{-3}$	$4.64x10^{-4}$	$4.64x10^{-4}$
hole mobility (cm^2/Vs)	$5x10^{-2}$	$7x10^{-3}$	$4.64x10^{-4}$	$6.82x10^{-4}$
shallow uniform donor density ND ($1/cm^3$)	$1x10^{18}$	$1x10^{15}$	$8x10^{16}$	$1x10^{16}$
shallow uniform acceptor density NA ($1/cm^3$)	0	$1.2x10^{16}$	$1.78x10^{17}$	$2.64x10^{17}$
Defect				
defect type	Neutral	Neutral	Neutral	Neutral
capture cross section electrons (cm^2)	$1x10^{-15}$	$1x10^{-13}$	$1x10^{-13}$	$1x10^{-13}$
capture cross section holes (cm^2)	$1x10^{-15}$	$1x10^{-13}$	$1x10^{-13}$	$1x10^{-13}$
energetic distribution	Single	Single	Single	Single
reference for defect energy level E_t	Above E_v (SCAPS<2.7)	Below E_c	Below E_c	Below E_c
energy level with respect to Reference (eV)	0.6	0.3	0.3	0.3
N_t total ($1/cm^3$)	$1x10^{14}$	$1x10^{15}$	$1x10^{16}$	$1x10^{16}$

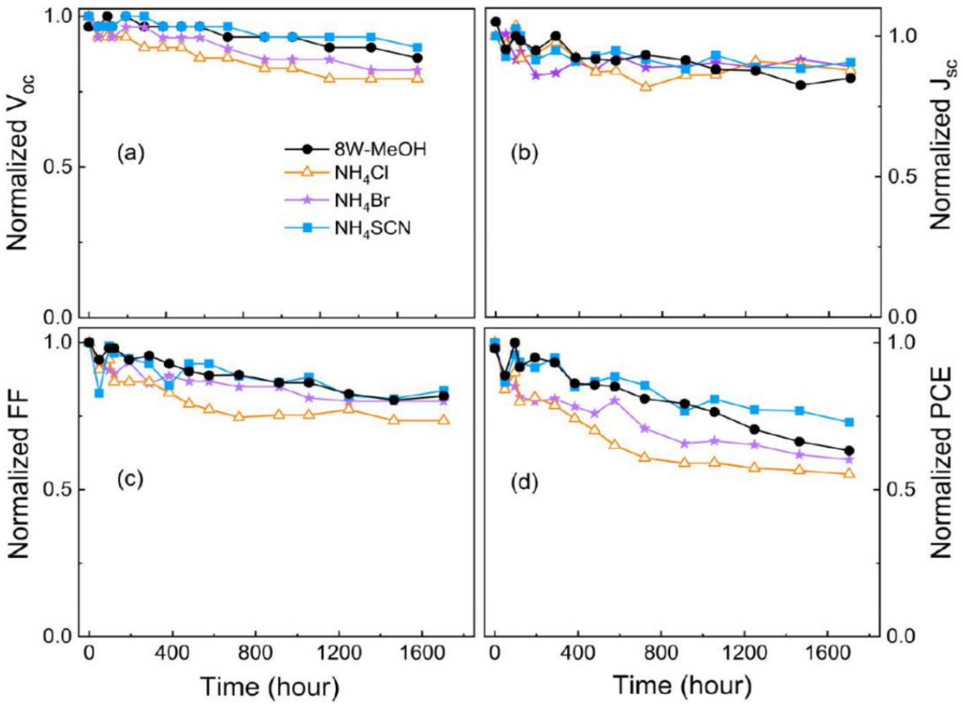

Figure 4.16: Photostability of the solar cells with regular and ammonium salts treated HTL on top.

4.4 Conclusion

Summarizing this chapter, we have shown that crack-free QD films can be grown using the SLE method through partial removal of native OA ligands. Repeated cleaning with protic MeOH solvent helps removing the covalently bound OA ligands from the QD surface, however, the quantum confinement and electronic properties degrade substantially. Solution phase partial ligand exchange with ammonium salts enables partial removal of OA ligands and helps to maintain the QD surface. The one-step partial ligand exchange process is efficient and useful in circumventing the tedious MeOH cleaning process. PbS QDs partially ligand exchanged with NH_4SCN shows an increase in p-doping and mobility while a decrease in trap states. HTLs developed using NH_4SCN treated QDs shows improved photovoltaic performance due to superior hole extraction efficiency. The proposed strategy of partial ligand exchange to grow thin and crack-free QD film can find widespread applications in the research and development of QD-based light-emitting diodes, photodetectors, and solar cells.

4.5 References

(1) Sun, B.; Johnston, A.; Xu, C.; Wei, M. Y.; Huang, Z. R.; Jiang, Z.; Zhou, H.; Gao, Y. J.; Dong, Y. T.; Ouellette, O.; Zheng, X. P.; Liu, J. K.; Choi, M. J.; Gao, Y.; Baek, S. W.; Laquai, F.; Bakr, O. M.; Ban, D. Y.; Voznyy, O.; García de Arquer, F. P.; Sargent, E. H. Monolayer Perovskite Bridges Enable Strong Quantum Dot Coupling for Efficient Solar Cells. *Joule* **2020**, *4* (7), 1542−1556.

(2) Lee, H.; Song, H. J.; Shim, M.; Lee, C. Towards the commercialization of colloidal quantum dot solar cells: perspectives on device structures and manufacturing. *Energy Environ. Sci.* **2020**, *13* (2), 404−431.

(3) Chuang, C. H. M.; Brown, P. R.; Bulovic, V.; Bawendi, M. G. Improved performance and stability in quantum dot solar cells through band alignment engineering. *Nat. Mater.* **2014**, *13* (8), 796− 801.

(4) Kagan, C. R.; Lifshitz, E.; Sargent, E. H.; Talapin, D. V. Building devices from colloidal quantum dots. *Science* **2016**, *353* (6302), aac5523.

(5) Aqoma, H.; Jang, S. Y. Solid-state-ligand-exchange free quantum dot ink-based solar cells with an efficiency of 10.9%. *Energy Environ. Sci.* **2018**, *11* (6), 1603−1609.

(6) Lu, K. Y.; Wang, Y. J.; Liu, Z. K.; Han, L.; Shi, G. Z.; Fang, H. H.; Chen, J.; Ye, X. C.; Chen, S.; Yang, F.; Shulga, A. G.; Wu, T.; Gu, M. F.; Zhou, S. J.; Fan, J.; Loi, M. A.; Ma, W. L. High-Efficiency PbS Quantum-Dot Solar Cells with Greatly Simplified Fabrication Processing via "Solvent-Curing". *Adv. Mater.* **2018**, *30* (25), 1707572.

(7) Cao, Y. M.; Stavrinadis, A.; Lasanta, T.; So, D.; Konstantatos, G. The role of surface passivation for efficient and photostable PbS quantum dot solar cells. *Nat. Energy* **2016**, *1*, 16035.

(8) Konstantatos, G.; Badioli, M.; Gaudreau, L.; Osmond, J.; Bernechea, M.; de Arquer, F. P. G.; Gatti, F.; Koppens, F. H. L. Hybrid graphene-quantum dot phototransistors with ultrahigh gain. *Nat. Nanotechnol.* **2012**, *7* (6), 363−368.

(9) Gao, J. B.; Nguyen, S. C.; Bronstein, N. D.; Alivisatos, A. P. Solution-Processed, High-Speed, and High-Quantum-Efficiency Quantum Dot Infrared Photodetectors. *ACS Photonics* **2016**, *3* (7), 1217−1222.

(10) Shirasaki, Y.; Supran, G. J.; Bawendi, M. G.; Bulovic, V. Emergence of colloidal quantum-dot light-emitting technologies. *Nat. Photonics* **2013**, *7* (1), 13−23.

(11) Pradhan, S.; Dalmases, M.; Baspinar, A. B.; Konstantatos, G. Highly Efficient, Bright, and Stable Colloidal Quantum Dot Short- Wave Infrared Light-Emitting Diodes. *Adv. Funct. Mater.* **2020**, *30* (39), 2004445.

(12) Hines, M. A.; Scholes, G. D. Colloidal PbS nanocrystals with size-tunable near-infrared emission: Observation of post-synthesis self-narrowing of the particle size distribution. *Adv. Mater.* **2003**, *15* (21), 1844−1849.

(13) Cademartiri, L.; Montanari, E.; Calestani, G.; Migliori, A.; Guagliardi, A.; Ozin, G. A. Size-dependent extinction coefficients of PbS quantum dots. *J. Am. Chem. Soc.* **2006**, *128* (31), 10337−10346.

(14) Kirmani, A. R.; Sheikh, A. D.; Niazi, M. R.; Haque, M. A.; Liu, M. X.; de Arquer, F. P. G.; Xu, J. X.; Sun, B.; Voznyy, O.; Gasparini, N.; Baran, D.; Wu, T.; Sargent, E. H.; Amassian, A. Overcoming the Ambient Manufacturability-Scalability-Performance Bottleneck in Colloidal Quantum Dot Photovoltaics. *Adv. Mater.* **2018**, *30* (35), 1801661.

(15) Wadia, C.; Alivisatos, A. P.; Kammen, D. M. Materials Availability Expands the Opportunity for Large-Scale Photovoltaics Deployment. *Environ. Sci. Technol.* **2009**, *43* (6), 2072−2077.

(16) Liu, M. X.; Voznyy, O.; Sabatini, R.; García de Arquer, F. P.; Munir, R.; Balawi, A. H.; Lan, X. Z.; Fan, F. J.; Walters, G.; Kirmani, A. R.; Hoogland, S.; Laquai, F.; Amassian, A.; Sargent, E. H. Hybrid organic-inorganic inks flatten the energy landscape in colloidal quantum dot solids. *Nat. Mater.* **2017**, *16* (2), 258−263.

(17) Mandal, D.; Goswami, P. N.; Rath, A. K. Thiol and Halometallate, Mutually Passivated Quantum Dot Ink for Photovoltaic Application. *ACS Appl. Mater. Interfaces* **2019**, *11* (29), 26100−26108.

(18) Voznyy, O.; Zhitomirsky, D.; Stadler, P.; Ning, Z. J.; Hoogland, S.; Sargent, E. H. A Charge-Orbital Balance Picture of Doping in Colloidal Quantum Dot Solids. *ACS Nano* **2012**, *6* (9), 8448−8455.

(19) Norris, D. J.; Efros, A. L.; Erwin, S. C. Doped nanocrystals. *Science* **2008**, *319* (5871), 1776−1779.

(20) Liu, Y.; Gibbs, M.; Puthussery, J.; Gaik, S.; Ihly, R.; Hillhouse, H. W.; Law, M. Dependence of Carrier Mobility on Nanocrystal Size and Ligand Length in PbSe Nanocrystal Solids. *Nano Lett.* **2010**, *10* (5), 1960−1969.

(21) Kagan, C. R.; Murray, C. B. Charge transport in strongly coupled quantum dot solids. *Nat. Nanotechnol.* **2015**, *10* (12), 1013− 1026.

(22) Ip, A. H.; Thon, S. M.; Hoogland, S.; Voznyy, O.; Zhitomirsky, D.; Debnath, R.; Levina, L.; Rollny, L. R.; Carey, G. H.; Fischer, A.; Kemp, K. W.; Kramer, I. J.; Ning, Z. J.; Labelle, A. J.; Chou, K. W.; Amassian, A.; Sargent, E. H. Hybrid passivated colloidal quantum dot solids. *Nat. Nanotechnol.* **2012**, *7* (9), 577−582.

(23) Choi, J.; Kim, Y.; Jo, J. W.; Kim, J.; Sun, B.; Walters, G.; García de Arquer, F. P.; Quintero-Bermudez, R.; Li, Y. Y.; Tan, C. S.; Quan, L. N.; Kam, A. P. T.; Hoogland, S.; Lu, Z. H.; Voznyy, O.; Sargent, E. H. Chloride Passivation of ZnO Electrodes Improves Charge Extraction in Colloidal Quantum Dot Photovoltaics. *Adv. Mater.* **2017**, *29* (33), 1702350.

(24) Jean, J.; Chang, S.; Brown, P. R.; Cheng, J. J.; Rekemeyer, P. H.; Bawendi, M. G.; Gradecak, S.; Bulovic, V. ZnO Nanowire Arrays for Enhanced Photocurrent in PbS Quantum Dot Solar Cells. *Adv. Mater.* **2013**, *25* (20), 2790−2796.

(25) Azmi, R.; Seo, G.; Ahn, T. K.; Jang, S. Y. High-Efficiency Air- Stable Colloidal Quantum Dot Solar Cells Based on a Potassium- Doped ZnO Electron-Accepting Layer. *ACS Appl. Mater. Interfaces* **2018**, *10* (41), 35244−35249.

(26) Park, H. Y.; Ryu, I.; Kim, J.; Jeong, S.; Yim, S.; Jang, S. Y. PbS Quantum Dot Solar Cells Integrated with Sol-Gel-Derived ZnO as an n-Type Charge-Selective Layer. *J. Phys. Chem. C* **2014**, *118* (31), 17374−17382.

(27) Choi, M. J.; García de Arquer, F. P.; Proppe, A. H.; Seifitokaldani, A.; Choi, J.; Kim, J.; Baek, S. W.; Liu, M. X.; Sun, B.; Biondi, M.; Scheffel, B.; Walters, G.; Nam, D. H.; Jo, J. W.; Ouellette, O.; Voznyy, O.; Hoogland, S.; Kelley, S. O.; Jung, Y. S.; Sargent, E. H. Cascade surface modification of colloidal quantum dot inks enables efficient bulk homojunction photovoltaics. *Nat. Commun.* **2020**, *11* (1), 103.

(28) Mahajan, C.; Sharma, A.; Rath, A. K. Solution-Phase Hybrid Passivation for Efficient Infrared-Band Gap Quantum Dot Solar Cells. *ACS Appl. Mater. Interfaces* **2020**, *12* (44), 49840−49848.

(29) Sukharevska, N.; Bederak, D.; Goossens, V. M.; Momand, J.; Duim, H.; Dirin, D. N.; Kovalenko, M. V.; Kooi, B. J.; Loi, M. A. Scalable PbS Quantum Dot Solar Cell Production by Blade Coating from Stable Inks. *ACS Appl. Mater. Interfaces* **2021**, *13* (4), 5195− 5207.

(30) Biondi, M.; Choi, M. J.; Ouellette, O.; Baek, S. W.; Todorovic, P.; Sun, B.; Lee, S.; Wei, M. Y.; Li, P. C.; Kirmani, A. R.; Sagar, L. K.; Richter, L. J.; Hoogland, S.; Lu, Z. H.; García de Arquer, F. P.; Sargent, E. H. A Chemically Orthogonal Hole Transport Layer for Efficient Colloidal Quantum Dot Solar Cells. *Adv. Mater.* **2020**, *32* (17), 1906199.

(31) Lee, S.; Choi, M. J.; Sharma, G.; Biondi, M.; Chen, B.; Baek, S. W.; Najarian, A. M.; Vafaie, M.; Wicks, J.; Sagar, L. K.; Hoogland, S.; de Arquer, F. P. G.; Voznyy, O.; Sargent, E. H. Orthogonal colloidal quantum dot inks enable efficient multilayer optoelectronic devices. *Nat. Commun.* **2020**, *11* (1), 4814.

(32) Yang, J.; Oh, J. T.; Kim, M.; Song, H.; Boukhvalov, D. W.; Lee, S. H.; Choi, H.; Yi, W. Hybrid Surface Passivation for Retrieving Charge Collection Efficiency of Colloidal Quantum Dot Photovoltaics. *ACS Appl. Mater. Interfaces* **2020**, *12* (39), 43576−43585.

(33) Teh, Z. L.; Hu, L.; Zhang, Z. L.; Gentle, A. R.; Chen, Z. H.; Gao, Y. J.; Yuan, L.; Hu, Y. C.; Wu, T.; Patterson, R. J.; Huang, S. J. Enhanced Power Conversion Efficiency via Hybrid Ligand Exchange Treatment of p-Type PbS Quantum Dots. *ACS Appl. Mater. Interfaces* **2020**, *12* (20), 22751−22759.

(34) Zhang, Y. N.; Kan, Y. Y.; Gao, K.; Gu, M. F.; Shi, Y.; Zhang, X. L.; Xue, Y.; Zhang, X. N.; Liu, Z. K.; Zhang, Y.; Yuan, J. Y.; Ma, W. L.; Jen, A. K. Y. Hybrid Quantum Dot/Organic Heterojunction: A Route to Improve Open-Circuit Voltage in PbS Colloidal Quantum Dot Solar Cells. *ACS Energy Lett.* **2020**, *5* (7), 2335−2342.

(35) Chiu, A.; Rong, E.; Bambini, C.; Lin, Y. D.; Lu, C. C. F.; Thon, S. M. Sulfur-Infused Hole Transport Materials to Overcome Performance-Limiting Transport in Colloidal Quantum Dot Solar Cells. *ACS Energy Lett.* **2020**, *5* (9), 2897−2904.

(36) Kirmani, A. R.; Garcia de Arquer, F. P.; Fan, J. Z.; Khan, J. I.; Walters, G.; Hoogland, S.; Wehbe, N.; Said, M. M.; Barlow, S.; Laquai, F.; Marder, S. R.; Sargent, E. H.; Amassian, A. Molecular Doping of the Hole-Transporting Layer for Efficient, Single-Step-Deposited Colloidal Quantum Dot Photovoltaics. *ACS Energy Lett.* **2017**, *2* (9), 1952−1959.

(37) Zhang, X. L.; Justo, Y.; Maes, J.; Walravens, W.; Zhang, J. D.; Liu, J. H.; Hens, Z.; Johansson, E. M. J. Slow recombination in quantum dot solid solar cell using p-i-n architecture with organic p type hole transport material. *J. Mater. Chem. A* **2015**, *3* (41), 20579−20585.

(38) Tavakoli Dastjerdi, H.; Qi, P. F.; Fan, Z. Y.; Tavakoli, M. M. Cost-Effective and Semi-Transparent PbS Quantum Dot Solar Cells Using Copper Electrodes. *ACS Appl. Mater. Interfaces* **2020**, *12* (1), 818−825.

(39) Wang, R. L.; Wu, X.; Xu, K. M.; Zhou, W. J.; Shang, Y. Q.; Tang, H. Y.; Chen, H.; Ning, Z. J. Highly Efficient Inverted Structural Quantum Dot Solar Cells. *Adv. Mater.* **2018**, *30* (7), 1704882.

(40) Gao, J. B.; Perkins, C. L.; Luther, J. M.; Hanna, M. C.; Chen, H. Y.; Semonin, O. E.; Nozik, A. J.; Ellingson, R. J.; Beard, M. C. n-Type Transition Metal Oxide as a Hole Extraction Layer in PbS Quantum Dot Solar Cells. *Nano Lett.* **2011**, *11* (8), 3263−3266.

(41) Liu, S. Q.; Hu, L.; Huang, S. J.; Zhang, W. Q.; Ma, J. J.; Wang, J. C.; Guan, X. W.; Lin, C. H.; Kim, J. Y.; Wan, T.; Lei, Q.; Chu, D. W.; Wu, T. Enhancing the Efficiency and Stability of PbS Quantum Dot Solar Cells through Engineering an Ultrathin NiO Nanocrystalline Interlayer. *ACS Appl. Mater. Interfaces* **2020**, *12* (41), 46239−46246.

(42) Jin, Z. W.; Yuan, M. J.; Li, H.; Yang, H.; Zhou, Q.; Liu, H. B.; Lan, X. Z.; Liu, M. X.; Wang, J. Z.; Sargent, E. H.; Li, Y. L. Graphdiyne: An Efficient Hole Transporter for Stable High- Performance Colloidal Quantum Dot Solar Cells. *Adv. Funct. Mater.* **2016**, *26* (29), 5284−5289.

(43) Tulsani, S. R.; Rath, A. K.; Late, D. J. 2D-MoS2 nanosheets as effective hole transport materials for colloidal PbS quantum dot solar cells. *Nanoscale Advances 2019*, *1* (4), 1387−1394.

(44) Biondi, M.; Choi, M.-J.; Lee, S.; Bertens, K.; Wei, M.; Kirmani, A. R.; Lee, G.; Kung, H. T.; Richter, L. J.; Hoogland, S.; Lu, Z.-H.; García de Arquer, F. P.; Sargent, E. H. Control Over Ligand Exchange Reactivity in Hole Transport Layer Enables High-Efficiency Colloidal Quantum Dot Solar Cells. *ACS Energy Lett.* **2021**, *6*, 468−476.

(45) Biondi, M.; Choi, M.-J.; Lee, S.; Bertens, K.; Wei, M.; Kirmani, A. R.; Lee, G.; Kung, H. T.; Richter, L. J.; Hoogland, S.; Lu, Z.-H.; García de Arquer, F. P.; Sargent, E. H. Control Over Ligand Exchange Reactivity in Hole Transport Layer Enables High-Efficiency Colloidal Quantum Dot Solar Cells. *ACS Energy Lett.* **2021**, *6* (2), 468−476.

(46) Luther, J. M.; Law, M.; Song, Q.; Perkins, C. L.; Beard, M. C.; Nozik, A. J. Structural, optical and electrical properties of selfassembled films of PbSe nanocrystals treated with 1,2-ethanedithiol. *ACS Nano* **2008**, *2* (2), 271−280.

(47) Fan, J. Z.; La Croix, A. D.; Yang, Z.; Howard, E.; Quintero- Bermudez, R.; Levina, L.; Jenkinson, N. M.; Spear, N. J.; Li, Y. Y.; Ouellette, O.; Lu, Z. H.; Sargent, E. H.; Macdonald, J. E. Ligand cleavage enables formation of 1,2-ethanedithiol capped colloidal quantum dot solids. *Nanoscale* **2019**, *11* (22), 10774−10781.

(48) Tavakoli Dastjerdi, H.; Tavakoli, R.; Yadav, P.; Prochowicz, D.; Saliba, M.; Tavakoli, M. M. Oxygen Plasma-Induced p-Type Doping Improves Performance and Stability of PbS Quantum Dot Solar Cells. *ACS Appl. Mater. Interfaces* **2019**, *11* (29), 26047−26052.

(49) Tulsani, S. R.; Rath, A. K. Photo-induced surface modification to improve the performance of lead sulfide quantum dot solar cell. *J. Colloid Interface Sci.* **2018**, *522*, 120−125.

(50) Tang, J. A.; Sargent, E. H. Infrared Colloidal Quantum Dots for Photovoltaics: Fundamentals and Recent Progress. *Adv. Mater.* **2011**, *23* (1), 12−29.

(51) Hassinen, A.; Moreels, I.; De Nolf, K.; Smet, P. F.; Martins, J. C.; Hens, Z. Short-Chain Alcohols Strip X-Type Ligands and Quench the Luminescence of PbSe and CdSe Quantum Dots, Acetonitrile Does Not. *J. Am. Chem. Soc.* **2012**, *134* (51), 20705−20712.

(52) Kirmani, A. R.; Carey, G. H.; Abdelsamie, M.; Yan, B. Y.; Cha, D.; Rollny, L. R.; Cui, X. Y.; Sargent, E. H.; Amassian, A. Effect of Solvent Environment on Colloidal-Quantum-Dot Solar-Cell Manufacturability and Performance. *Adv. Mater.* **2014**, *26* (27), 4717− 4723.

(53) Jung, J.; Chang, M.; Yoon, H. Interface Engineering Strategies for Fabricating Nanocrystal-Based Organic-Inorganic Nanocomposites. *Appl. Sci.* **2018**, *8* (8), 1376.

(54) Song, J. H.; Choi, H.; Kim, Y. H.; Jeong, S. High Performance Colloidal Quantum Dot Photovoltaics by Controlling Protic Solvents in Ligand Exchange. *Adv. Energy Mater.* **2017**, *7* (15), 1700301.

(55) Jean, J.; Mahony, T. S.; Bozyigit, D.; Sponseller, M.; Holovsky, J.; Bawendi, M. G.; Bulovic, V. Radiative Efficiency Limit with Band Tailing Exceeds 30% for Quantum Dot Solar Cells. *ACS Energy Lett.* **2017**, *2* (11), 2616−2624.

(56) Zherebetskyy, D.; Scheele, M.; Zhang, Y. J.; Bronstein, N.; Thompson, C.; Britt, D.; Salmeron, M.; Alivisatos, P.; Wang, L. W. Hydroxylation of the surface of PbS nanocrystals passivated with oleic acid. *Science* **2014**, *344* (6190), 1380−1384.

(57) Brown, P. R.; Kim, D.; Lunt, R. R.; Zhao, N.; Bawendi, M. G.; Grossman, J. C.; Bulovic, V. Energy Level Modification in Lead Sulfide Quantum Dot Thin Films through Ligand Exchange. *ACS Nano* **2014**, *8* (6), 5863−5872.

(58) Fabregat-Santiago, F.; Garcia-Belmonte, G.; Mora-Sero, I.; Bisquert, J. Characterization of nanostructured hybrid and organic solar cells by impedance spectroscopy. *Phys. Chem. Chem. Phys.* **2011**, *13* (20), 9083−9118.

(59) Luther, J. M.; Law, M.; Beard, M. C.; Song, Q.; Reese, M. O.; Ellingson, R. J.; Nozik, A. J. Schottky Solar Cells Based on Colloidal Nanocrystal Films. *Nano Lett.* **2008**, *8* (10), 3488−3492.

(60) Pattantyus-Abraham, A. G.; Kramer, I. J.; Barkhouse, A. R.; Wang, X. H.; Konstantatos, G.; Debnath, R.; Levina, L.; Raabe, I.; Nazeeruddin, M. K.; Gratzel, M.; Sargent, E. H. Depleted- Heterojunction Colloidal Quantum Dot Solar Cells. *ACS Nano* **2010**, *4* (6), 3374−3380.

(61) Liu, M. X.; de Arquer, F. P. G.; Li, Y. Y.; Lan, X. Z.; Kim, G. H.; Voznyy, O.; Jagadamma, L. K.; Abbas, A. S.; Hoogland, S.; Lu, Z. H.; Kim, J. Y.; Amassian, A.; Sargent, E. H. Double-Sided Junctions Enable High-Performance Colloidal-Quantum-Dot Photovoltaics. *Adv. Mater.* **2016**, *28* (21), 4142−4148.

Chapter-5

Summary and Future Outlook

In the past two decades, PbS Quantum dot (QDs) and Perovskite solar cells have been the forerunner for the next-gen commercialization to move away from the costly Silicon solar cells. The highest efficiencies for these c-Si modules are 16-20% and not much room for improvement as the values ever come close to the theoretical limit. Additionally, these technologies, namely lead sulfide QDs and $CH_3NH_3PbI_3$ perovskites can be used to construct tandem solar cells to overcome the Shockley Quessier limit involving only a single p-n junction diode. Though both materials show interesting properties such as high photostability and high molar extinction coefficients for PbS QDs and high carrier mobility and ambipolar transport for $CH_3NH_3PbI_3$, the performance is limited by the top p-type hole transport layer (HTL) which can act as a deterrent for realizing the full potential of the solar cells. In 3D $CH_3NH_3PbI_3$ perovskites, the material tends to grow inhomogeneously while being spin coated and thus can lead to low short circuit current and decreased reproducibility. Subsequently, moisture ingress and air oxidation are two factors that perovskites are highly sensitive to and can damage the perovskite structure leading to precursor (PbI_2 and MAI) formation. Thus, we need a capping layer which not only helps in improving the charge transport for the holes but also prevents moisture or even electrode penetration. In PbS QD we have two facets, the (111) polar facet comprising of only lead atoms and charge-neutral (200) facet with alternating Pb and S atoms. The alternate vacant Pb atoms in (111) surface lead to Pb-OH formation which acts as the trap states and reduces efficiency. The conventional ligand exchange with halometallate (PbI_3^-) also leads to a rise in polydispersity which can again affect performance as differential bandgaps can act as mid gap states for nearby QDs. Thus, passivating these states is important to overcome these difficulties. Generally, iodide passivation leads to an n-type PbS, and thiol passivation leads to p-type PbS. Another major issue for the PbS QDs is the time and chemicals consumed in the removal of oleic acid from the as-synthesized PbS by commonly followed sequential cleaning (6-8 times) from methanol for the p-type layer coating (EDT exchanged). The resulting PbS QDs though devoid of excess oleic acid ligands, also lose much of their photophysical properties leading to a net reduction in open-circuit voltage and fill factor in solar cells. QDs need to be thoroughly passivated in a single step to protect the QDs from overexposure to uncontrolled chemical reactions. The electronic properties of the QD solar cells stem directly from their surface properties and as the bandgap is indirectly proportional to the size of the QDs, polydispersity plays a role too.

In this thesis, we discuss various strategies to combat the shortcomings listed above to achieve high-efficiency solar cells for both perovskite and PbS QDs. In Chapter 1, we looked at the genesis of photovoltaics and development through different generations of solar cells as well as the properties and improvements in perovskites and PbS QDs were discussed in detail.

In Chapter 2, to combat small crystallite sizes and cracks in the film (as seen from SEM) with $PbAc_2$ as a precursor of perovskite, antisolvent treatment was introduced using chlorobenzene on top of the spinning film which increases grain size and nullifies cracks on perovskite films. A homogeneous growth along the (110) plane is seen which bodes well for the charge transport. Additionally, as seen using hole transport layer, Spiro-OMeTAD leads to the film having pinholes and cracks which could lead to either moisture or gold electrode seeping and decrease performance. To this end, this organic molecule is combined with the polymer P3HT which also acts as HTL but lacks charge transport properties of the former. The HTL formed by P3HT is thick and thus having a blend of P3HT: Spiro-OMeTAD in 1:3 ratio grants us a robust HTL which boosts performance and shows less hysteresis when compared to only spiro-OMeTAD film. There being a concern of low hole mobility due to the organic molecules embedded into the polymer matrix, SCLC calculation proved it to be on par with the Spiro-OMeTAD. A high recombination lifetime for the blend is obtained when compared to both the constituents separately. The increase is observed for all three photovoltaic parameters and statistical distribution showed high fidelity in PCE and fill factor with 14.9% and 0.70 being the highest, respectively. This is a marked increase when compared to Spiro-OMeTAD (PCE = 11.2%, FF = 0.50) and P3HT (PCE = 8.85%, FF = 0.49) only cells. This study shows the importance of morphology of both the active layer and the HTL for the reproducible films with good junctions leading to high fill factor and efficiency for solar PSCs.

The polar (111) plane in the PbS QDs terminated by Pb atoms is prone to oxidation due to the alternate vacant atoms after exchange with PbI_3^- ligands. In Chapter 3, we sought to passivate the QDs with small thiol ligand in conjunction with PbI_3^- and fill up those vacant sites. The best contender for the said thiol would have been 3-mercapto propionic acid, a thiol known for its high performance in solid-state ligand exchange but due to its agglomeration and subsequent precipitation, we utilized its ester form 3-mercapto propionate (MPE). The SH binding site of the ligand can interact with the Pb at the (111) plane squeezing in between the halometallate ligands. The MPE addition leads to reduced polydispersity as evidenced from the excitonic peak in the absorbance with a higher redshift. From the Photoluminescence (PL) of films, we see emergence and strengthening of band-edge PL emission peak around 1100 nm upon increasing the amount of MPE in the halometallate solution while the other peak at 1500 nm reduces proportionately. This peak could be the result of either low energy state formation (Pb-OH) or QD fusing both of which are negated by thiol passivation. This leads to a reduced stokes shift and low Urbach energy indicating homogeneous growth for MPE passivated films. This monodispersity and near-unity retention of band-edge PL leads to a 33% increase in average PCE highest being 9.6% with a reduction in density of the intermediate trap states, an increase in mobility, and an increase in depletion width. The findings of this study emphasize the benefits of the mutual passivation strategy for reducing trap states and provide solar cells with better optoelectronic properties.

Continuing from the studies of the previous chapter, it was noticed that the conventional method of sequentially cleaning the oleic acid (OA) capped PbS QDs to partially remove oleic acid using methanol washing to facilitate solid-state ligand exchange with 1,2-ethandithiol for the top hole transport layer later on, though leading to a crack-free film, is detrimental to the electronic and optical properties of the PbS QDs. For this, in Chapter 4, a one-step-solution-phase short ligand, NH_4SCN, to partially replace the surface-bound oleic acid ligand while retaining the optoelectronic properties is introduced. Ammonium salts are the chosen candidates with NH_4Cl, NH_4Br, and NH_4SCN able to redisperse in octane after the partial removal of OA while NH_4I interaction led to PbS QDs turning n-type and hence insoluble in non-polar solvents. AFM and SEM show that the surface roughness is high and cracks are present in large quantities for 2W-MeOH (nW-MeOH, where n indicates the number of washings) which simmer down to a large extent for 8W-MeOH (3.72 nm rms roughness to 0.89 nm) but the films obtained from NH_4SCN and NH_4Cl treated PbS QDs are almost crack-free and have less surface roughness (NH_4SCN = 0.72 nm). The PbS QDs obtained after the ammonium salt interaction show retention in excitonic and PL peak whereas multiple washing leads to a linear increase in polydispersity (peak broadening) and a similar decrease in band edge PL intensity. The PL intensity of ammonium salts is 2 times that of 8W-MeOH. NH_4SCN treated HTL outperforms in solar cells due to the increase in all the photovoltaic parameters, and the increase in PCE is to the tune of 11% over 8W-MeOH. In the case of NH_4Cl and NH_4Br treated HTLs, V_{OC} remained unchanged, J_{SC} increases but FF decreases to yield comparable PCE with 8W-MeOH HTL. An increase in depletion width and recombination resistance supports the increase in J_{SC} and FF, and higher built-in voltage backs the increment in V_{OC} in NH_4SCN HTL solar cells. The majority carrier density and the hole mobility for NH_4SCN HTL were obtained to be 1.5 times higher than 8W-MeOH which is also predicted by 1D SCAPS simulation software. The highest obtained efficiency by jointly tuned p-type CPT-PbS and p^+ NH_4SCN HTL was 10.5%. This approach for HTL preparation shown in this study could replace the conventional HTL preparation for PbS QDs saving time and chemicals.

The best overall efficiency for PSCs and PbS QDSCs stands at 24.3% and 13.8% respectively. The third generation of solar cells focuses on developing strategies to overcome the limitations of single p-n junctions and thus have higher efficiency output at a smaller cost value. A tandem solar cell employing $CH_3NH_3PbI_3$ and PbS QDs as the absorbing layers could be developed to compete with existing Silicon solar cells. As the $CH_3NH_3PbI_3$ perovskite has a bandgap around 1.54 eV, the bandgap of PbS QDs has to be around 1 eV for efficient NIR photon harvesting. The HTLs developed in these studies, i.e. P3HT blended Spiro-OMeTAD for perovskite and NH_4SCN cleaned PbS QDs could be utilized for enhanced morphology. This technique can take advantage of enhanced V_{OC} ($V_{PbS} + V_{perov}$) for ultimately achieving higher PCE.

ABSTRACT

Name of the Student: Ashish Sharma **Registration No.: 10CC15A26017**

Faculty of Study: Chemical Science **Year of Submission: 2021**

CSIR Lab: NCL, Pune **Name of the Supervisor: Dr Arup Rath**

Title of the thesis: Designing the Hole Transport Layer for the Development of Perovskite and Quantum Dot Solar Cells

----

This thesis explores the various hole transport layer (HTL) preparation strategies for the perovskite ($CH_3NH_3PbI_3$) and lead sulfide quantum dot (PbS QD) solar cells. In this thesis, the improvement has been looked at from a morphological standpoint while simultaneously improving the photophysical and electronic properties of the HTL. Chapter 1 of the thesis introduces the need for photovoltaic technology, its progress over the ages, and the current technologies perovskite and PbS QDs. Background information and current research in these technologies are also discussed. Chapter 2 works towards the two-fold improvement in the $CH_3NH_3PbI_3$ solar cells where the morphological defects arising from the lead acetate based active layer and spiro-OMeTAD HTL are remedied using antisolvent treatment by chlorobenzene and 1:3 P3HT:spiro-OMeTAD HTL, respectively. The junction properties and HTL mobility were analyzed to be in line with the efficiency improvement. Chapter 3 moves towards more stable PbS QDs where the trap states formed at the PbS (111) facet while using the conventional PbI_3^-, were reduced by mutual passivation of PbI_3^- + 3-Methyl mercaptopropionate (MPE) during the ligand exchange process. Optoelectronic studies were conducted with the new passivation strategy showing lower polydispersity and lesser density of trap states with higher lifetime. Chapter 4 looks towards solving the age-old issues involved with sequential cleaning for partial removal of oleic acid ligands from the PbS QDs for HTL treatment, by introducing a single step cleaning utilizing ammonium salts. Ammonium thiocyanate (NH_4SCN) managed to give the best performance. AFM and SEM were used to study morphology and other electronic studies helped analyze the NH_4SCN treated PbS QDs for their hole mobility and doping density. Chapter 5 summarizes the work done in this thesis and recommends future directions for this research for their further use in photovoltaic applications.

List of Publication(s) in SCI Journal(s) Emanating from the Thesis Work

(1) **Sharma, A.**; Rath, A. K. Improved Performance and Reproducibility of Perovskite Solar Cells by Jointly Tuning the Hole Transport Layer and the Perovskite Layer Deposition. *J. Mater. Sci. Mater. Electron.* **2018**, *29* (15), 12652–12661. https://doi.org/10.1007/s10854-018-9382-8.

(2) **Sharma, A.**; Mahajan, C.; Rath, A. K. Reduction of Trap and Polydispersity in Mutually Passivated Quantum Dot Solar Cells. *ACS Appl. Energy Mater.* **2020**, *3* (9), 8903–8911. https://doi.org/10.1021/acsaem.0c01378.

(3) **Sharma, A.**; Dambhare, N. V; Bera, J.; Sahu, S.; Rath, A. K. Crack-Free Conjugated PbS Quantum Dot–Hole Transport Layers for Solar Cells. *ACS Appl. Nano Mater.* **2021**, *4* (4), 4016–4025. https://doi.org/10.1021/acsanm.1c00373.

List of papers with abstract presented (oral or poster) at national or international conferences /seminars

(1) **“Science Day Celebration 2020”** held at CSIR National Chemical Laboratory Pune. (Presented poster)

(2) “**Mumbai Pune Semiconductor Conference 2019**” held at Indian Institute of Technology, Mumbai (IIT Bombay). (Presented Poster)

(3) **“Science Day Celebration 2019”** held at CSIR National Chemical Laboratory Pune. (Presented poster)